Nanoscale structural/chemical characterization of manganese oxide surface layers and nanoparticles, and the associated implications for drinking water

Michel Eduardo Vargas Vallejo

Dissertation submitted to the faculty of the
Virginia Polytechnic Institute and State University
in partial fulfillment of the requirements for the degree of

Doctor of Philosophy
In
Materials Science and Engineering

Mitsuhiro Murayama
William R. Knocke
William T. Reynolds Jr.
Sean G. Corcoran
Frederick M. Michel

September 10th, 2015
Blacksburg, VA

Keywords: Water Filtration, $MnO_{x(s)}$ Coating, Nanomaterial, Characterization

Nanoscale structural/chemical characterization of manganese oxide surface layers and nanoparticles, and the associated implications for drinking water

Michel Eduardo Vargas Vallejo

Abstract

Water treatment facilities commonly reduce soluble contaminants, such as soluble manganese (Mn^{2+}), in water by oxidation and subsequent filtration. Previous studies have shown that conventional porous filter system removes Mn^{2+} from drinking water by developing Mn-oxides ($MnO_x(s)$) bearing coating layers on the surface of filter media. Multiple models have been developed to explain this Mn^{2+} removal process and the formation mechanism of $MnO_x(s)$ coatings. Both, experimental and theoretical studies to date have been largely focused on the micrometer to millimeter scale range; whereas, coating layers are composed of nanoscale particles and films. Hence, understanding the nanoscale particle and film formation mechanisms is essential to comprehend the complexity of soluble contaminant removal processes. The primary objective of this study was to understand the initial $MnO_x(s)$ coating formation mechanisms and evaluate the influence of filter media characteristics on these processes. We pursued this objective by characterizing at the micro and nanoscale $MnO_x(s)$ coatings developed on different filter media by bench-scale column tests with simulating inorganic aqueous chemistry of a typical coagulation fresh water treatment plant, where free chlorine is present across filter bed. Analytical SEM and TEM, powder and synchrotron-based XRD, XPS, and ICPMS were used for characterization of coatings, filter media and water solution elemental chemistry. A secondary objective was to model how surface coating formation occurred and its correlation with experimentally observed physical characteristics. This modeling exercise indicates that surface roughness and morphology of filtering media are the major contributing factors in surface coating

formation process. Contrary to previous models that assumed a uniform distribution and growth of surface coating, the experimental results showed that greater amounts of coating were developed in rougher areas. At the very early stage of coating formation, unevenly distributed thin films and/or particle aggregates were observed, which provided active sites for further surface coating growth. The predominant $MnO_x(s)$ phase in the surface coatings was identified to be poorly crystalline birnessite having scavenging activity by intercalation and/or sorption. This would explain the enhancement of efficiency in removing soluble manganese and other contaminants during water filtration. Moreover, the increased Mn^{2+} removal effect of having aluminum (Al) in pre-treated water is explained. These results indicate that the surface roughness and morphology need to be incorporated into particle capture models to more precisely describe the soluble manganese removal process.

Acknowledgements

First and foremost, I would like to thank God for all the blessings received, especially for my family and for allowing me to follow this path. Second, I would like to extend a special thanks to my primary faculty advisor Dr. Mitsuhiro Murayama for his leadership and guidance throughout these years. I would specifically like to thank Dr. William R. Knocke, Dr. Michael F. Hochella, Jr., Dr. William T. Reynolds, Dr. Sean G. Corcoran, and Dr. Frederick M. Michel for their insights and their expenditure of time helping me to improve my work and my skills. Additionally, I would like to recognize Mr. Gary Hinds for his assistance in performing the column test experiments for obtaining the media samples analyzed in this research project and for obtaining the ICP-MS measurements. For the financial support, I also want to thank the International Fulbright Science and Technology program and the Institute for Critical Technology and Applied Science –ICTAS- at VT. I am also grateful to all my colleagues and coworkers for all of their contributions to this project.

I want to express my love and gratitude to my wife –Vanessa- for her constant support, patience, and unconditional love. She has been instrumental in helping me to simultaneously raise a family and pursue my doctoral studies. Without her, I would not have been able to accomplish so much. She is the one, my only one. I also want to thank my daughters Isabella and Daniela for being the inspiration that keeps me going. Finally, I would like to thank my parents –Guido and Lorgia- who have always stood by me, giving me their unconditional support, encouragement, infinite love and strength to pursue my goals.

Table of Contents

List of Figures

List of Tables

Glossary

E

Effluent: any outflowing water solution that exits the filter after interacting with the filter bed.

G

Granule morphology of filter media: the typical shape of a small particle of any material used as a collector in a filter.

I

Influent: any water solution that flows into the filter and start to interact with the filter bed.

P

Poorly crystallized: any solid substance that has a low or poor degree of structural order that do not produce sharp and narrow peaks in a diffraction experiment with X-rays.

S

Soluble species: any chemical substance that is present in water as an elementary unit and forms a solution.

CHAPTER 1. Introduction

1.1. Background

1.1.1 Solution chemistry of fresh water filtration process and manganese oxides coating formation

Fresh water filtration processes worldwide aim to provide safe drinking water. These processes have a dramatic impact on reducing waterborne diseases and thus represent a key factor in human health protection. Removal of soluble manganese (Mn^{2+}) is an important goal of the drinking water treatment processes and is originally aimed to solve aesthetic problems, which arise when this contaminant enters the distribution system with concentrations above the US EPA secondary maximum contaminant level (SMCL) guideline of 0.05 mg/L [1, 2]. However, even with lower Mn^{2+} concentrations (0.02 mg/L), some customers complain about brownish/blackish water, changes in taste and odor, and staining of laundry and fixtures. [1, 3, 4]. Recently, emerging health concerns that are potentially associated with the soluble manganese in drinking water have been addressed. Exposure to high concentrations of manganese over the course of years could trigger a wide range of negative health effects. Increasing evidence [5] suggests that high level of manganese in drinking water may have adverse neurological impacts on children. Furthermore, Sain (2013) also refers the possible health risk of high manganese exposure by inhalation of aerosols originating from showers and portable home humidifiers.

Commonly, water treatment providers reduce the soluble manganese concentration by oxidation and subsequent filtration. An extensive body of literature show that the mixed porous filters in water facilities remove this soluble contaminant at circumneutral pH by precipitating manganese oxides ($MnO_x(s)$) on the surface of the filter media in the presence of an oxidant. [6-10]. On the other hand, elevated soluble manganese levels are found in the filtered water with the absence of an oxidant [9], demonstrating a dramatic reduction in the removal efficiency.

Multiple models have been drawn to explain the removal mechanisms of soluble Mn by MnO_x(s)-precoated media [6, 10-12] by now. These models were developed based upon one of the following hypotheses regarding the Mn oxidation process:

1) Homogeneous distribution of active sites for sorption and surface catalyzed oxidation over the entire media surface [13, 14]; and,
2) Localized or inhomogeneous distribution of active sites for oxidation and precipitation on the media surface [11, 15, 16].

With regards to the first case, models were developed based on mass transfer and sorption processes, including macroscopic solution rate constants data, surface diffusion and superficial manganese oxidation by surface coating. A simplified general equation for this reaction, following Merkle et al. (1997), can be written as:

$$Mn^{2+} + Active\ Site + OCl^- \Leftrightarrow MnO_{x(s)} + Active\ Site + Cl^- \quad (1),$$

where the active site has not been detailed characterized by researchers due to technical challenges related to available techniques, insufficient information about the structure of sorption sites and oxidation products.

With regards to the second case, traditional colloid filtration theory (CFT) models were mainly used. Amirtharajah (1988) summarizes these theoretical and conceptual models [17]. These models commonly use the classical electrical double-layer theory, which provides inexact predictions for filtration under unfavorable conditions of surface charge interaction (due to homogeneous surface potential assumptions) between spherical colloid particles and flat smooth surfaces of filter media. [18-20].

It should be noted that none of above-mentioned models focus on the initial formation of MnO_x(s) coatings; i.e., the oxidation of soluble manganese on the bare media surface in water filtration systems or what has been called the “natural greensand effect (NGE)” [7]. Several authors [8, 13-15,

[21-24] have pursued studies towards explaining this initial MnO_x(s) coating formation; however, there is still no consensus on the formation mechanisms. Two models are mainly considered for explaining this process.

The first model proposed by Davies and Morgan (1989) (ligand model, hereafter) includes the oxidation of soluble manganese on the specific active sites of a bare media surface. Their model assumes the process starts with adsorption of Mn^{2+} on reactive sites that are monodentate and bidentate complexes. They suggest that bidentate complexes are the reactive species in this process [13]. Then, the adsorbed Mn^{2+} is complexed to molecular oxygen by transferring an electron from Mn to O_2, forming a Mn^{3+} superoxide complex. Finally, precipitation occurs at catalytic surface sites. A newly formed MnO_x(s) solid catalyzes further this process due to its greater activity, and the precipitate continues to grow at the absorption sites. Considerations of homogeneous distribution of active sites on media surface are taken into account while computing this model with solution rate constants data.

The second model developed by Junta-Rosso et al. (1997) (geometric model) assumes that Mn^{2+} heterogeneous oxidation is taking place in geometric favorable sites on specific locations of the substrate (media) surface and MnO_x(s) precipitation occurs without any sorption process that leads to a monolayer formation, in contrast to the work from Davies and Morgan (1989) [13]. Precipitation occurs near steps and along irregular fractured edges, and only a small fraction of sites promotes the initial Mn^{2+} sorption-oxidation process. According to precipitate morphology, the interface of precipitate/ substrate surface/ solution is much more reactive than other sites.

When comparing these models, the similarities remain in that either one can fit well solution rate constants data used as the macroscopic information for studying these heterogeneous reactions. Since the application of both models relies on the identification of the specific location of the first formed MnO_x(s), the authors of these studies strongly recommend to

pursue microscopic analysis prior to modeling in order to evaluate which model is applicable to a specific situation[15]. They also stress the importance of improving kinetic models by addition of microscopic observations of the substrate and precipitate.

In recent years, improved colloidal interactions models have emerged as a result of taking into account physical and chemical surface heterogeneity of particles and filter media, emulating closely real systems [20, 25, 26]. In these models, a modified Derjaguin-Landau-Verwey-Overbeek (DLVO) theory was used. The DLVO theory combines the effects of van der Waals attraction and the double layer energy in an expression that estimate the interaction behavior between colloidal particles. Now, it has been modified to describe interactions between spherical particles and rough surfaces by including protrusions (asperities) and/or depressions on the surfaces. Figure 1.1 graphically shows this interaction energy with respect to separation distance between a spherical colloid particle and a smooth collector (filter media) surface. Here, the double layer energy is originated in the interaction of two charged objects across liquids. It can be attractive or repulsive in nature depending on the surface charge density of the objects. The charged surface is considered the first layer and the second layer is the one containing neutralizing charge (diffuse layer).[27]

When a particle and media surfaces have like charges, which leads to an unfavorable interaction, the interaction energy curve (labeled “Like-charged surface” in figure 1.1) has two energy minima: an infinitely deep attractive well (primary minimum) within a few nm separation distance, and a shallow attractive well (secondary minimum) at relatively large separation distances -typically larger than 5nm- after the maximum energy barrier. When both surfaces has opposite charges, which leads to a favorable interaction, only a primary minimum exists (curve labeled “Oppositely-charged surfaces” in figure 1.1). Short-range repulsion effects (like hydration and steric repulsion -spatial shielding-) reduce the depth of primary minimum to a finite value.

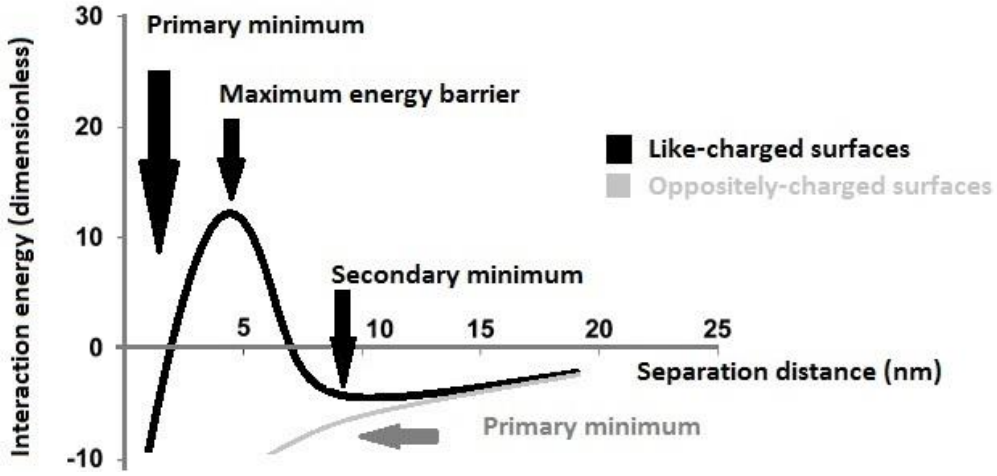

Figure 1.1. Schematic of typical shape of interaction energy curves versus separation distance between colloid particle and filter media surfaces after (Bradford & Torkzaban, 2013).

One of the improved colloidal interaction models proposed by Shen et al. (2012) (rough surface model) consider spherical particles interacting with a plate-type media surface with hemispherical protrusions (asperities) on top of the flat surface for simulating roughness. Irreversible attachments in the primary minima take place at a higher total concentration of ions in solution, ionic strength (IS). The particle attachment and detachment processes are explained in terms of changes in the maximum energy barrier due to variations in IS. A particle attaching on top of protrusions is favored at a higher IS, but reduction in IS allows the particle to detach. The secondary minimum depth increases in concave regions, such as areas aside or between protrusions, due to sidewall interactions, which promotes the particle attachment. Furthermore, actual hydrodynamic forces on particles at the secondary minima are reduced and the particles are somewhat shielded from the hydrodynamic shear force. Bradford and Torkzaban (2013) conclude that the physical heterogeneity has a greater impact on the interaction energy properties compared to chemical heterogeneity [26].

1.1.2 Structure and chemistry of manganese oxide coating on filter media surface

The above overviewed theories indicate that a systematic microscopic observation is essential to understand and properly model the initial MnO_x(s) coating formation mechanisms. Several authors have explained the Mn removal mechanism by MnO_x(s) coatings in filter media by combining information of macroscopic solution chemistry typically obtained by inductively coupled plasma mass spectrometry (ICPMS) and atomic absorption spectroscopy (AAS) with microscopic and spectroscopic evaluations at larger scales. For example, the phase identification of MnO_x(s) coatings by powder X-ray Diffraction with the aid of Energy Dispersive Spectroscopy (EDS) identification of primary constituents by Merkle et al. (1996)[28] shows that the coatings consist of multiple phases of poorly crystalline MnO_x(s) and Mn oxyhydroxides. Definitive structure determination by XRD was not possible due to several factors, limiting the amount of information obtained. Spectra from samples showed particularly broad peaks yielding extremely poor peak resolution. This condition was caused by the lower crystallinity or the small particle size of phases observed. In addition, these broad peaks also obscured the identification of other possible peaks due to peak convolution and overlapping, as well as reduced the signal to noise ratio of the spectra (estimated to be below 2 in many cases) making it impossible to reliably distinguish peaks from background noise. Moreover, missing and shifted peaks also neglected definitive phase identification. This condition could arise from the chemical nonstoichiometry of possible phases (due to the presence of vacancies and substitutional atoms distorting their structure). Qualitative identification of phases was mainly performed by using data with improved peak resolution from powder XRD experiments by (Birkner and Navrotsky, 2012, Bricker, O., 1965)[29, 30] and synchrotron-based XRD (Zhu et al., 2012)[31]. The samples used for obtaining these improved data were independently and carefully synthesized in controlled conditions and sometimes subjected to an aging process for increasing crystallinity, showing sharper peaks in the spectrum. Consequently, chemical constituents were also controlled and monitored, being able to specify

their stoichiometry without the interference of having other phases present. Thermogravimetric analysis was also used for monitoring water content. Moreover, synchrotron-based XRD allowed for improved peak resolution due to the smaller wavelength of the radiation (one order of magnitude) used for the analysis compared to regular powder-based XRD. This feature permitted to correctly distinguish between two adjacent peaks, overcoming overlapping and convolution issues.

Oxidation state information associated with the reactions taking place during soluble manganese uptake and oxidation process was assessed by wet chemistry methods. Okazaki et al. (1997)[32] and Gabelich et al. (2006)[1] used the leucoberbelin blue method for identifying the presence of oxidized soluble Mn ($^{3+}$ and above) in water. This colorimetric essay is based on monitoring the blue color produced when leucoberbelin blue is oxidized by manganese of oxidation states of 3+ and higher. Nevertheless, this method does not distinguish between the different Mn in higher oxidation states. Okazaki et al. (1997)[32] evaluated the soluble Mn (Mn^{2+}) oxidizing activity of the bacteria Pseudomonas Fluorescens GB-1 under different conditions by monitoring the amount of oxidized Mn species present in water. Gabelich et al. (2006)[1] studied the manganese leaching/desorption from filter media of a working coagulation plant when free chlorine was suppressed from feed water and across-filter bed during the filtration step. They monitored and distinguished between the released amounts of oxidized Mn from soluble Mn in water leaving the filter media. Morgan and Stumm (1965)[33], Brewer and Spencer (1971)[34], and Veeramani et al.(2013)[35] used the modified formaldoxime spectrophotometric method for evaluating the amount of Mn^{2+} in solution. This colorimetric assay is based on the oxidation of Mn^{2+} by formaldoxime, yielding an orange-red color in alkaline solution. This method determines the quantity of Mn^{2+} in solution down to a 0.01 ppm limit. Morgan and Stumm (1965)[33] applied this method in investigating the kinetics of the reaction between soluble Mn and dissolved oxygen in various aqueous solutions. Brewer and Spencer (1971)[34] successfully used and modified the

method for analyzing precisely the dissolved manganese (Mn^{2+}) content of the anoxic waters of the Black Sea, overcoming the fact that dissolved oxygen must be present for the color to develop. Veeramani et al.(2013)[35] monitored the remaining amount of Mn^{2+} in solution while synthesizing Mn_3O_4 nanowires at room temperature using iron oxide nanoparticles as a catalyst, manganese chloride, water, PIPES buffer, and atmospheric oxygen as oxidizer. Other methods were reviewed by Morgan and Stumm (1965)[33], which involved the determination of either Mn^{2+} or Mn in higher oxidation states in natural and treated waters by using sensitive oxidation-reduction reagents. These results showed limited accuracy and sensitivity, since Mn-ions can form complexes unfavorable or kinetically slow for oxidation, and samples might contain compounds that rapidly reduced the oxidized reagents. Therefore, X-ray Photoemission Spectroscopy technique was used compensatively for evaluating the Mn oxidation states at the surface of coatings on filter media (Merkle et al, 1996, Han et al., 2006, Cerrato et al., 2011)[28, 36, 37] utilizing previously developed concepts by (Murray et al., 1985, Junta and Hochella, 1994, Nesbitt and Banerjee, 1998) [23, 38, 39]. Merkle et al. (1996)[28] evaluated the Mn oxidation states at the surface of coatings on anthracite and sand filter media from different full-scale water treatment plants using the Mn3s peaks. Han et al. (2006)[36] studied the metal adsorption sites of copper (II) and lead (II) on the surface of manganese oxide coated sand by identifying Mn oxidation states in the surface of coatings using the Mn2p peaks. Cerrato et al. (2011)[37] investigated the soluble Mn removal by manganese oxide coated media by monitoring the Mn oxidation states in the surface of coatings utilizing the Mn3p peaks. Murray et al. (1985)[23] analyzed the Mn oxidation states of initial solid phase products formed during oxidation of soluble Mn by CO_2 free air using the Mn3s peaks. Junta and Hochella (1994)[38] monitored the Mn oxidation states of the heterogeneous oxidation products of soluble Mn by air at hematite, goethite, and albite surfaces using the Mn3s peaks. Nesbitt and Banerjee (1998)[39] evaluated the use of Mn2p peaks for identifying Mn oxidations states present in different Mn oxides and oxyhydroxides. Results indicate that manganese in the surface coatings has a mixture of Mn^{2+}, Mn^{3+}, and Mn^{4+} oxidation states.

In order to improve the understanding of the chemical content of coatings and provide physical observations of the morphology, location and size of coating particles, Electron Probe Micro-Analysis (EPMA) was also employed (Merkle et al., 1996, Sahabi et al., 2009)[28, 40]. Merkle et al. (1996)[28] performed transect analysis of elemental content of Mn, Al, and Fe from cross-section of coatings on anthracite and sand filter media from different full-scale water treatment plants by EPMA. Sahabi et al. (2009)[40] investigated the morphological and chemical characteristics of coatings on anthracite filter media of a biological water treatment plant using EPMA in combination with wavelength dispersive spectroscopy WDS. Simultaneously, scanning electron microscopy with energy dispersive X-ray spectroscopy (SEM/EDS) was used to explain the coating morphology, obtain quantitative distribution of Mn content on coatings, and evaluate their connection to surface characteristics (Hu et al.,2004, Junta and Hochella, 1994, Sahabi et al., 2009, Merkle et al., 1996, O'Reilly and Hochella, 2003, Han et al., 2006, Kim and Jung, 2008, Tobiason et al., 2008)[9, 28, 36, 38, 40-43]. Hu et al. (2004)[41] evaluated the characteristics of manganese oxide coated sand treating ground water by SEM and EDS. O'Reilly and Hochella (2003)[42] used field emission scanning electron microscopy FESEM and EDS for analyzing the lead sorption per specific surface area of natural and synthetic manganese and iron oxides. Kim and Jung (2008)[43] performed SEM observations of coatings and filter media while investigating the soluble Mn removal by uncoated sand, manganese oxide coated sand MOCS, a combination of uncoated sand and MOCS, and granular activated carbon. Tobiason et al. (2008)[9] performed extensive investigations using imaging and chemical capabilities of SEM with EDS for analyzing coatings on filter media from several different full-scale treatment plants in US and UK, with special interest of transect analysis from cross-sections of coatings. SEM equipped with a field emission electron source could provide the image resolution around few nanometer; however, the initial coating formation process appears to occur less than few nanometer scale range.

Since obtaining local chemistry and crystal structure information with few nanometer spatial resolution is very challenging for both SEM and EPMA, transmission electron microscopy

(TEM) based characterization has recently emerged. TEM is a very powerful tool for nanoscale evaluation, whereas preparing a sample from wet, poorly crystalline, loosely bonded surface coating remains technically challenging and painstaking. Thus, only handful TEM based studies to provide information regarding MnO_x(s) phases present in coatings have been published so far. Still, several important characteristics of the MnO_x(s) coatings such as possible constituent MnO_x(s) phases have been reported (Villalobos et al., 2003, Fendorf et al., 1992, Hem and Lind, 1983, Zhu et al., 2012, Manceau et al., 2013)[22, 31, 44-46] Villalobos et al. (2003)[46] obtained morphological and structural information by TEM while characterizing and comparing the manganese oxide produced by Pseudomonas putida strain MnB1 with synthesized triclinic birnessite, "c-disordered" H^+- birnessite, delta birnessite and acid birnessite. Fendorf et al. (1992)[45] utilized high resolution TEM images to show the importance of considering surface precipitates formation on oxide surface while modeling sorption mechanisms of hydrolyzable metal ions on oxide surfaces. They showed an amorphous surface precipitate formed on a birnessite phase. Hem and Lind (1983)[22] imaged with TEM the different manganese oxides products of the reaction of air with 0.01 molar solutions of $MnCl_2$, $Mn(NO_3)_2$, $MnSO_4$, and $Mn(ClO_4)_2$ while validating a nonequilibrium thermodynamic model for predicting forms of precipitated manganese oxides. Zhu et al. (2012)[31] pursued TEM observations to complement their modelling efforts using atomic pair distribution function analysis in elucidating the microstructure of biotic and abiotic poorly-crystalline manganese oxides including acid birnessite, delta birnessite, polymeric birnessite, and bacteriogenic manganese oxide. Manceau et al. (2013)[44] used high resolution TEM to image morphological microstructure of turbostratic delta birnessite nanosheets in order to complement their modeling efforts using high-energy X-ray scattering data in understanding the short- and long-range structure of this phase.

In spite of extensive previous surface characterization analyses (Merkle et al., 1996, Tobiason et al., 2008, Cerrato et al., 2011)[9, 28, 37], the efforts to elucidate the initial formation mechanisms have been maldistributed in macro-, meso-, and micro- meter scale ranges. Therefore, by using

multi-scale characterization techniques, this study systematically explores the role of filtering media structure, chemistry, and surface topography at the micro and nanoscale on the initial $MnO_x(s)$ coating formation under different inorganic aqueous synthesis conditions.

1.2. Experimental methods

1.2.1 Bench-scale column experiments

Bench-scale column experiment method is commonly used for analyzing filtration processes in controlled conditions [18]. In this study, to evaluate the role of characteristics of media on the formation of the initial $MnO_x(s)$ surface coating layer, six columns were operated first using three different filter media for the porous filter system:

1) Silica sand, which is of standard use in water filtration: Filtersil 0.50, Unimin Corp., Ottawa, MN; quartz sand with size range between 0.425 – 0.850 mm.
2) Amorphous borosilicate glass beads: Cataphote Corp., Jackson, MS; amorphous silica beads with size range between 1.5 – 3 mm in diameter.
3) High purity alumina spheres: T-99 PROX-SVERS®, Christy® Catalytics, Saint Louis, MO; catalyst support α- alumina spheres with two sizes: 1.6 and 3.2 mm in diameter.

Inorganic conditions typical of fresh water treatment plants were used in this study. Free chlorine was present across the filter bed and acted as the primary oxidant in all experiments. Aluminum sulfate (Alum) was added for simulating the coagulation step prior filtration carried out in many water treatment plants. The addition of Alum formed around 10% of hydrolyzed species and about 90% of precipitated aluminum hydroxide ($Al(OH)_{3(s)}$) under the experimental conditions of this study[47]. In this document, any mention to Al in water will refer implicitly to the occurrence of these species. The feed solution was prepared using distilled water with 1 meq/L $NaHCO_3$ alkalinity as a source for background ions. Borosilicate glass columns (7/16” inner diameter) were operated at

an hydraulic load rate (HLR) of 4 gpm/ft^2, and a constant flow of 16 mL/min with a nominal Mn^{2+} influent concentration of 0.2 mg/L (200 ppb) -using manganous chloride-, in the absence and the presence of a nominal concentration of 0.220 mg/L (220 ppb) of Al, prepared from aluminum sulfate octadecahydrate (ACS grade, CAS Number 7784-31-8, Sigma-Aldrich, Inc.); and, subjected to a dosage of 4 mg/L of a solution of 12.5% of sodium hypochlorite yielding 2 mg/L (2 ppm) chlorine residual in the effluent as Cl_2. The mixing point of manganese stock solution and oxidant feed water was above each filter bed, so that the reaction time before reaching the bed was approximately 5 seconds. The bed length was 6". Oxic conditions were maintained: 8 mg/l dissolved oxygen (DO). pH was adjusted at a value of 7.3 and measured using a probe from Accumet© (Cat. No. 13-620-221) and a meter by Oakton© pH/mV/OC (110 Series, RS232). The desired pH value was achieved by additions of small aliquots of solutions of 1M NaOH and 1M HCl as required. The calculated ionic strength of each starting feed solution when mixed -solutions bearing either only Mn (Mn-only) and a combination of Mn and Al (Mn-Al)- was generally less than 0.00213 M and 0.00214 M respectively.

Each column was monitored for the effluent Mn concentration and operated arbitrarily for six days (the Mn effluent concentration usually stabilized at this time). Some media granules were retrieved from each column at the end of each trial by evacuating the remaining water and pouring carefully the media bed on a tray covered with aluminum foil, forming a line from bottom to top. Then, media samples were taken from the top 1-inch and bottom 1-inch of the column. Both influent and effluent concentrations of Mn, Al, Ca, Fe, Si and Na were also monitored by taking water samples at the inlet and outlet connections to each of the six columns.

For comparing the evolution of surface coating on amorphous (silicate glass) versus crystalline (silica sand) media, four additional columns were operated and samples were retrieved from the top of each column after 1 hour, 6 hours, 12 hours, 1 day, 3 days, 4 days and 6 days of starting each experiment.

To evaluate changes in surface coating development based on the sequential change of influent water chemistry, two additional columns were operated in parallel for 18 and 15 days with sequentially changing the solution composition as a function of time. The influent solution sequence used for each of these columns is presented in table 1.1. The filter media used were UV-resistant clear extruded acrylic spheres of 1.6 mm in diameter (Catalog # 1383K41, McMaster-Carr, Princeton, NJ). Notation for coatings formed in the presence of a manganese only (Mn-only), aluminum only (Al-only), and a combination of manganese and aluminum (Mn-Al) solution is maintained. Granules of coated media were retrieved directly from the columns as required for characterization.

For further details regarding the operational conditions of the column experiments performed in this study, refer to (Hinds, G., 2015)[47]

Table 1.1. Sequence of solution composition applied to two column filters in parallel using acrylic spheres as media.

Column Operation time (days)	3	3	2	1	3	3	3
Column A	Al - only	Mn - Al	Al - only	Mn - Al	Al – only	Mn - only	Mn – Al
Column B	Mn - Al	Al – only			Mn – Al	Mn - only	

1.2.2. Inductively coupled plasma mass spectrometry

The chemical composition of the influent and effluent water from the column was determined using inductively coupled plasma - mass spectrometry (ICP-MS). The residual soluble Mn concentration was monitored under the assumption that colloidal $MnO_x(s)$ were neither formed nor present in the influent or effluent solutions. The instrument (Thermo Electron Corp. X Series

ICP-MS, X-0458) has a detection limit for Mn of 0.1 µg/L. All measurements conformed to the ICP-MS method outlined in Standard Methods 3125-B (21st ed., 2005).

1.2.3. Powder X-Ray Diffraction

The mineralogy of the surface coatings and substrates was determined by powder X-Ray Diffraction (XRD) analysis. Samples were prepared by removing the coating from filter media surface by gentle rotation of filter media in distilled water using Single Tier Roll Jar Mill (U.S. Stoneware, East Palestine, OH) at 150 rpm for 3 hours. The resulting suspension was recovered and then vacuum dried. The obtained dry samples were softly crushed to powdery form and then analyzed with a Rigaku MiniFlex II X-ray diffractometer equipped with a Cu Kα (λ=1.5406 angstroms) source, operated at 30 kV and 15 mA. Scans were performed from 5° to 80° at a step size of 0.2°, dwell time of 20 s per step with sample rotation. A Si low-background plate was used to minimize background contributions.

1.2.4. Synchrotron X-Ray Diffraction

Synchrotron X-ray diffraction (SR-XRD) data of the dry powders prepared by a gentle coating removal protocol, followed by vacuum-drying and crushing as specified in the section above and loaded in 1 mm O.D. Kapton capillaries were collected at the beamline 11-ID-B [~58 keV, λ = 0.2114 Å] of the Advanced Photon Source, Argonne National Laboratory (APS-ANL, Argonne, IL). An amorphous Si area detector system (Perkin Elmer) was used for data collection[48]. A CeO2 standard (NIST diffraction intensity standard set 674a) was used to calibrate the sample-detector distance and nonorthogonality of the detector relative to the incident beam. Conversion of data from 2D to 1D was performed using Fit2D[49]. The background intensity measured for a blank (empty) capillary was subtracted from data for each sample using Excel.

1.2.5. X-Ray Photoemission Spectroscopy

X-Ray Photoemission Spectroscopy (XPS) was performed to identify the oxidation state of Mn on the top surface of the coating by analysis of the position and shape of the Mn 3p photoline as described by Cerrato et al.[37] Coated filter media granules were mounted on a glass slide using adhesive carbon tape and analyzed using a Phi Quantera HR SXM-03 Scanning X-ray Photoelectron Spectrometer (XPS) Microprobe (ULVAC-Phi Ind.) under vacuum at or below 5×10^{-8} Torr. This instrument uses a monochromated Al-Kα (energy of 1486.7 eV) source and a 32-channel detector. The anode was operated at 15kV and 50 W. The spot size for this analysis was 200 µm. Binding energy values were charge referenced to the adventitious C 1s peak position at 284.8 eV. XPS spectra were recorded for survey wide scans with a pass energy of 280 eV and a step size of 1 eV; meanwhile, a pass energy of 26 eV and a step size of 0.1 eV was used for high resolution scans. Data were background subtracted using a Shirley algorithm, and curve fitting was performed by restricting the peak shape, peak position, and FWHM of the standards for Mn(II), Mn (III), and Mn (IV) presented by Cerrato et al. [37] and NIST Data (http://srdata.nist.gov/xps/Default.aspx). The FWHM parameters were previously optimized in order to allow/reflect changes of the local environment of the oxidized species in the samples as suggested by other authors[39, 50]. A slight modification of the Gaussian – Lorentzian Asymmetric algorithm involving a change of the tail-modifier was pursued improving the goodness of fit. Areas under the curve were kept the same. These results were obtained from within a typical analytical depth roughly 5 nm from the surface, considering the characteristics of the materials and the energies of the Mn photoelectrons[37]. Parameters used are presented in table 1.2. The atomic concentrations were obtained by multiplying the background subtracted photoelectron peak areas by their relative sensitivity factor.

Table 1.2. Gaussian-Lorentzian asymmetric line shape parameters used for the reference photopeaks of Mn(II), Mn(III), and Mn(IV) standards.[37].

Standard	Peak position (eV)	FWHM (eV)	Lorentzian asymmetric line shapes parameters	
			% Gaussian	Exponential Tail Modifier
Mn (II)	47.99	1.07	88	1.15
Mn (III)	48.43	1.73	96	1.15
Mn (IV)	49.51	1.64	85	1.15

1.2.6. Atomic Force Microscopy

Atomic Force Microscopy (AFM) was supplementary used to examine the surface topography and measure surface roughness of filter media. AFM uses a sharp tip to probe the surface of filter media by raster scanning its surface. Samples were mounted with double-sided adhesive carbon tape to a flat AFM sample disc and probed using a Veeco multimode atomic force microscope (Veeco Metrology, Santa Barbara, CA) in contact mode with a silicon nitride tip (DNP-S10, Bruker Corp.). Analysis of the AFM images was performed using the Digital Instruments, NanoScope IVa software.

1.2.7. Optical and Electron Microscopy

Optical Microscopy (OM) was used to observe macroscopic features (morphology and topography) of the uncoated and coated media from few mm to hundreds of μm without depositing conductive coating on the samples' surface prior to observation. Samples for OM were air-dried, mounted on aluminum pins by silver paste, and observed in a Carl Zeiss Axio Scope.A1 Pol Hal 100 optical microscope.

Scanning Electron Microscopy (SEM) with Energy Dispersive X-ray Spectroscopy (EDS) was used to characterize elemental composition, structure, morphology and topography of Mn

oxides formed on filter media, as well as the bare surface of filter media at the micro- and meso-scale. SEM analysis was performed on the same OM samples. When samples showed image distortions due to extremely poor electron conductivity, the sample surface was coated with an around 10 nm thick Au-Pd. An FEI Quanta 600 with a Schottky field-emission electron source and a Bruker Silicon Drift EDS Detector model XFlash 4010 was used to image all the samples with an accelerating voltage of 10 kV, working distance of around 10 mm, and an Everhart-Thornley detector.

Transmission Electron Microscopy (TEM) samples were prepared by gently scrapping the coating off the top of the filter media particle using a sharp blade, capturing the removed layer on top of a Cu grid with double-layer carbon support film; less than 5nm continuous carbon film which is mounted on a carbon holey film. For cross-section analysis of MnO_x(s) coating development by varying solution composition, acrylic spheres filter media granule with surface coating were sliced to a thin foil of approximately 100 nm in thickness using a RMC Power Tome PC microtome with a cutting velocity of 0.9 mm/s and a DiATOME ultra 35° wet diamond knife, No. MT 10117, and size 4.0 mm. TEM characterization (imaging, electron diffraction and EDS) was performed on a thermionic emission JEOL 2100 with a JEOL genuine 60 mm^2 Silicon Drift EDS Detector (SDD-EDS), operated at 200 kV. A JEOL ARM200CF (at the Ultramicroscopy Research Center, Kyushu University) operated at 30kV was also used for imaging and electron diffraction where particularly specified. This instrument is equipped with a cold-Field Emission Gun electron source, two hexapole-type spherical aberration correctors, and two 100 mm^2 SDD-EDS detectors.

1.2.8. Numerical modeling parameters

The main parameters used for pursuing the numerical modeling exercise in chapter 4 are summarized in table 1.3. The extended DLVO model used was developed by Shen et al. (2012)[25], considering that the calculated interaction energies reflect the preferred location of MnO_x(s) nanoparticles attached to a rough surface.

Table 1.3. Principal parameters required for calculating interaction energy curves according to the rough surface model by Shen et al. (2012)[25]. This model is based on the extended DLVO theory.

Parameter	**Units**
Hamaker constant A_{123} considering colloid, medium, collector	J
Asperity/protrusion radius a_g	nm
Colloid/nanoparticle radius a_p	nm
Dielectric characteristic wavelength λ	nm
Permittivity of vacuum $\boldsymbol{\varepsilon_0}$	$C^2J^{-1}nm^{-1}$
Relative permittivity of water $\boldsymbol{\varepsilon}$ (@25°C)	-
Reciprocal double layer thickness κ	nm^{-1}
Zeta potential of the colloid $\boldsymbol{\psi_p}$	V
Zeta potential of the asperity $\boldsymbol{\psi_g}$ equal to zeta potential of the surface $\boldsymbol{\psi_s}$	V
Collision parameter σ	nm

1.3. Objectives

This work aims to understand the role of filter media characteristics on the initial MnO_x(s) surface coating formation under similar inorganic conditions of fresh water treatment facilities. By using advanced multi-scale characterization techniques, this study systematically explores the role of filtering media structure, chemistry, and surface topography at the micro and nanoscale on the initial MnO_x(s) coating formation under different inorganic aqueous synthesis conditions. Results obtained will be compared with a suitable model that can predict the initial MnO_x(s) coating location on the filter media surfaces.

The specific objectives of this study are to:

- Investigate the role of filter media's micrometer scale surface topography, crystal structure and chemistry on the initial $MnO_x(s)$ coating layer formation on the bare surface of filter media, Mn uptake, and coating evolution under different inorganic aqueous synthesis conditions.
- Analyze the coating's crystal structure and identify phases and morphology at the micro and nanometer scale.
- Model how surface coating formation occurred and its correlation with experimentally observed physical characteristics. This modeling exercise attempts to asses the favorable locations of initial $MnO_x(s)$ coating formation.
- Provide experimental-based explanations of the formation mechanisms of $MnO_x(s)$ surface coatings at the nanoscale.

CHAPTER 2. Influence of filter media characteristics on the formation of manganese oxide nanoparticles and films during water filtration: micrometer scale experimental investigation of coating evolution.

2.1. Summary

The influence of micrometer-scale surface topography, crystal structure, and chemistry of fresh water filter media on the initial MnO_x(s) coating formation and soluble manganese removal mechanisms was investigated. A series of Bench-scale column experiments was conducted to develop MnO_x(s) coating layers on the surface of different filter media by simulating the inorganic aqueous chemistry of a typical coagulation fresh water treatment plant where free chlorine is present across filter bed. Scanning electron microscopy (SEM) observations demonstrated that both surface roughness and granule morphology are major contributing factors to the MnO_x(s) coating formation and soluble manganese removal processes. A greater amount of coating was developed on rougher areas. In contrast, filter media's crystal structure and crystallinity (crystalline vs. amorphous) has no impact on the coating formation. In addition, the role of Al species for simulating pretreated water conditions -previous coagulation steps- with varying filter media material was clarified. Al species destabilized the small amount of MnO_x(s) nanomaterial formed in the filter-applied water due to oxidation of soluble manganese by free chlorine, enhancing its deposition on the media and increasing soluble Mn removal. Through the analysis of the factors improving the manganese removal process, a model for the initial MnO_x(s) coating formation was proposed. In terms of factors affecting the proposed model, the characteristics of filter media (elemental chemistry and surface morphology) were found to be most influential.

Depending on the elemental chemistry of the media, different $MnO_x(s)$ phases were formed. Moreover, depending on the elemental chemistry and surface morphology of filter media, local conditions for particle-media interactions are thought to change, impacting on the attachment behavior of particles with respect to filter media. Finally, it was demonstrated that the addition of Al to the water promotes the formation of the delta birnessite phase regardless of filter media type.

2.2. Results

2.2.1. Solution chemistry

Removal of soluble manganese (Mn^{2+}) by different fresh filter media in the presence and the absence of Al is shown in Figure 2.1. In this work, the main hypothesis is that some of the soluble Mn in the influent water is oxidized by free chlorine, forming nanosize $MnO_x(s)$ material that simultaneously enters the filter bed in conjunction with the remaining soluble Mn. In contrast, it is assumed that in the effluent water only soluble manganese exists. In addition, it is also hypothesized that Al species in water destabilize this $MnO_x(s)$ nanomaterial, enhancing its deposition on the media. The curves represented the normalized residual of soluble manganese as a function of processing time. This figure shows the efficacy of the different filter media at removing soluble manganese increases in the following order: glass, alumina, and silica sand. Also, the addition of Al to the influent water significantly increases the soluble manganese removal rate by more than 50 % regardless of the filter media used.

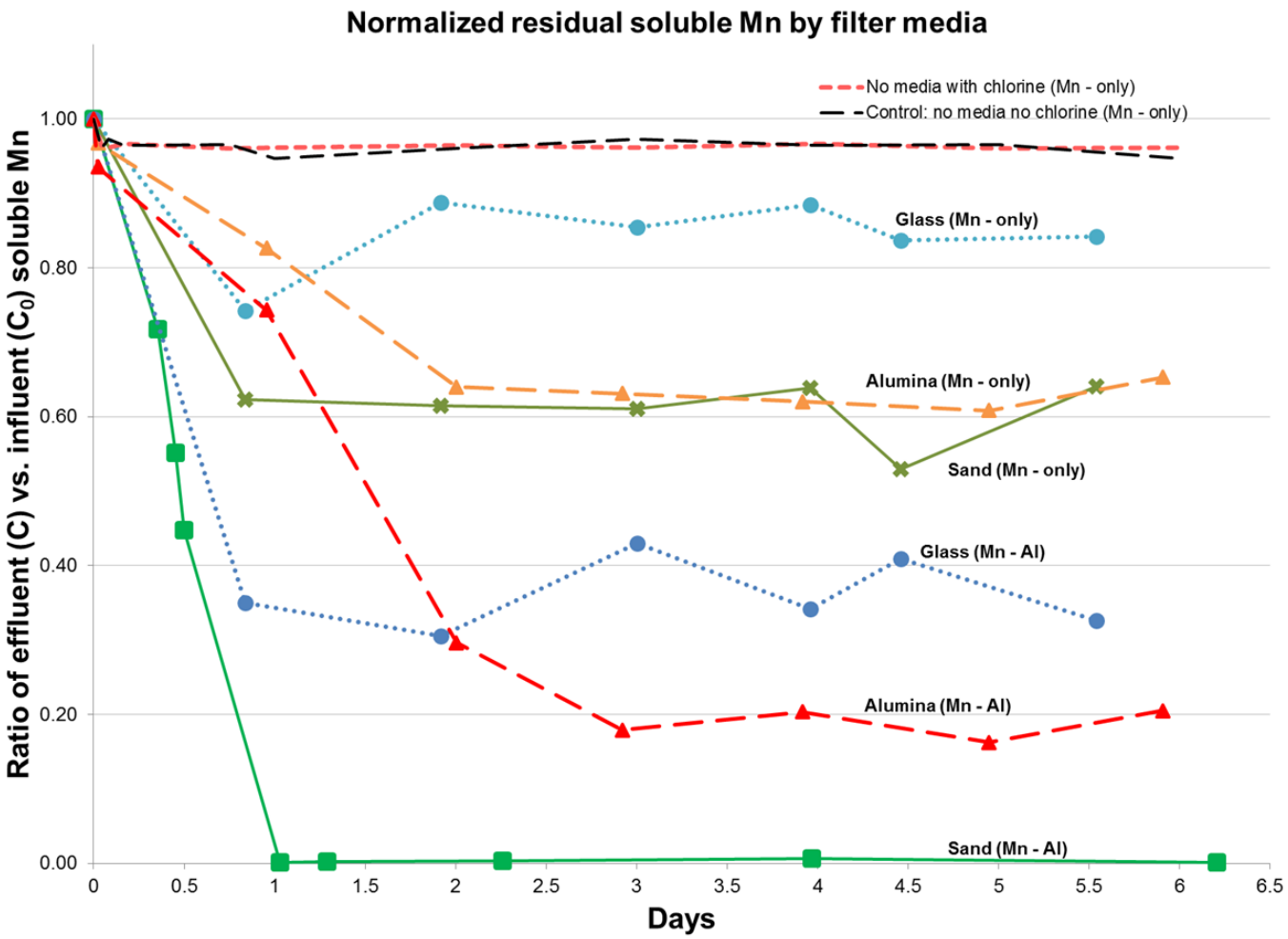

Figure 2.1. Soluble Mn^{2+} removal by different filter media in a porous filter having free chlorine as oxidant across the bed in the absence and the presence of Al.

In this study, filter media have only trace amounts of impurity elements on their bare surface, which is reported by the manufacturer and confirmed by SEM-EDS analysis. Hence, any compounds found in the coatings must necessarily originate from the components delivered by the influent water. Typical elemental chemistry of the influent water is presented in table 2.1. As expected, only trace amounts of other elements apart from Mn and Al are present in the prepared water, avoiding possible complicating effects caused by chemical species other than the ones controlled in the influent water and filter media. This facilitated elucidating the mechanism of coating formation, as well as coating structure determination.

Table 2.1. Typical elemental chemistry of influent feed solution in column experiments. Solutions were prepared by mixing distilled water with alkalinity -NaHCO3-, dosed with nominal 200 ppb Mn^{2+}, with and without addition of nominal 220 ppb Al in the presence of sodium hypochlorite solution, and pH adjusted by HCl or NaOH to 7.3. Units are in (micrograms/Liter).

Species	Nominal 200 ppb Mn2+ influent solution	Nominal 200 ppb Mn2+ added 220 ppb Al influent solution
Mn	215.40	221.50
Al	1.55	222.50
Ca	5.14	3.86
Fe	<0.06	<0.06
Si	<0.05	<0.05
Na	20030.00	19740.00

2.2.2. Phase identification

Powder XRD results of the solid surface coatings retrieved from the different filter media and calculated candidate phases are shown in figures 2.5 to 2.10. It should be noted that all the spectra taken from solid surface coating materials contains some amount of crushed filter media. The background of the experimental spectra was mathematically removed by using the background spectrum obtained from the Si zero-background plate used for all the measurements with the same experimental setup and conditions. Experimental peaks in each pattern were indexed initially by automated search algorithms using the Rigaku PDXL Software Version 1.8.0.3. Afterwards, suggested phases were manually reselected from the candidates by first considering only the ones containing combinations of the major elemental constituents in the system (Mn, Al, Si, O), while focusing on the peak position and intensity, taking into account possible small divergences on these values. More specifically, $MnO_x(s)$ species known to be stable at our experimental conditions were primarily selected. The powder diffraction pattern database by the International Center for Diffraction Data (ICDD, formerly, the Joint Committee on

Powder Diffraction Standards, JCPDS) was used primarily for the reselection. Since only a limited number of poorly crystalline manganese oxide crystal structures are available in this database, and the major phases with similar diffraction patterns that could exist under our experimental conditions are birnessite and their derivatives, structure information from several birnessites from Zhu et al. (2012)[31] and Bricker, O. (1965)[30] was also used. Finally, phases were identified by matching the experimental peaks obtained from each sample with the peaks of standard species taking into account both the position in the spectra and the relative intensity of peaks.

To distinguish multiple phases, several characteristic interplanar spacings for each phase (1.4 Å for birnessite, 7.2 Å and 3.6 Å only for hexagonal birnessite; 4.7 Å, 2.5 Å and 1.8 Å for pyrochroite; and, 4.7 Å, 4.4 Å, and 2.2 Å for bayerite) were utilized. XRD spectra from all the surveyed samples are presented in figures 2.2, and 2.5 through 2.10. General features of the observed spectra included very significant peak broadening with a large background intensity. Possible sources of peak broadening were in e.g. small crystal size, thermal diffuse scattering, crystal defects, etc., being the most important contributors: small crystal size, defective crystals, and the presence of a significant amount of amorphous material. Two main types of layered Mn-Ox structures in these samples were observed. XRD profiles for samples Mn-only on glass and Mn-only on sand have the basal plane spacing that is characteristic of a hexagonal birnessite-like structure. Samples Mn-Al on glass, Mn-Al on sand, Mn-only on alumina, and Mn-Al on alumina all show XRD features that are not consistent with hexagonal birnessite, but instead appear to match a trigonal-hexagonal structure similar to that of pyrochroite ($Mn^{2+}(OH)_2$). This is suggested by the major XRD peak centered at an interplanar spacing of 4.72 Å that corresponds with the basal plane spacing in pyrochroite. Although it is not a perfect match, several other features (e.g., 2.45 Å) also agree well with the observed data if broadening is considered. In figure 2.2, synchrotron and powder XRD spectra from Mn-Al on glass, powder XRD spectrum from Mn-only on glass, and calculated XRD patterns for pyrochroite and hexagonal birnessite are presented as example. As XPS data in Chapter 3 show very small detectable Mn^{2+} in sample Mn-Al on glass, it appears that

the Mn-Ox phase in this and several of the other samples is either feitknechtite ($Mn^{3+}O(OH)$) which is isotypic with pyrochroite[51] or some other oxidized Mn phase in combination with another Mn^{4+}-containing phase that is not yet identified. Although it is likely a layered structure, it is difficult to identify it as birnessite because of the absence of the large basal plane spacing (which could be missing because of turbostratic disorder) and because of the mismatch between the observed data and the other calculated XRD peaks shown in figure 2.2 (e.g. 3.68 Å). The structures of birnessite and pyrochroite are also shown in figures 2.3 and 2.4.

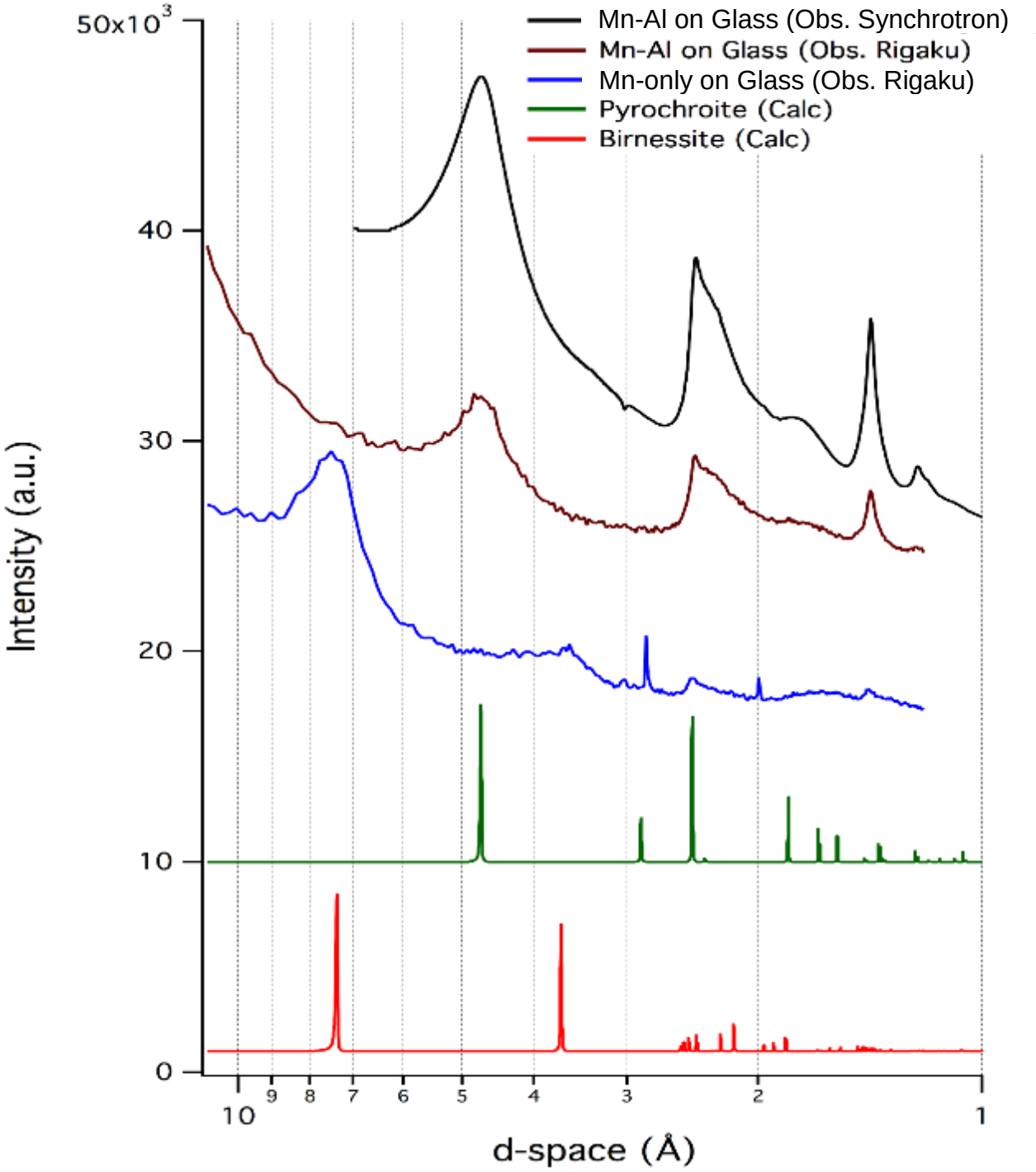

Figure 2.2. Observed XRD data for Mn-Al on Glass (both synchrotron and powder data shown) and Mn-only on Glass. Calculated patterns for pyrochroite and birnessite.

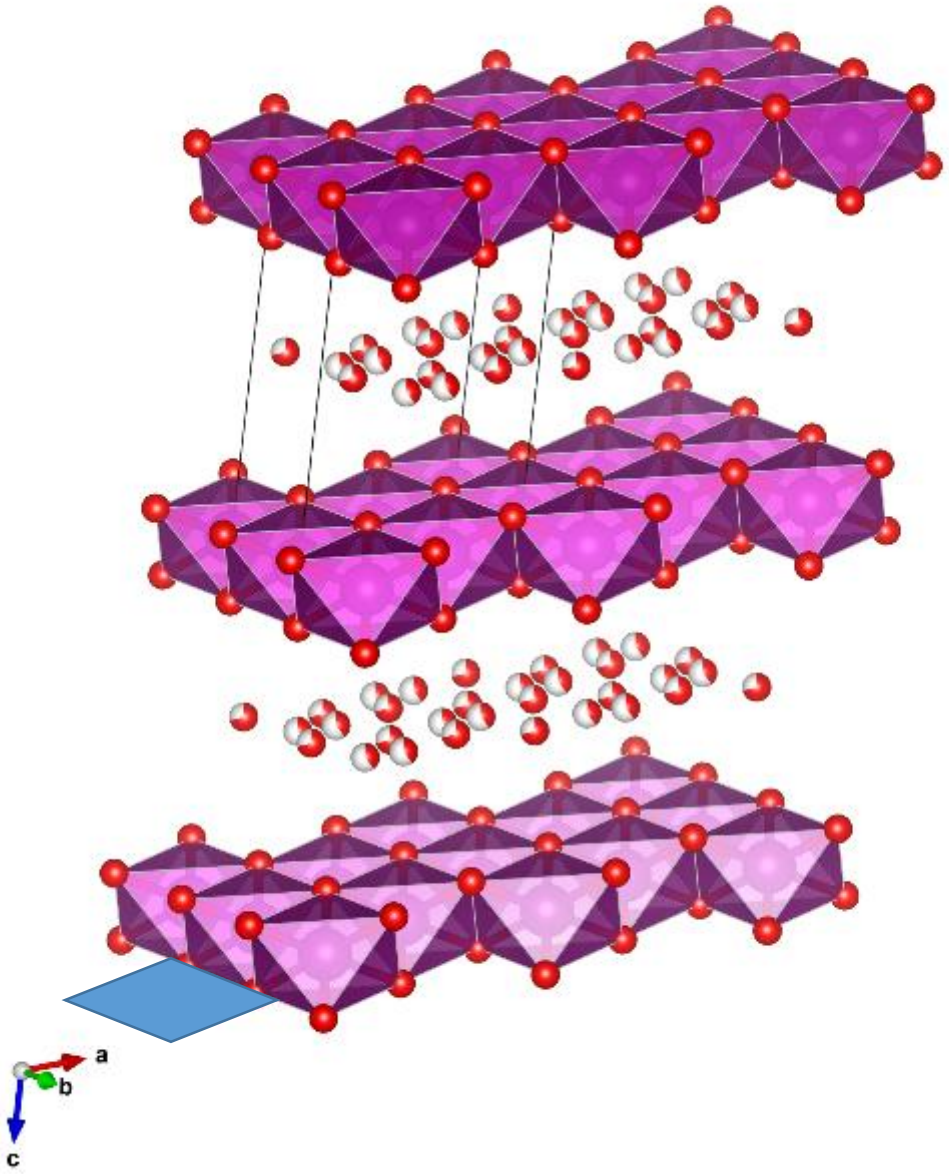

Figure 2.3. Layered birnessite structure. Red balls are octahedral oxygens and purple ones are manganese. MnO_6 octahedra (purple) form the different layers. Interlayer oxygens (red and white balls) can be water molecules or can be replaced by cations. The basal plane (blue) is oriented perpendicular to the c direction and expands on the a and b directions. Basal interplanar spacing is approximately 7.36 Å.

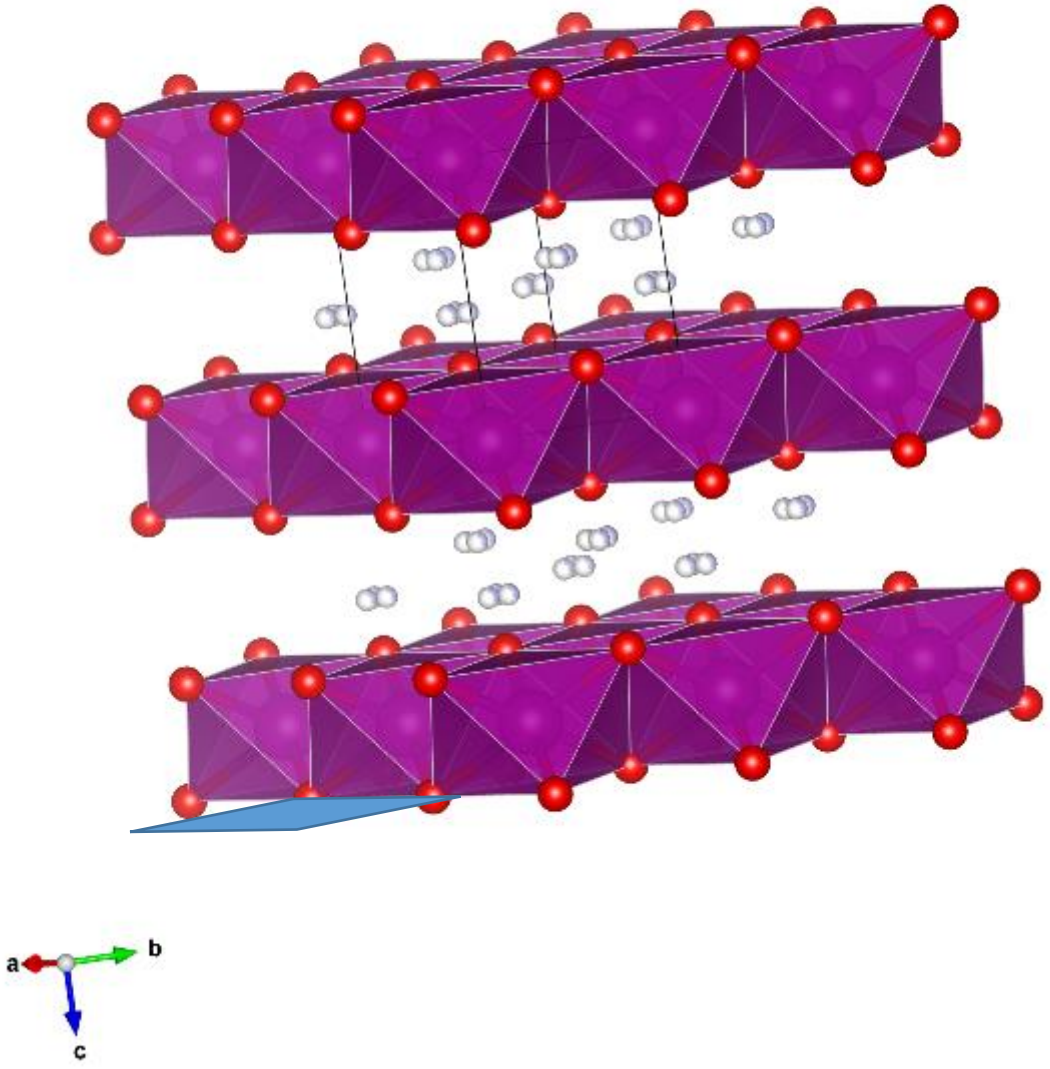

Figure 2.4. Layered pyrochroite ($Mn(OH)_2$) structure. This phase is isotypic with feitknechtite ($Mn^{3+}O(OH)$). Red balls are octahedral oxygens and purple ones are manganese. MnO_6 octahedra (purple) form the different layers. Interlayer atoms are hydroxyls (white balls). The basal plane (blue) is oriented perpendicular to the c direction and expands on the a and b directions. Basal interplanar spacing is approximately 4.72 Å.

In Table 2.2, a summary of identified and suggested phases is presented. Hexagonal birnessite was identified as the predominant phase in Mn-only coatings on glass and alumina. All other coatings have multiple poorly crystalline phases suggested to be either feitknechtite or another oxidized Mn phase (probably hausmannite), and a turbostratically dirsordered birnessite (δ - birnessite). The crystal structure of filter media (amorphous vs. crystalline) is also confirmed in figures 2.5 through 2.10. Silica sand and alumina media presented crystalline peaks, meanwhile glass media showed only a large hump indicating its amorphous nature. In figure 2.10, bayerite (sharper peaks) was confirmed as minor phase in the Mn-Al on alumina sample, which was not present in the Mn-only on alumina sample. The synthetic birnessites -hexagonal–MnO_2 and δ–MnO_2 - are considered as standard candidates for identification purposes. They are both layered phyllomanganates with hexagonal point group symmetry. They are structurally very similar to each other, but with different octahedral sheet stacking order along the c-axis. δ–birnessite has nearly randomly stacked octahedral sheets which causes the lack of the (001) reflection in its XRD spectrum, whereas the (001) reflection is a characteristic identification of hexagonal-birnessite. Also, the chemical composition of these synthetic model birnessites is reported to be MnO_2•$0.56H_2O$ for hexagonal-birnessite and $Na_{0.07}K_{0.05}MnO_2 \cdot 0.44H_2O$ for δ-birnessite[31]. Bayerite ($Al(OH)_3$) is noted as the principal solid phase at the pH used for our experiments (pH 7.3) [17].

Because the majority of the phases found in the coatings on the filter media are poorly crystallized, refinement techniques could not be applied to the diffraction spectra. The lack of information regarding the correct peak shapes of the reference standards, knowledge of peak broadening of phases, and the volume ratio of amorphous and (poorly) crystalline material, etc., did not allow estimating the individual abundance/contribution of phases to the experimental spectrum. Therefore, only a qualitative distinction was possible, identifying predominant versus minor phases.

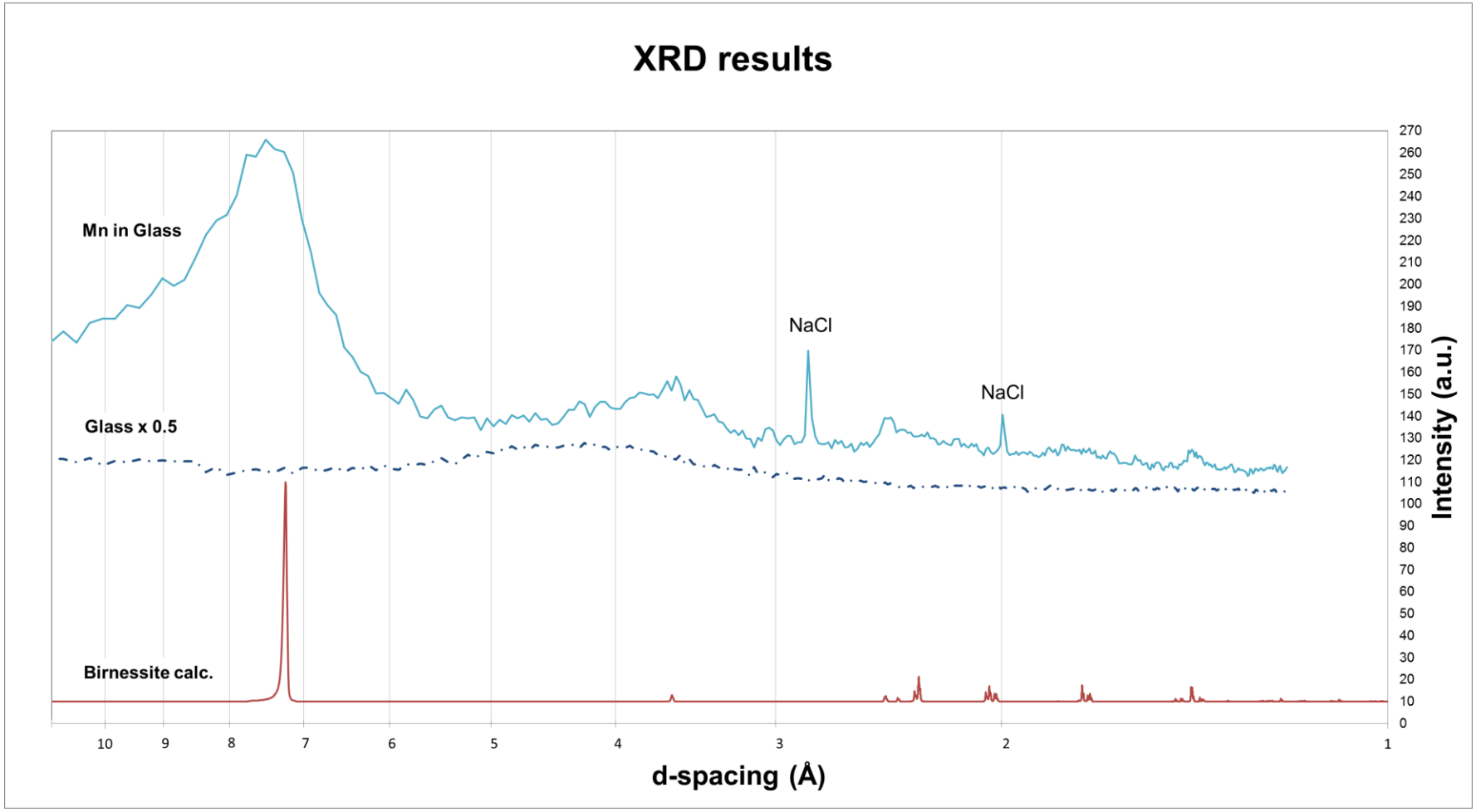

Figure 2.5. Powder X-Ray diffractograms of material dislodged from Mn-only coating on glass media, crushed fresh glass media, and calculated candidate phases. Peaks of sodium chloride (NaCl) are also identified. Spectra have been scaled down by the factor shown next to their name on label.

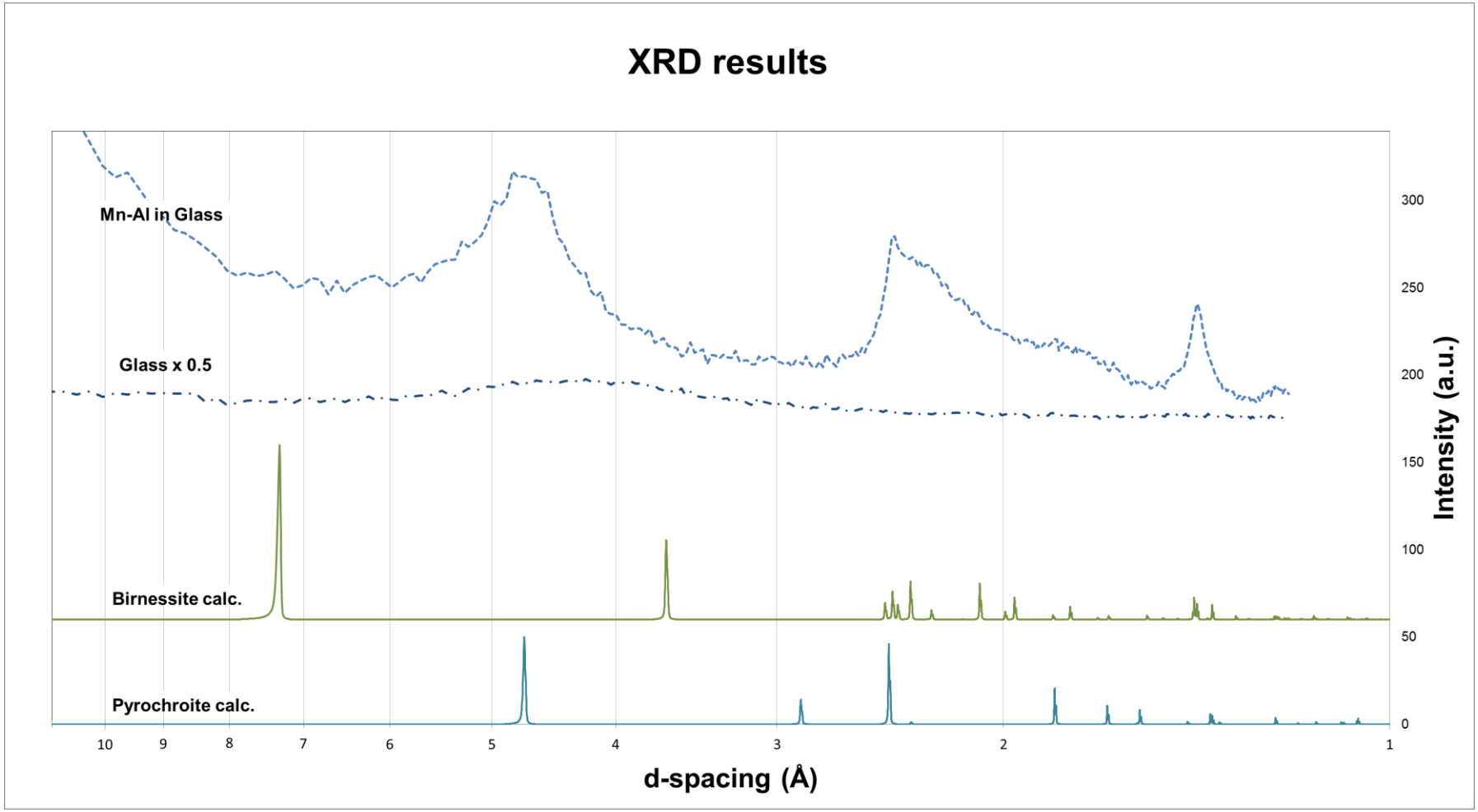

Figure 2.6. Powder X-Ray diffractograms of material dislodged from Mn-Al coating on glass media, crushed fresh glass media, and calculated candidate phases. Spectra have been scaled down by the factor shown next to their name on label.

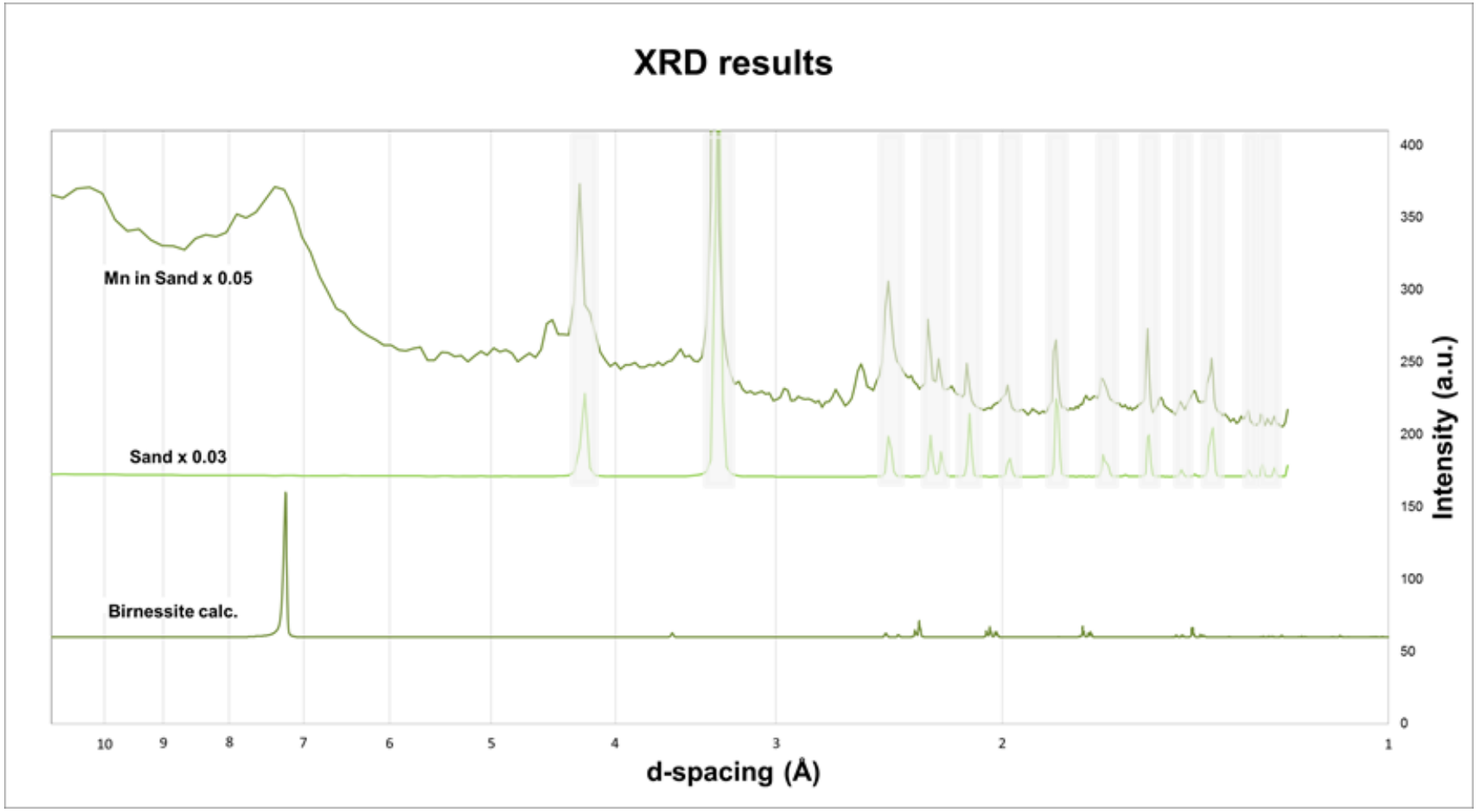

Figure 2.7. Powder X-Ray diffractograms of material dislodged from Mn-only coating on silica sand media, crushed fresh silica sand media, and calculated candidate phases. A minor crystalline phase is present, but has not been identified. Spectra have been scaled down by the factor shown next to their name on label.

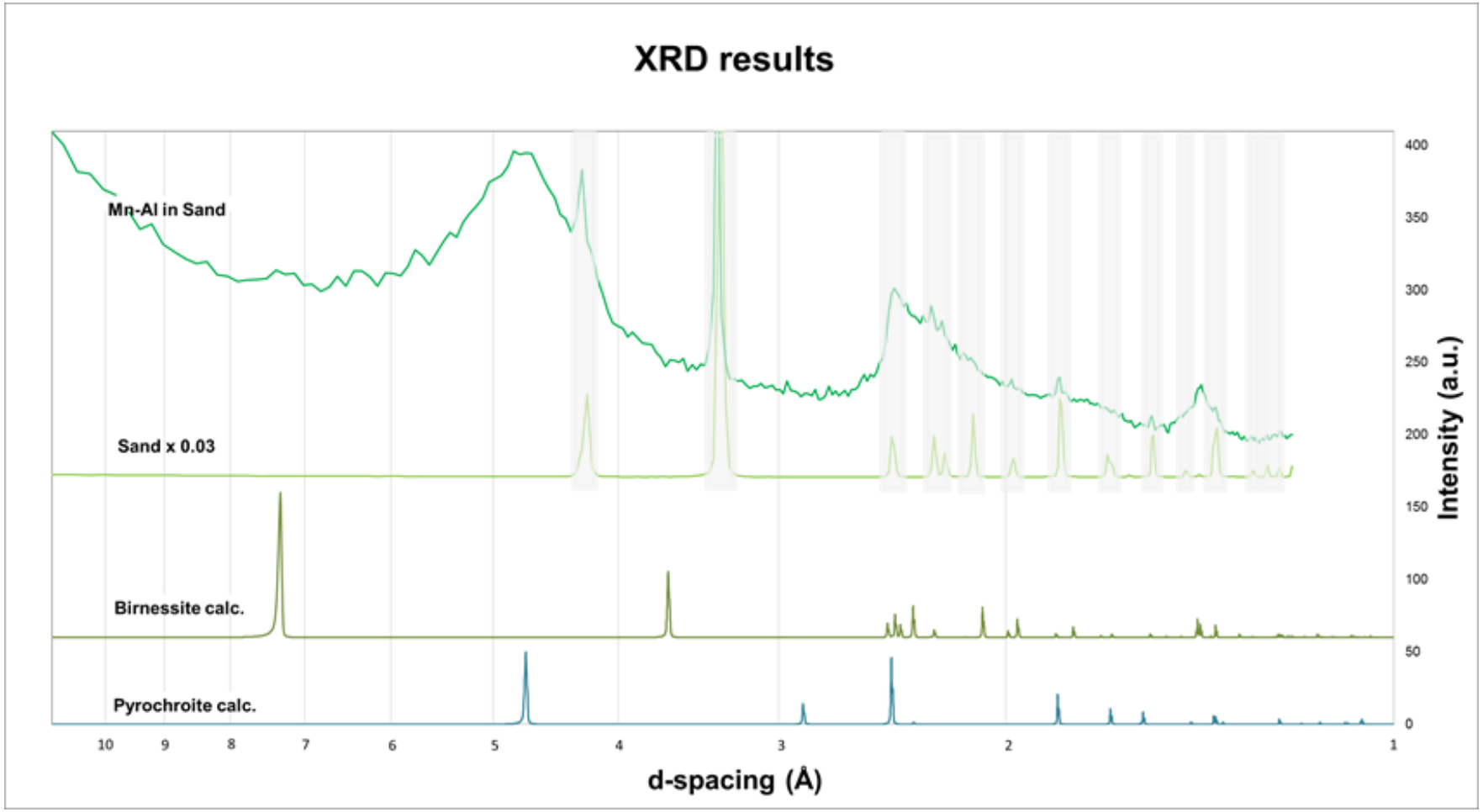

Figure 2.8. Powder X-Ray diffractograms of material dislodged from Mn-Al coating on silica sand media, crushed fresh silica sand media, and calculated candidate phases. Spectra have been scaled down by the factor shown next to their name on label.

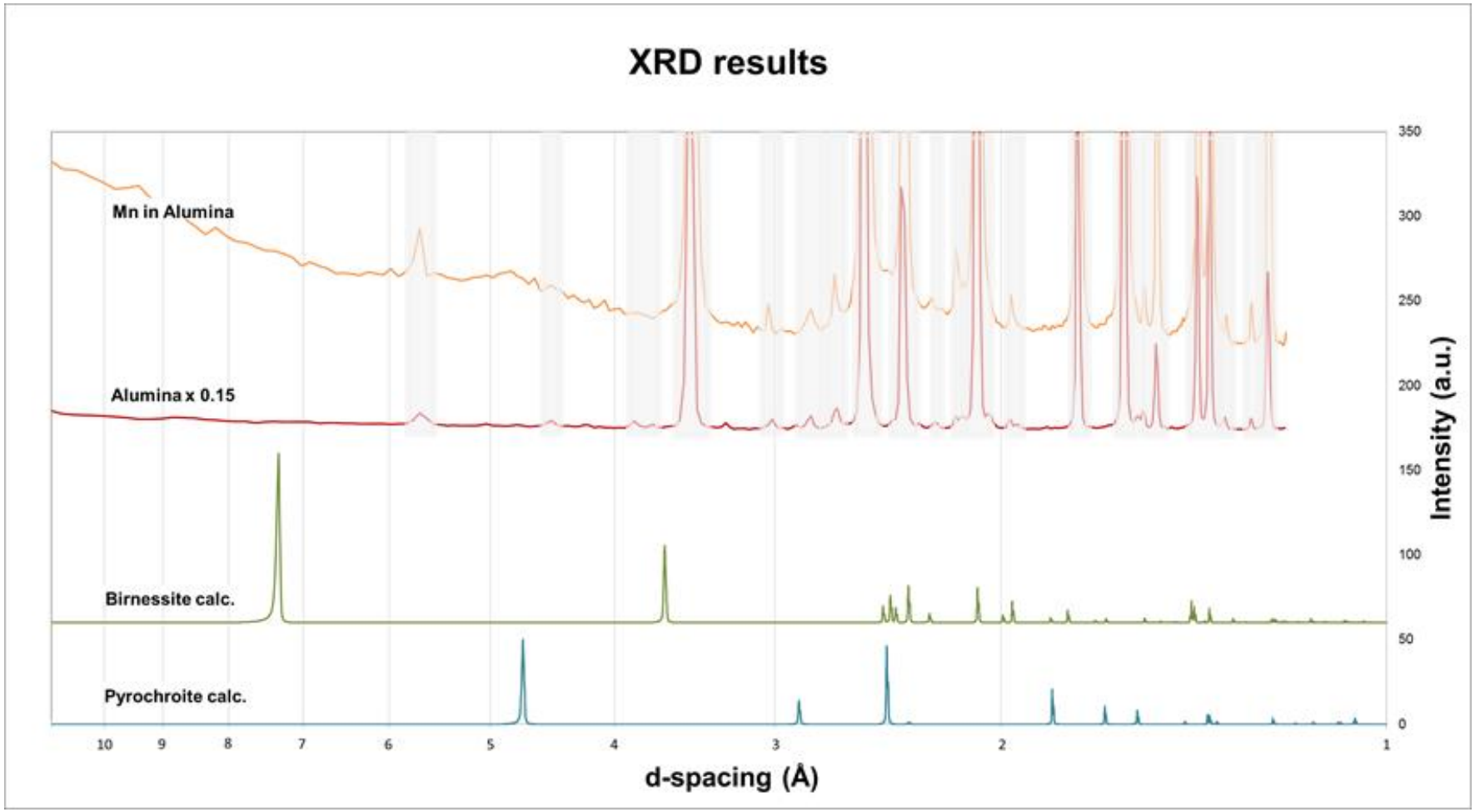

Figure 2.9. Powder X-Ray diffractograms of material dislodged from Mn-only coating on alumina media, crushed fresh alumina media, and calculated candidate phases. Peaks correlate well with correspondent media (alpha alumina). Spectra have been scaled down by the factor shown next to their name on label.

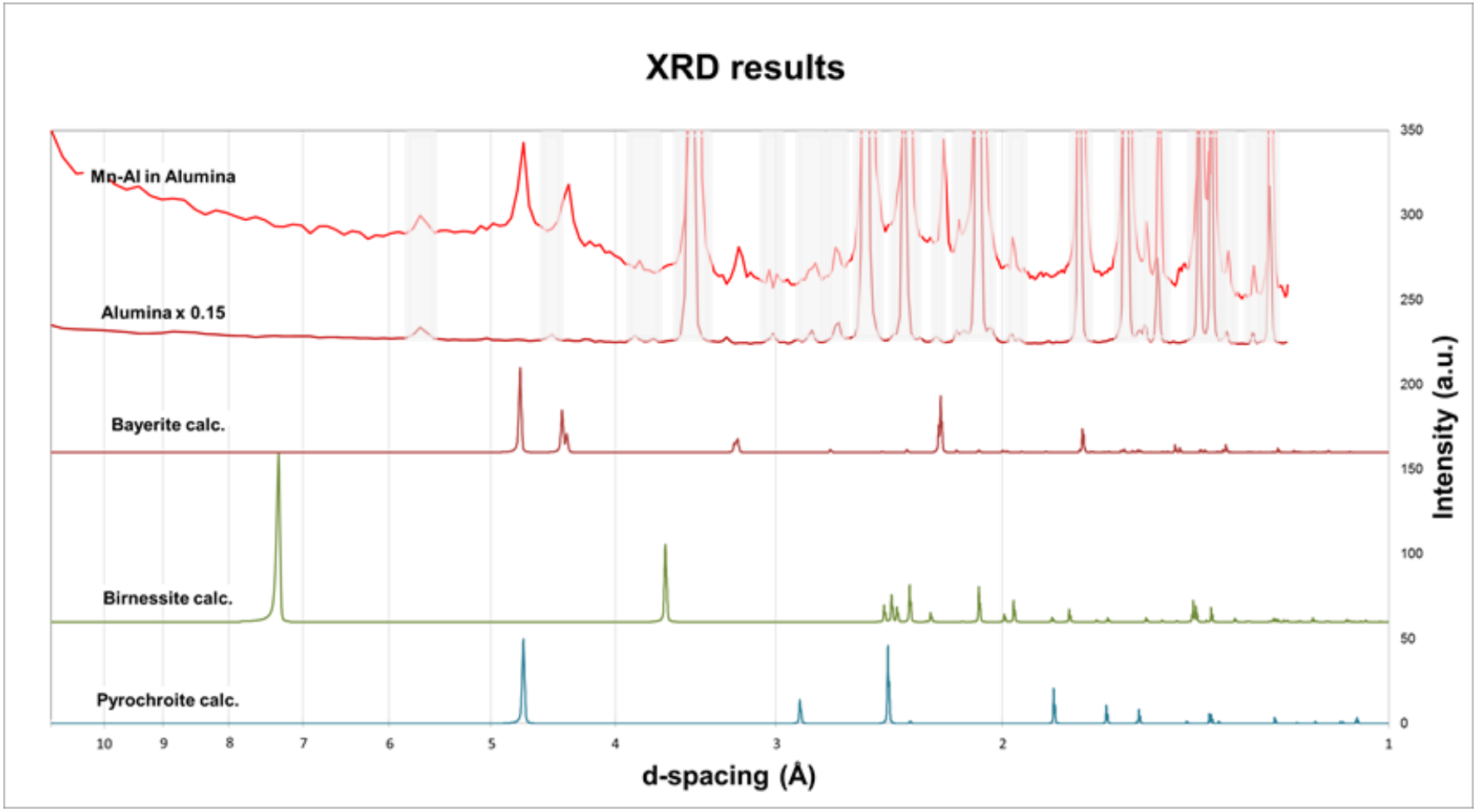

Figure 2.10. Powder X-Ray diffractograms of material dislodged from Mn-Al coating on alumina media, crushed fresh alumina media, and calculated candidate phases. Peaks correlate well with correspondent media (alpha alumina) and crystalline bayerite. Spectra have been scaled down by the factor shown next to their name on label.

Table 2.2. Summary of identified and suggested phases from powder XRD analysis. Mineral name, chemical formula and chemical state of Mn is presented.

Substrate	Mn-only influent solution				Mn-Al influent solution			
	Mineral Name	Chemical Formula	Chemical State Mn	Crystal Structure	Mineral Name	Chemical Formula	Chemical State Mn, Al	Crystal Structure
Alumina spheres	Suggested phases: δ Birnessite (δ – MnO_2) (see [31]) Feitknechtite: (diffraction data used from the isotypic Pyrochroite (PDF Card # 01-073-1133) (see[52]))	$Na_{0.07}K_{0.05}MnO_2 \cdot 0.44H_2O$ MnO(OH)	Mn^{3+}, Mn^{4+} Mn^{3+}	System: Monoclinic Space Group: $C12/m1$ (12) Lattice parameters: a = 4.966 b = 2.825 c = 7.35 α = 90° β = 95.7° γ = 90° System: Hexagonal Space Group: $P\bar{3}m1$ (164) Lattice parameters: a = 3.322 b = 3.322 c = 4.734 α = 90° β = 90° γ = 120°	Identified phases: Bayerite (PDF Card # 00-901-0964 (see[53]) Suggested phases: δ Birnessite (δ – MnO_2) (see [31]) Feitknechtite (Isotypic Pyrochroite (PDF Card # 01-073-1133) (see[52]))	$Al(OH)_3$ $Na_{0.07}K_{0.05}MnO_2 \cdot 0.44H_2O$ MnO(OH)	Al^{3+} Mn^{3+}, Mn^{4+} Mn^{3+}	System: Monoclinic Space Group: $P12_1/n1$ (14) Lattice parameters: a = 5.096 b = 8.729 c = 9.489 α = 90° β = 90.26° γ = 90° As already presented As already presented
Silica Sand	Identified phases: Hexagonal Birnessite (see [31]) Unknown crystalline phase d	$MnO_2 \cdot 0.56H_2O$	Mn^{3+}, Mn^{4+}	System: Monoclinic Space Group: $C12/m1$ (12) Lattice parameters: a = 4.935 b = 2.841 c = 7.23 α = 90° β = 91.17° γ = 90	Suggested phases: δ Birnessite (δ – MnO_2) (see [31]) Feitknechtite (Isotypic Pyrochroite (PDF Card # 01-073-1133) (see[52]))	$Na_{0.07}K_{0.05}MnO_2 \cdot 0.44H_2O$ MnO(OH)	Mn^{3+}, Mn^{4+} Mn^{3+}	As already presented As already presented

Glass Beads	Identified phases: Hexagonal Birnessite (see [31])	$MnO_2 \cdot 0.56H_2O$	Mn^{3+}, Mn^{4+}	As already presented	Suggested phases: δ Birnessite (δ – MnO_2) (see [31]) Feitknechtite (Isotypic Pyrochroite (PDF Card # 01-073-1133) (see[52]))	$Na_{0.07}K_{0.05}MnO_2 \cdot 0.44H_2O$ MnO(OH)	Mn^{3+}, Mn^{4+} Mn^{3+}	As already presented As already presented

In figures 2.6, 2.8, 2.9 and 2.10, spectra from coatings formed in the presence of Al showed major broad peaks at an interplanar spacing of around 4.72 Å, 2.45 Å and 1.42 Å. The 4.72 Å peak corresponded with the basal plane spacing in a pyrochroite-like layered phase. A layered structure for this phase is proposed, since only a few prominent diffraction peaks associated mainly with one plane (basal) were observed. Several other peaks expected from planes at an angle to the layer plane (basal) were missing. On the other hand, the 2.45 Å and 1.42 Å broad peaks coincided with several spectral features from regions of the diffraction pattern of a turbostratically disordered birnessite (probably δ-MnO_2). Nevertheless, this disordered phase was not detectable by the experimental setup used in this study. These data suggested that the presence of Al promoted the formation of a mixture of poorly crystalline phases: a pyrochroite-like layered phase and a disordered unidentified phase (probably δ-MnO_2) regardless of the type of filter media used. In addition, the hexagonal-birnessite on silica sand media showed slightly sharper peaks (figure 2.7) compared to the ones formed on glass media (figure 2.5). This can be attributed to an increase in the crystallite size and the crystallinity of the coating. The Scherrer equation –considering crystals of the same regular shape with the same size (smaller than 100 nm for valid predictions)-[54, 55] was applied to XRD data (figures 2.5 and 2.7) in order to estimate the crystallite size from the (001) reflection of hexagonal birnessite at d-spacing of 7.2 Å. A spherical crystal shape, confirmed by TEM observations (figure 2.11), was used for calculating the Scherrer constant. The Full Width at Half Maximum (FWHM) approximation was applied. It uses the width of the diffraction peak, in radians, at a height half-way between background and the peak maximum. The diameter of a spherical crystallite was calculated as follows:

$$Dp = \frac{0.9\lambda}{\text{peak FWHM}*\cos(\text{peak position}/2)} \quad (2)$$

For hexagonal-birnessite on glass, crystallite size was estimated as 7 nm; meanwhile, the crystallite size for hexagonal birnessite on sand is 8 nm. These calculated values are consistent with the observed crystallites in the TEM images of figure 2.11.

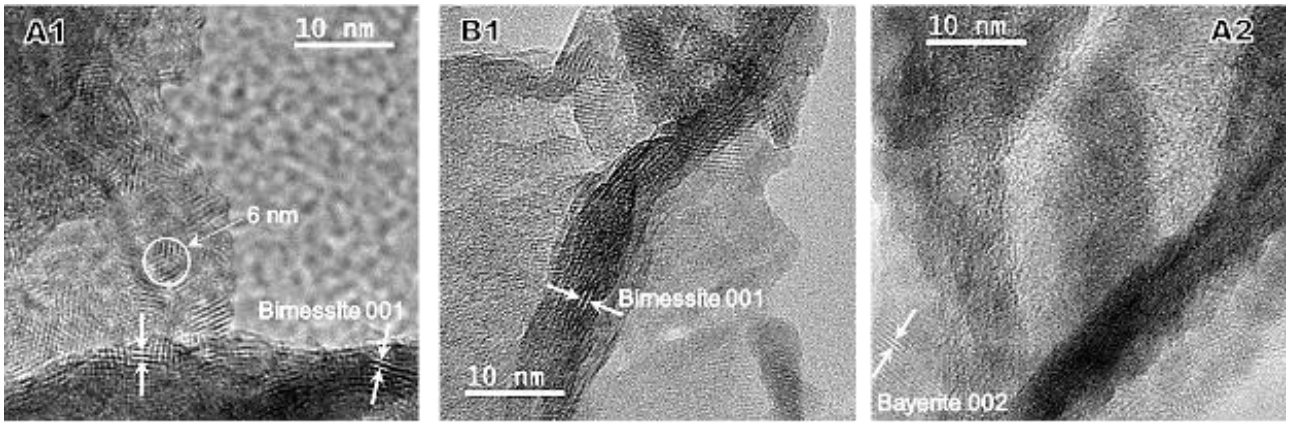

Figure 2.11. TEM micrographs of coating: Mn-only on glass (A1), Mn-only on sand (B1), and Mn-Al on glass (A2) showing birnessite (001) (d = 7.2 Å) and bayerite (002) (d = 4.7 Å) lattice fringes. In A1, pseudo-spherical nanoparticles can be observed with a size of approximately 6 nm in a botryoidal configuration.

2.2.3. Microstructure

I. General appearances

Figure 2.12 presents the appearance of coated alumina media inside a column at the end of the experiments (sixth day). Images clearly show that filter media in the same column are unevenly coated with MnO_x(s). This condition is especially highlighted in the Mn–only column, where neighbor alumina spheres depict a radical color difference despite the same local condition. This strongly suggests that media characteristics are playing an important role in the coating formation process.

Optical micrographs showed differences in the surface morphology and topography for each media type (see figure 2.13). Fresh glass beads were a combination of smooth surface with little

concave defects appearing as pits or craters. Alumina spheres and silica sand showed features with topography, especially height differences and heterogeneous asperities distribution. Silica sand presented a characteristic intricate morphology. Due to the spherical shape and relatively larger size of glass and alumina media (considering similar filter bed packing condition), voids with a minimum diameter of 46 μm and 50 μm respectively are observed. These voids are approximately 4 times bigger than the ones in silica sand media (with a minimum diameter of 13 μm), if spherical sand granules were assumed to have no intricate morphology that could affect the bed porosity. When filter media have irregular/intricate shape, elongated areas of the granules may extend further into the voids, reducing their size. The opposite will also hold true. To the knowledge of the author, alumina spheres were shaped from sintered alumina particles. Thus, both alumina spheres and silica sands were considered as a micrometer size poly-grain aggregates.

Figure 2.12. Appearance of two columns with alumina spheres used as media at the end of experiments (sixth day). Media was exposed to Mn^{2+} in the absence and presence of Al with free chlorine as oxidant across the filter.

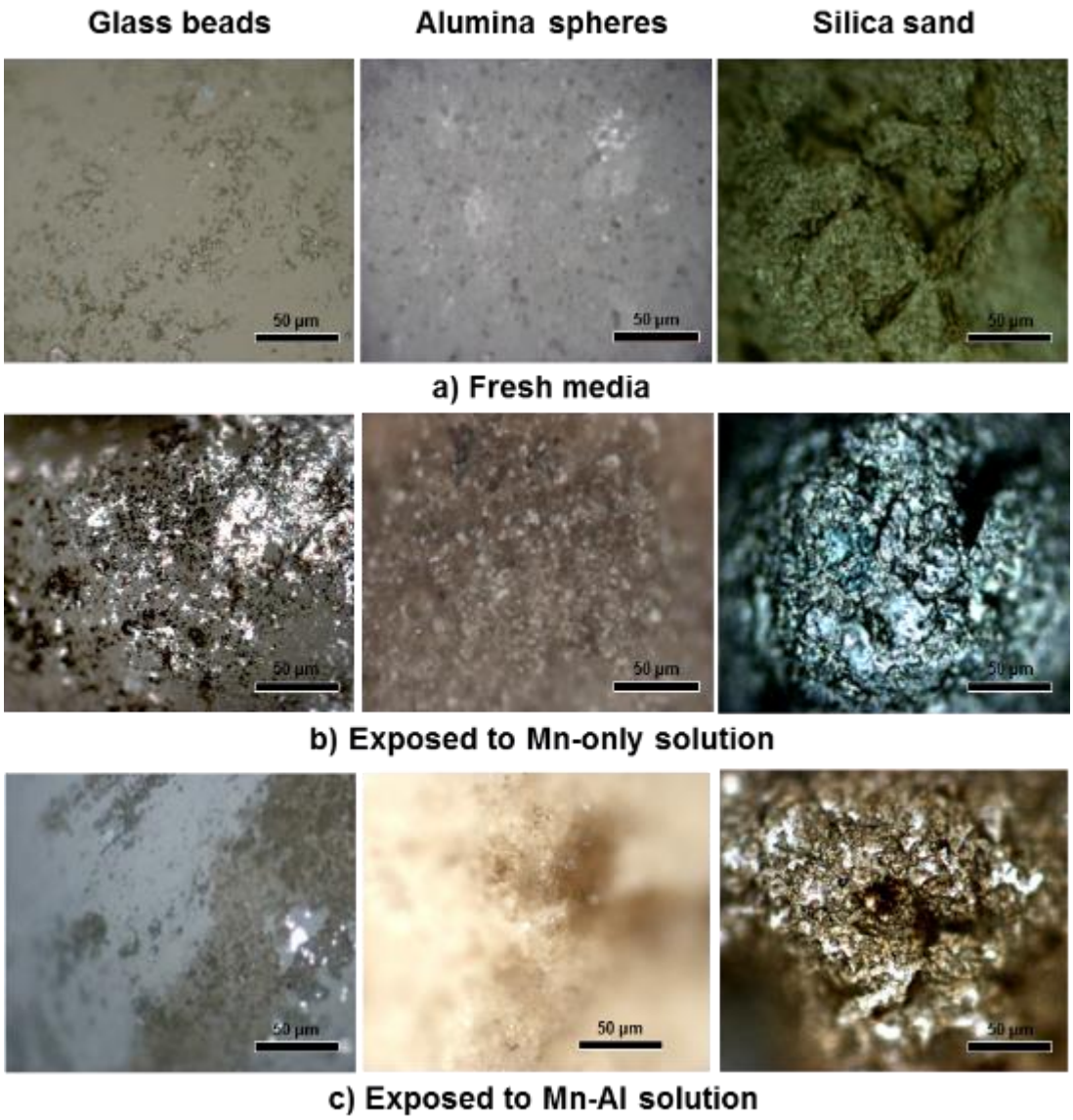

Figure 2.13. Optical micrographs of fresh filter media (a), MnO_x(s)-coated media exposed to Mn-only solution(b), and MnO_x(s)-coated media exposed to Mn-Al solution(c) in the presence of chlorine as oxidant (scale bar in all images is 50 micrometers).

Initially developed Mn-only and Mn–Al MnO_x(s) coatings were observed on concave areas of glass media, as well as on sides (valleys) of protrusions of alumina media (Figures 2.16, 2.18, 2.20 and 4.12 in chapter 4). On silica sand media, a thicker coating was developed with coverage presumably initiating on valleys or concave areas. When Al was added, coatings on all three media were mainly formed by deposited aggregates of material, which resembled flocs that could be easily re-suspended in water by even a gentle movement of the media while retrieving it.

Meanwhile, all the Mn-only coatings on media were not easily re-suspend in water (needed to be vigorously shaken), thus they seemed to be relatively less abundant.

II. The morphological changes of coating on different media

SEM Micrographs (figures 2.14, 2.15, 2.16) show the morphology and location of coating on each filter media after a six-day column operation. In the Mn-only coating on glass and silica sand media, the morphology resembled a honeycomb-like structure as described by Junta and Hochella (1994)[38], displaying a uniform coverage of media surface. Meanwhile, the Mn-Al coating on glass and silica sand media had the same honeycomb-like structure, but showed a non-uniform ("patchy") coverage of media surface. Multiple patches of coating were interconnected with each other. On alumina media, there was a minimal apparent difference in the coating morphology or distribution. In Mn-only coating, localized coatings started to connect with each other and formed a uniform distribution of coating (resembling a film) more rapidly than Mn-Al coating. The apparent coating thicknesses were correlated with the rougher surface areas of filter media, thus an inhomogeneous surface coverage occurred. The thickness of coatings corresponded directly to the darker areas observed in optical images in figure 2.12.

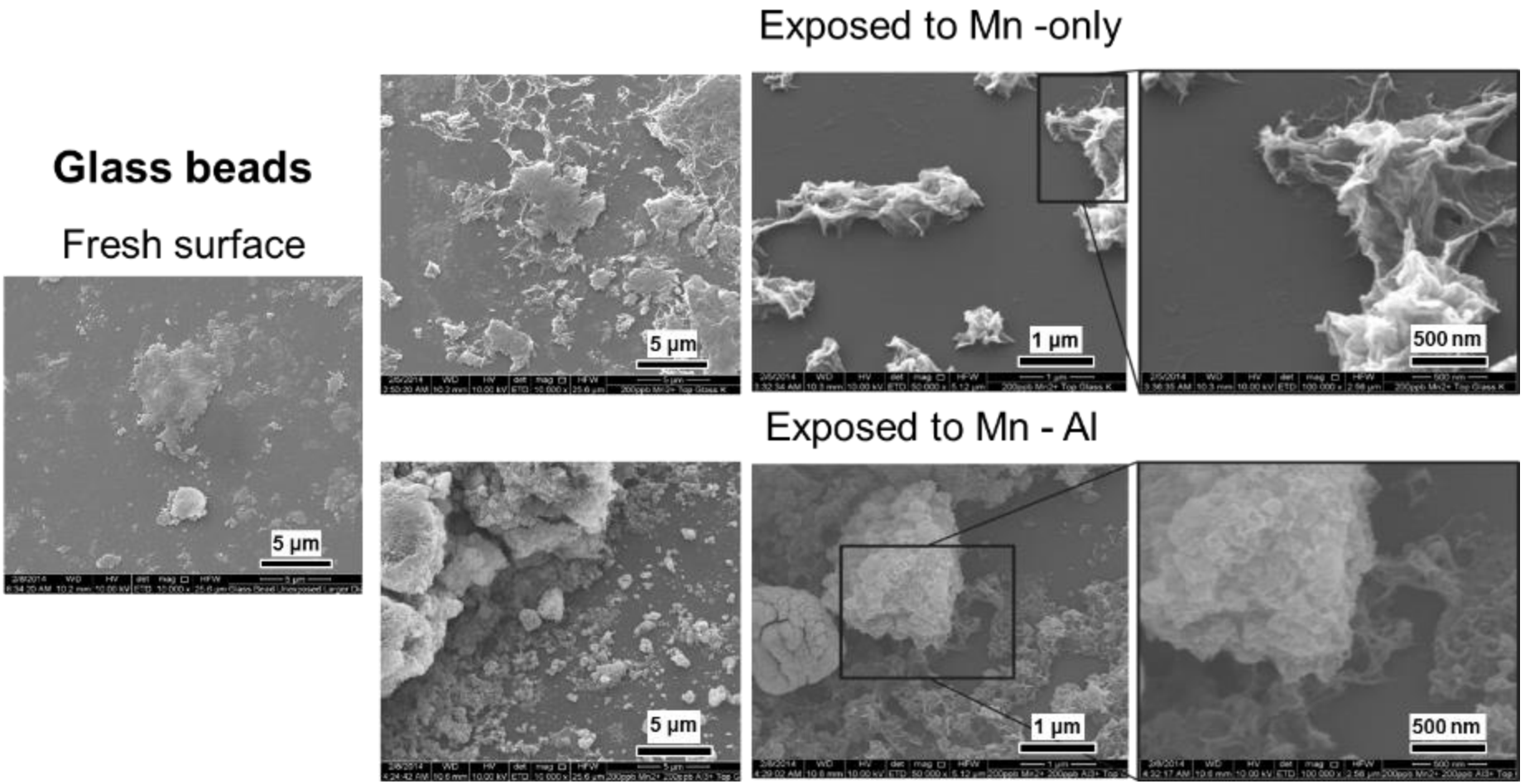

Figure 2.14. SEM micrographs of glass filter media showing fresh media surface and location of manganese-containing deposits (lighter grey with honeycomb-like morphology). When coating is developing on filter media, uncoated areas of glass surface are observed in dark grey. These media were exposed to Mn-only and Mn-Al solutions for six days.

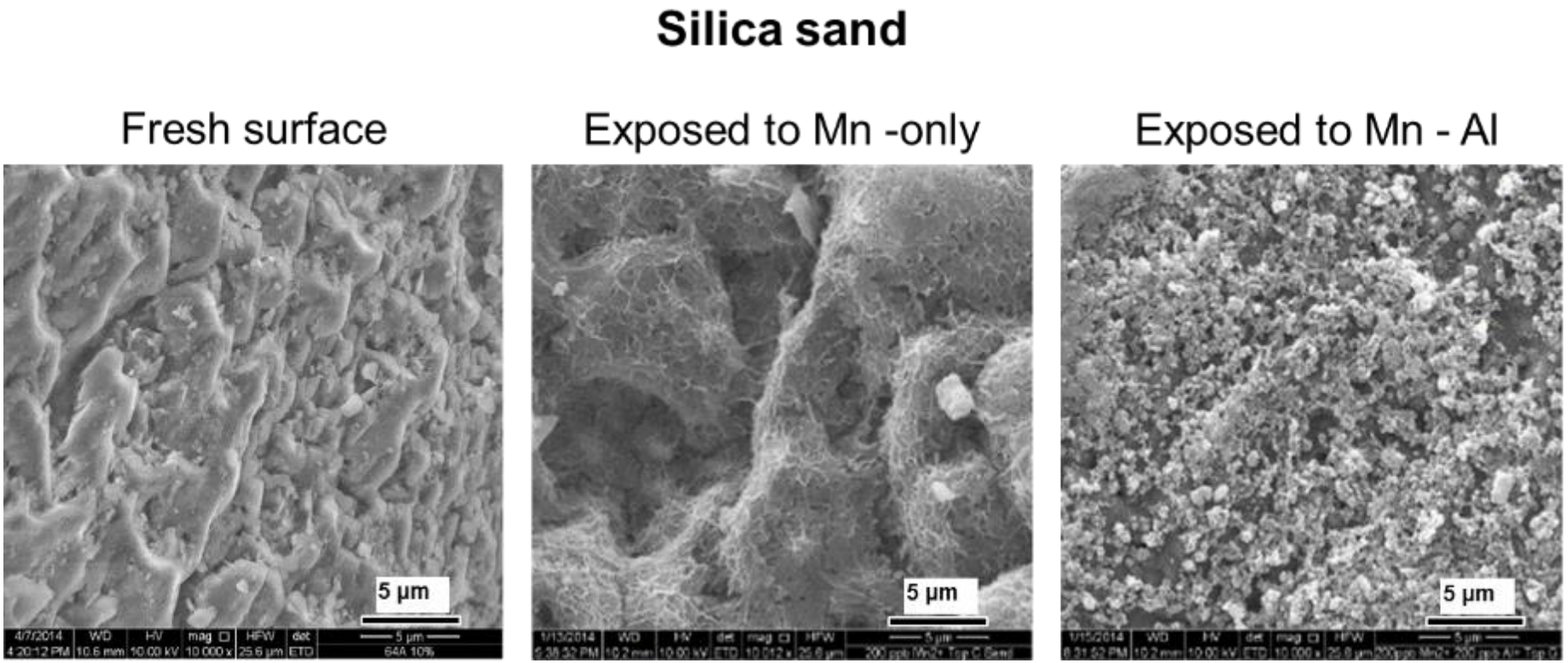

Figure 2.15. SEM micrographs of sand filter media showing fresh media surface and manganese-containing deposits (lighter grey with honeycomb-like morphology) covering almost all sand media surface (dark grey). These media were exposed to Mn-only and Mn-Al solutions for six days.

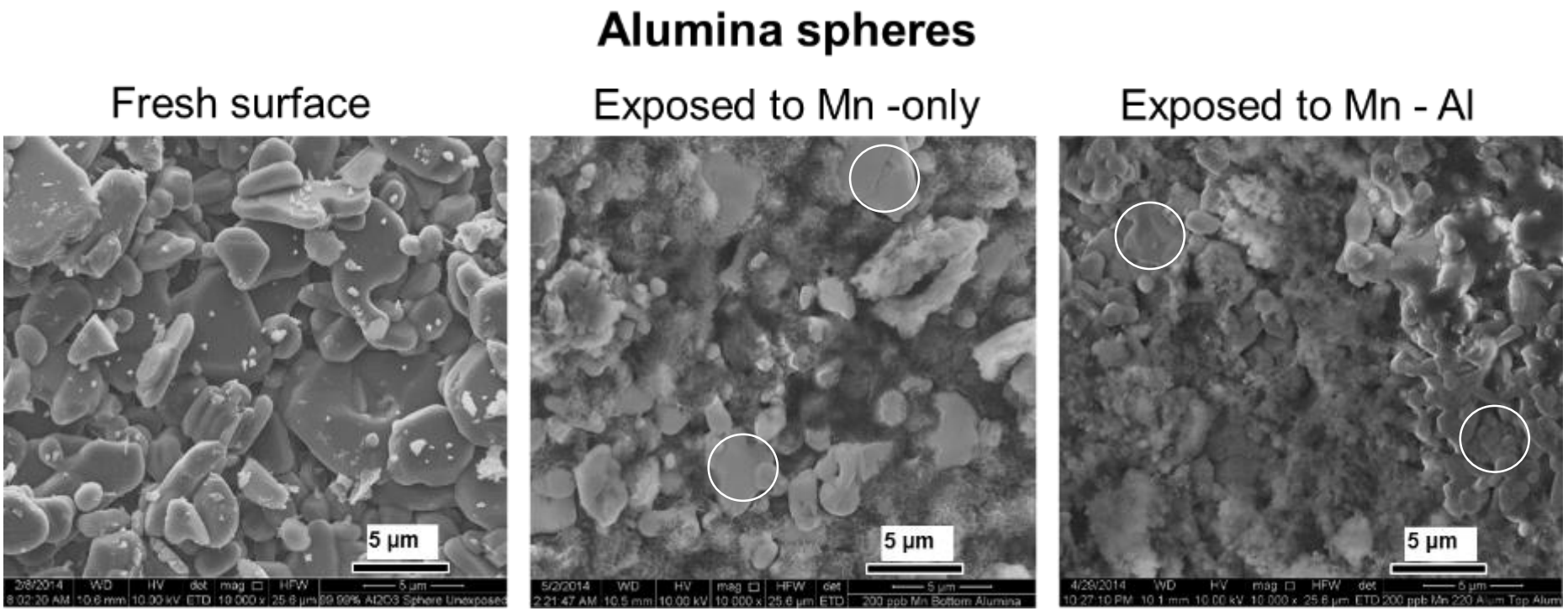

Figure 2.16. SEM micrographs of alumina filter media showing fresh media surface and location of manganese-containing deposits (dark grey with honeycomb-like morphology). When coating is developing on filter media, uncoated areas of alumina surface are observed in lighter grey (circles). These media were exposed to Mn-only and Mn-Al solutions for six days.

III. The effect of sample preparation process (dehydration)

SEM sample preparation usually includes a drying process and dehydration, which may change the coating morphology. Hence, changes in the coating morphology during SEM analysis was further examined under three different humidity levels (100%, 50% and 15%) in the SEM chamber. For this analysis, samples from columns were carefully preserved in distilled water until inserted in the SEM chamber, and rapidly mounted on a SEM sample holder to avoid dehydration prior to analysis. No noticeable change was observed in the Mn-only coatings. Meanwhile, Mn-Al coatings presented small changes in morphology of thin areas when illuminated by the electron beam. Several small areas of the Mn-Al coating disappeared due to water evaporation leaving behind burst marks; whereas, the majority of coating morphology was preserved intact (see figure 2.17).

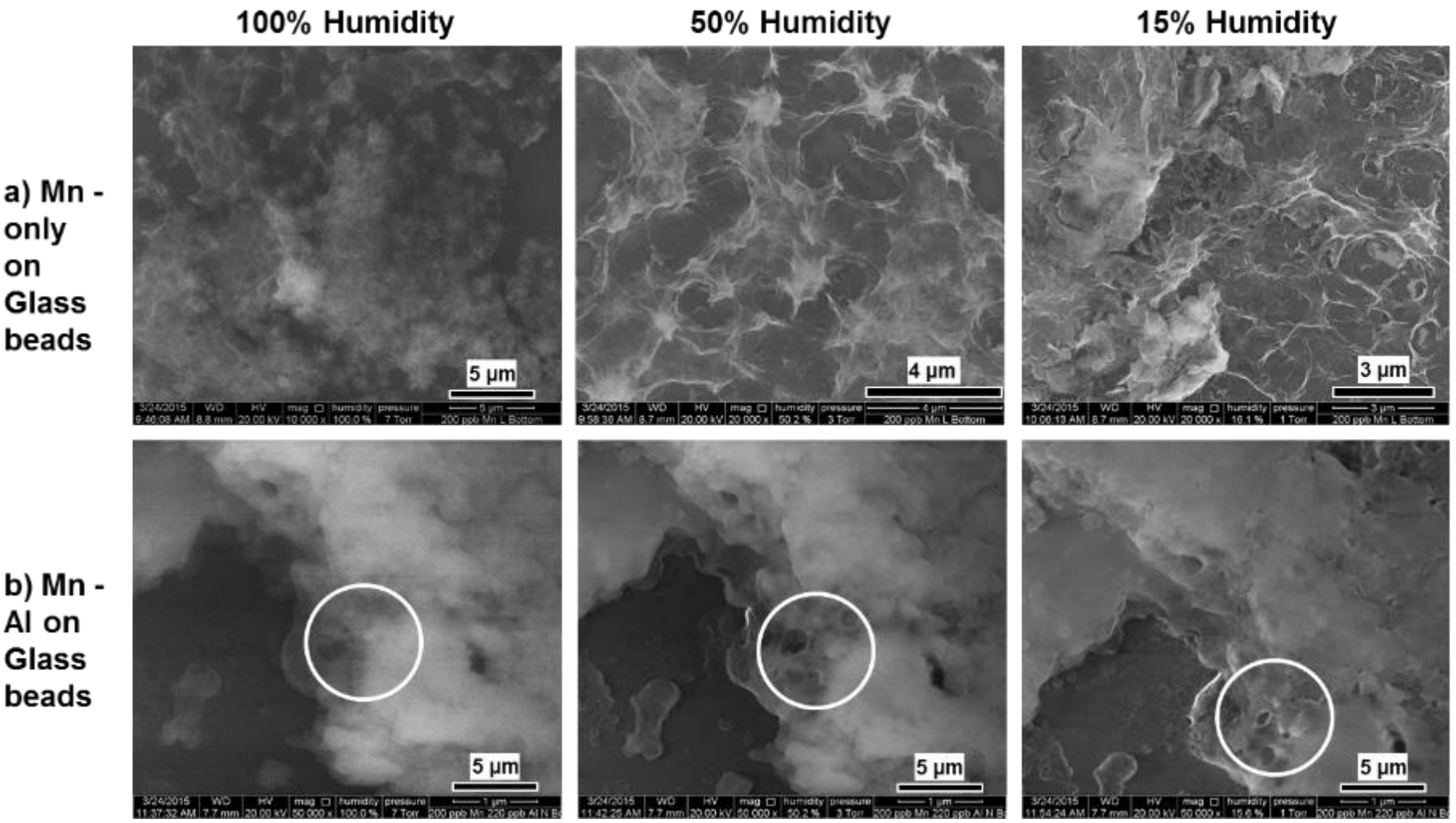

Figure 2.17. SEM micrographs of glass filter media showing manganese-containing deposits formed when exposed to Mn-only and Mn-Al solutions. Circles mark the same monitored area for showing changes in coating morphology when drying.

IV. Al effects on the coating growth mode

When comparing the morphology of a small localized section of the Mn-only and Mn-Al coatings, they were very similar to each other as shown in figure 2.14. The Mn-only coating growth was observed to occur preferentially at the interface of a previously precipitated MnO_x(s), the media surface, and the solution. The coating spread first to the lateral direction (parallel to the media surface) rather than increasing its thickness. Also, images in figures 2.14, 2.15, and 2.16 show attachment/connection of neighboring Mn-Al coatings that aggregated to each other to develop networks/films as time passed. SEM-EDS point analyses on different areas of the coating confirmed the presence of Mn, O, and Al (where applicable) supporting the previous findings (figure 2.18).

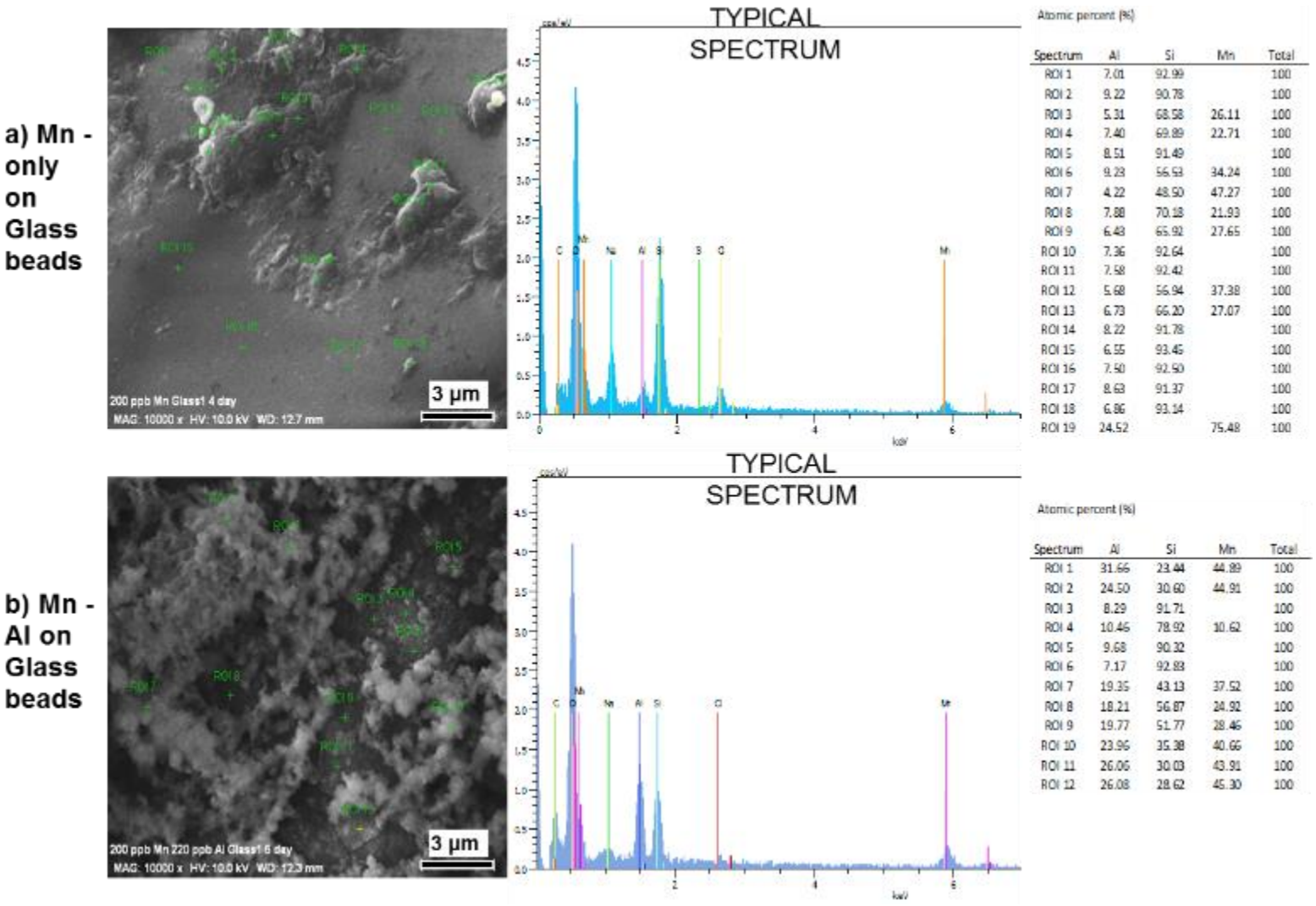

Figure 2.18. SEM-EDS point analysis of coatings on glass media showing a typical spectrum of one region of interest (ROI) and calculated values of elemental composition of all ROIs shown in the micrographs. Background levels of Al are assumed to originate from the SEM sample holder used.

In figure 2.19, the evolution of coating was studied using glass media under the presence and the absence of Al. In the Mn-only coating, a two-dimensional film growth process was observed. The media surface coverage was increased predominantly during the first 24 hours, and then the coating was observed to become thicker. Darker areas appeared progressively in figures 2.19 (b) – (d). The Mn-only coating growth was correlated with these darker areas. After day 3, the honeycomb-like structure was observed in the Mn-only coating with outward extended features. Meanwhile, in the Mn-Al coating, a three-dimensional island growth behavior was observed. During the first 24 hours, the Mn-Al coating presented only a few isolated islands. Darker areas (same as those in the Mn-only coating) were formed at the end of this period. After day 3, larger aggregates/islands were observed in the Mn-Al coating with greater thickness compared to the Mn-only coating. Aggregates were also observed to deposit near or on top of darker areas. It is worth noting that the sample surface was occasionally charged up during imaging due to the extremely poor electron conductivity of media, especially the glass media. This made it difficult to adjust the image contrast and introduced localized image distortions like the intense bright spots in figures. 2.19(b), (i), and (j).

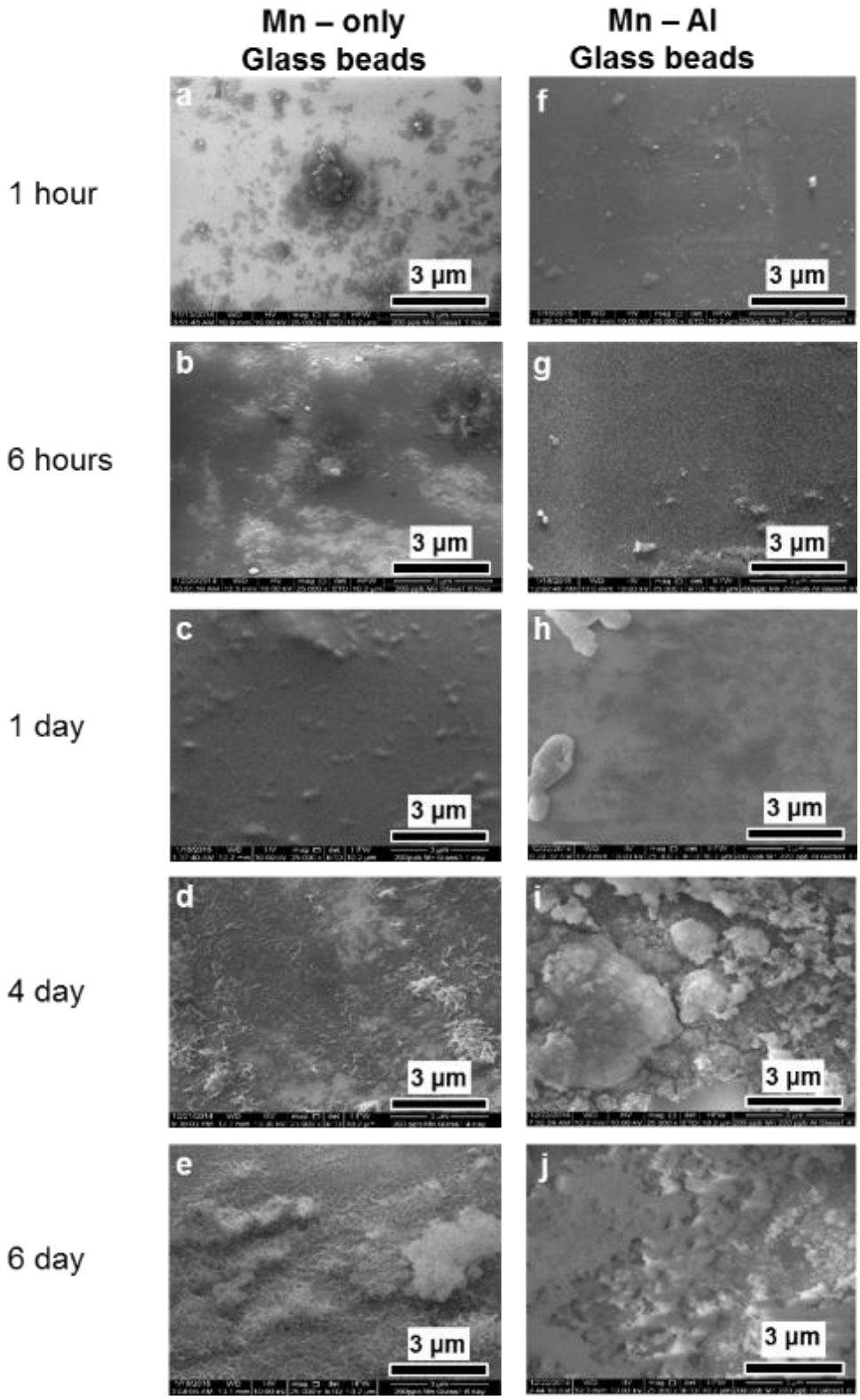

Figure 2.19. Coating evolution with time observed in bench-scale experiments using glass media in the absence and the presence of Al.

In figure 2.20, a difference in coating growth was noticed on alumina media subjected to Mn-only and Mn-Al solutions. On media subjected to the Mn-only solution, coatings continuously covered a large area of the media surface. Meanwhile, Mn-Al coating showed a few coating aggregates deposited on the media surface with a film/network growth morphology. This suggested that the addition of Al promoted suspended solids formation, namely, amorphous Al oxy(hydr)oxides (bayerite). Then, bayerite would increase the effective surface area where coating formation is occurring. Additionally, a slow film/network growth of coating was observed which could stimulate more δ-birnessite formation.

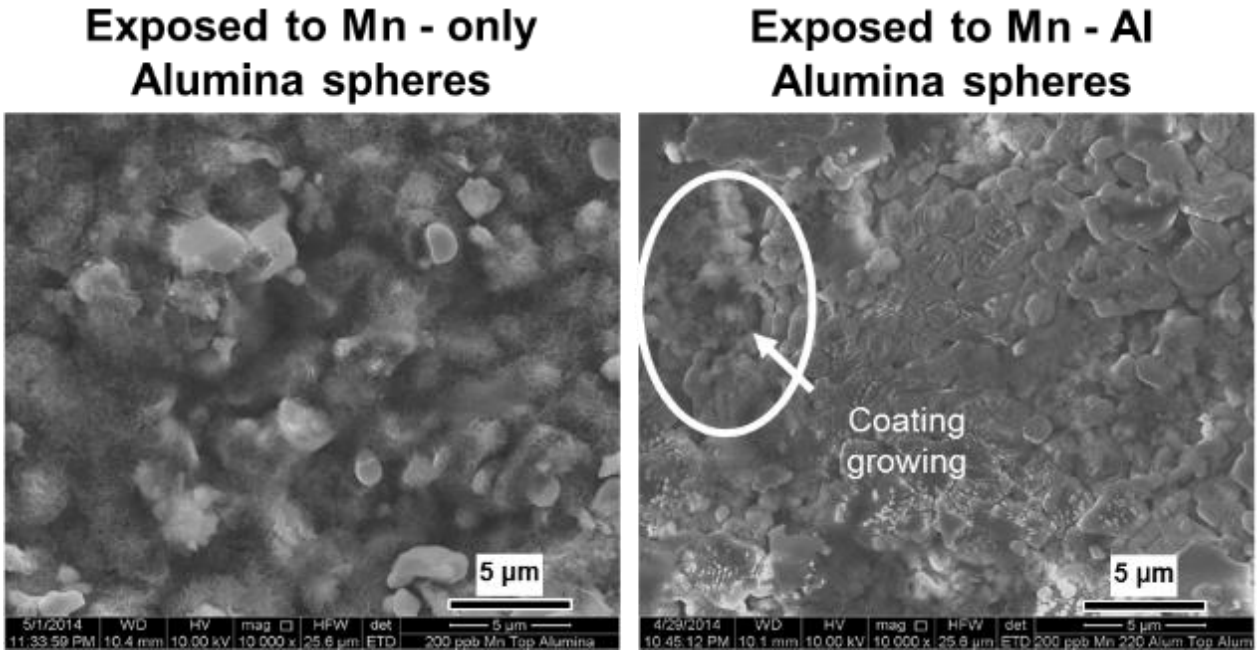

Figure 2.20. MnO_x(s) coating growth on top of alumina media exposed to Mn-only and Mn-Al solutions.

2.3. Discussion

2.3.1. Factors improving the Mn removal efficiency

Three factors for improving the soluble manganese removal efficiency were identified: (1) surface roughness, (2) Al addition, and (3) media morphology and convective diffusion. Their relative contributions to manganese removal are shown on the right side of Figure 2.2.

Rougher surfaces (silica sand and alumina) capture more soluble manganese than smooth surfaces (glass). This can be explained by an increase in the specific surface area in rougher surfaces, which impacts positively in the process of soluble Mn^{2+} sorption, oxidation and particle attachment. Simultaneously, rougher surfaces are believed to provide a shielding effect (through asperities) from shear flow to attached particles on the surface of media. In addition, rougher surfaces are thought to change the local conditions that modify colloid-filter media interactions.

It has been demonstrated that Al species in water neutralize surface charge, destabilize and coat colloidal particles at circumneutral pH.[17] Consequently, colloidal particles start to aggregate and form larger particles. Simultaneously, Al species specifically forms oxy(hydr)oxides that clump together forming flocs, providing extra surface area for Mn^{2+} sorption, oxidation and particle attachment. Al addition operates in combination with the media morphology and convective diffusion.

As noted by Shen et al. (2012), the filter media morphology dictates favorable sites for sorption and precipitation. Also, the granule morphology impacts in the shape and size of bed porosity that affect the fluid flow/particle trajectory, as well as the interactions colloid – filter media. These morphological effects increase the filter efficiency by reducing porosity and increasing filter bed surface area with time (filter ripening). Further explanations of all these factors are given in the following sections.

On the other hand, each curve in fig. 2.21 shows two stages in the removal process. The first part has a negative slope that can be designated as the formation rate of the first $MnO_x(s)$ coating on fresh media mainly by precipitation. Then, each curve reaches a plateau (the second stage) suggesting that a steady state process is taking place and which can be considered as a coating growth stage. This growth stage can be proposed as a combination of a surface-catalyzed oxidation of soluble Mn and precipitation of $MnO_x(s)$ particles. Since other authors[4, 6, 8, 10] have shown that the active catalytic reaction in this system takes place preferentially, then this reaction is understood to be the limiting step that controls the soluble manganese removal rate in this second stage.

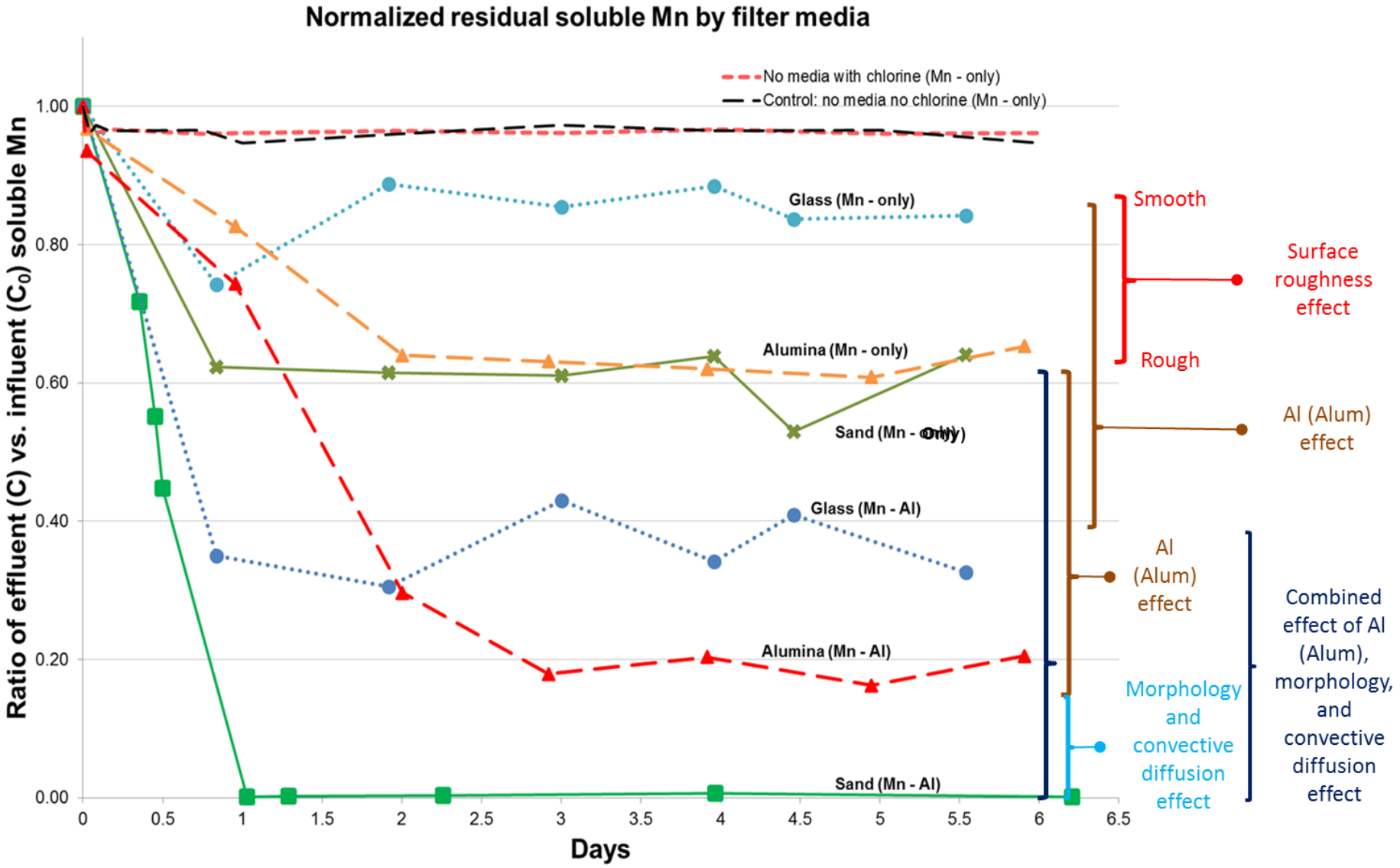

Figure 2.21. Graphical representation of the impact of different suggested factors on the soluble Mn^{2+} removal efficiency by different filter media in a porous filter having free chlorine as oxidant across the bed in the absence and presence of Al. Glass, alumina, and silica media removed correspondingly a greater amount of this soluble contaminant from solution.

2.3.2. Elemental composition and structure of media

Phase identification results indicate that (Table 2.2, Figures 2.5 to 2.10) same phases were formed in coating irrespective of the media crystal structure (crystalline or amorphous), indicating that the crystal structure of media did not play a role in the MnO_x(s) coating formation. This condition was also supported by SEM results (figure 2.20) showing that faceted areas of alumina did not change the coating formation process in any way. In contrast, the elemental chemistry of media was identified as an important factor in the initial formation and development of these coatings. Depending on the media chemistry, different phases can be formed or promoted as observed in alumina media (Table 2.2, Figures 2.9 and 2.10). When alumina media was exposed to Mn-only solution, a mixture of poorly crystalline phases was formed (suggested to be a pyrochroite-like layered phase or another oxidized Mn phase, and a turbostratically disordered birnessite) which were observed on other media -in this study- only when these were exposed to Mn-Al solutions. It was unclear and beyond the scope of this study, however, to investigate how the alumina media stimulates the formation of these phases.

2.3.3. Media morphology, surface roughness, and convective diffusion

The overall media morphology determines the type and size of pores in the filter bed. The comparison between these pores with the size of particles of coating observed in TEM images (figure 2.11) provided a consistent and strong support for the convective diffusion as a primary mechanism taking place to capture particles. Since particles are really small (less than 10 nm), the effective forces and interactions impacting their behavior are in the scale/order of Brownian motion. Consequently, the convective diffusion is the primary mechanism at work here. The pores in filter bed were measured as spheres of a minimum diameter of 46, 50 and 13 microns in glass, alumina, and silica sand, respectively. Therefore, there is approximately three orders of magnitude of difference between the pores and colloidal particles sizes, which would allow the particles to move in a large open space. Although diffusion is the

primary transport process driving particle attachment for all of the studied cases, the attachment mechanism is affected mainly by particle-media interactions, which depend on media's characteristics; i.e., mainly the surface roughness and elemental chemistry. Consequently, the three media would interact with the particles differently. That is the main reason of using an extended DLVO theory in chapter 4 for assessing preferential locations of particle attachment. In addition, when Al was added to the feed solution (see figure 3.1), the particle capture process was enhanced. The Al effect is discussed in detail in section 2.3.5.

A proposed birnessite formation process is started by the precipitation of poorly crystalline nanoparticles, followed by autocatalytic oxidation of soluble manganese on their surface in combination with co-precipitation. These nanoparticles or nanoparticle aggregates oxidize soluble manganese forming more birnessite, as well as other phases, such as hausmannite and/or manganite (depending on the pH)[56, 57]. In this case, Mn^{2+} sorption and oxidation occur preferentially on birnessite-dominated coating surface due to its high catalytic activity. Since the preferred location of birnessite formation is rough surface areas of filter media (observed in figures 2.12 through 2.20), the birnessite formation rate would increase by having media with rough surfaces. Moreover, the Mn removal capability could be enhanced with increasing birnessite formation rate.

Incidentally, silica sand media have a high specific surface area arising from the intricate surface morphology and topography, and it showed to have the highest manganese (nanosize MnO_x(s) in conjunction with soluble Mn) removal capability. The observed greater crystallinity of the coating and potential hausmannite formation favorably taking place on the silica sand surface coating would be explained by the high autocatalytic activity of hexagonal-birnessite. Greater crystallinity indicates that a larger quantity of hexagonal-birnessite formed. Although δ-birnessite has a higher reactivity than hexagonal-birnessite, hexagonal-birnessite has a higher activity than the bare surface in terms of adsorption and oxidation. The potential hausmannite formation also stimulates the soluble manganese removal capability because more soluble manganese would be oxidized, and more nanoparticles could

be formed. These nanoparticles will be then attached to the surface, improving the Mn removal rate. Again, more birnessite present, more soluble manganese will be removed.

Furthermore, the uneven coating coverage area was shown to be correlated with the difference in surface roughness, and demonstrated by coating thickness difference observed especially in figure 2.12. Since birnessite is hypothesized to be formed initially by precipitation of poorly crystalline nanoparticles, followed by an autocatalytic oxidation of soluble manganese on their surface in combination with co-precipitation, and further soluble Mn oxidation into hausmannite and/or manganite [10, 13, 15, 30], nanoparticles will be usually present and could preferentially be located in rougher surface areas such as concave regions. When surface roughness increases, coating thickness; i.e., the amount of coating, increases as well due to a larger fraction of concave regions on media surface.

2.3.4. Coating evolution

After the initial $MnO_x(s)$ deposits were formed, coatings continuously grew by a combination of $MnO_x(s)$ nanoparticle precipitation, and sorption and oxidation of Mn^{2+} as reported in previous work [15]. This is also identified in the time-resolved observation of the coating growth at the interface of a previously precipitated $MnO_x(s)$, the media surface and the solution. At certain time intervals, new connections between previously formed coating precipitates are established for developing networks/films. This process can be observed in figure 2.16, where initial coating formation areas got larger and increased in number as time elapses.

Suppose some of the nanoparticles were formed in solution and then attached on media surface, the oxidation of soluble manganese was partly occurring in water. Further, the experimental results show that multiple manganese oxide phases are found intermixed with no specific preferential location for each phase. Thus, each phase would form independently but nearly concurrently, rather than sequentially, i.e., co-precipitation or reactions occurred at the same time.

This scenario is consistent with several previous proposed Mn oxidation reactions [58, 59], and can be described by a set of half equations. Cornell and Giovanoli (1988)[60] showed that the reaction of hausmannite transforming into birnessite is relatively slow (4 - 5% transformation in 1 day and complete transformation in weeks to months in alkaline conditions at 70°C). Lefkowitz et al. (2013)[56] and Elzinga, E.J. (2011)[57] demonstrated that the surface-catalyzed oxidation of aqueous Mn (II) in oxic conditions is promoted by the presence of birnessite, rapidly forming the metastable phase feitknechtite (β-MnOOH) and releasing protons (H^+). Then, feitknechtite is transformed to manganite (pH 7.0 to 8.0) or hausmannite (pH 8.0 to 8.5) (transformation completed in 8 – 10 days, with initial formation of hausmannite at pH of 8.5 in just 30 minutes). The presence of a small amount of hausmannite in the Mn-only coating on glass and sand media (and feitknechtite on sand media) confirmed by nanodiffraction in TEM (further details in chapter 3) may support that this transition process happened, i.e., birnessite is forming feitknechtite which in turn is transforming to hausmannnite. If that is the situation, this transformation pathway suggests a localized pH increase near the surface of birnessite and the potential increasing in the Mn (II) removal capacity of coatings. In summary, the proposed growth model would be:

Poorly crystallized nanoparticles → birnessite → form and precipitate more birnessite and at the same time form feitknechtite → feitknechtite transform to hausmannite (Mn-only samples) or to a manganite-like material (these could be the amorphous material formed when Al is present, such as in Mn-Al coating on all media and Mn-only coating on alumina media).

The reactions' half equations are:

$Mn^{2+} + OCl^- \rightarrow$ poorly crystallized nanoparticles that organized forming Birnessite (s)

Mn^{2+} + Birnessite (s) + $2H_2O \rightarrow 2MnOOH$ (s) (feitknechtite) + $2H^+$

$2Mn^{2+} + OCl^- + 3H_2O \rightarrow 2MnOOH$ (s) (feitknechtite) + $4H^+$ (on the surface of birnessite)

Mn^{2+} + 2MnOOH (s) (feitknechtite) → Mn_3O_4 (s) + $2H^+$ (pH 8.0 to 8.5)

2MnOOH (s) (feitknechtite) → 2MnOOH (s) (manganite) (pH 7.0 - 8.0)

2.3.5. Role of Al addition

Aluminum specifically destabilizes MnO_x(s) colloids and forms oxy(hydr)oxides that clump together forming flocs that could provide extra surface area for Mn^{2+} sorption and oxidation. According to Amirtharajah (1988)[17], Al $(OH)_3$ (bayerite) is the principal form of solid species at the pH of this study (pH=7.3). This phase was confirmed by TEM (in chapter 3). Bayerite flocs destabilize MnO_x(s) colloids that ultimately attached to them, and increase the removal efficiency of soluble manganese [17]. In figure 3.1, it can be observed that the filter efficiency increases two to three times when Al is present. Specifically, there is an increase of three times the amount of Mn^{2+} removed in glass, two and a half times in sand, and two times in alumina. The governing mechanisms of increasing filter efficiency by Al addition were the reduction of bed porosity by flocs sedimenting on the surface of filter media and the increment of bed surface area with time; although it adversely increased the head loss as well.

When comparing two homologous surfaces covered by Mn-only and Mn-Al coating, it is observed that the Mn-Al coating is generally thicker (figures 2.13 and 2.17). For smooth surfaces like glass media, the Mn-Al coating is twice thicker than the Mn-only coating. For rough surfaces, there is a greater preference of birnessite formation in localized favorable sites (concave areas), which increases 20% or more the thickness of the Mn-only coating relative to the Mn-Al coating (see page 91 in Chapter 4 for more detail). This is explained by a larger amount of birnessite attached to the surface of filter media, which can further catalyze the formation of surface coating. In addition, birnessite is thought to be attached to the loose Al oxy(hydr)oxides flocs as well as filter media surface, thus a smaller fraction of birnessite is formed on the media surface subjected to the Mn-Al solution (figure 2.13). Nonetheless, the total amount of birnessite was increased, leading to more soluble manganese removal. Al addition also impacts/reduces the thickness of coating because the amorphous manganite-like and probable hausmannite phase could be attached to bayerite flocs rather than the surface of filter media.

It is worth noting that bayerite can also be encapsulated by other phases such as birnessite growing on top of it. Furthermore, as observed in the presented results in Chapter 3, the presence of Al in water promotes the formation of poorly crystalline turbostratically disordered birnessite (δ-MnO_2) which could hinder the ordering of the material and stimulate formation of aggregates of birnessite regardless the type of filter media used.

CHAPTER 3. Nanoscale study of colloidal manganese oxide particles and films formed during water filtration and their implications for drinking water treatment.

3.1 Summary

In Chapter 2, the morphological features and constituent phases of the surface coatings on three different filter media were investigated by SEM and XRD. Powder XRD results from solid surface coating materials indicate that coatings are a mixture of coexisting poorly crystallized manganese oxides and oxy(hydr)oxides, and aluminum oxy(hydr)oxides. SEM results demonstrate that the surface coatings consist of nanoparticles ranging few to few 10 nm in size and flaky films with thicknesses in the same order of magnitude. In this Chapter, Transmission Electron Microscopy (TEM) characterization down to nanometer scale was conducted to further investigate the morphology and structure of coating material. The results confirmed that nanoparticles of a poorly ordered MnO_x(s) phase (birnessite) were deposited on filter media along with other amorphous oxy-hydroxide phases containing Al and Mn. Small amounts of hausmannite and of an amorphous manganite-like phase were also found. The presence of a small volume faction of these two minor phases suggests that they are either precursor phase or a byproduct of a surface-catalyzed oxidation of Mn (II) by birnessite. The presence of an oxidant across filter bed (free chlorine) also promotes the accelerated oxidation processes observed. Finally, a phase transformation process is proposed to explain why the soluble Mn removal capacity of MnO_x(s) coatings lessen over time with the absence of an oxidant across filter bed.

3.2 Results

3.2.1. Phase identification and microstructure

I. Synchrotron-based X-ray Diffraction

Synchrotron-based X-ray Diffraction (SR-XRD) from dried powder obtained from Mn-Al coating on glass media, and Mn-only and Mn-Al coating on alumina media was performed in order to improve the resolution of spectral features that permit to definitively identify phases present in coatings. Results from these experiments are shown in Figure 3.1. Samples were prepared by the same method used for the powder XRD measurements. Diffraction peaks in each pattern were indexed and compared to previous powder XRD results (figures 2.6, 2.9 and 2.10). For ease of comparison, powder XRD results are summarized in table 3.1. The phases were identified from the peak locations and relative peak intensities. Information for phase identification of poorly crystalline manganese oxide crystal structures was obtained from Zhu et al (2012)[31]. As a reminder, synthetic birnessites (hexagonal–MnO_2 and δ–MnO_2) reported are layered phyllomanganates with hexagonal point group symmetry which differ from each other on their parallel octahedral sheet stacking order in the c-axis. δ–birnessite has randomly stacked octahedral sheets which explains the lack of the (001) reflection in XRD spectra [46, 61-67].

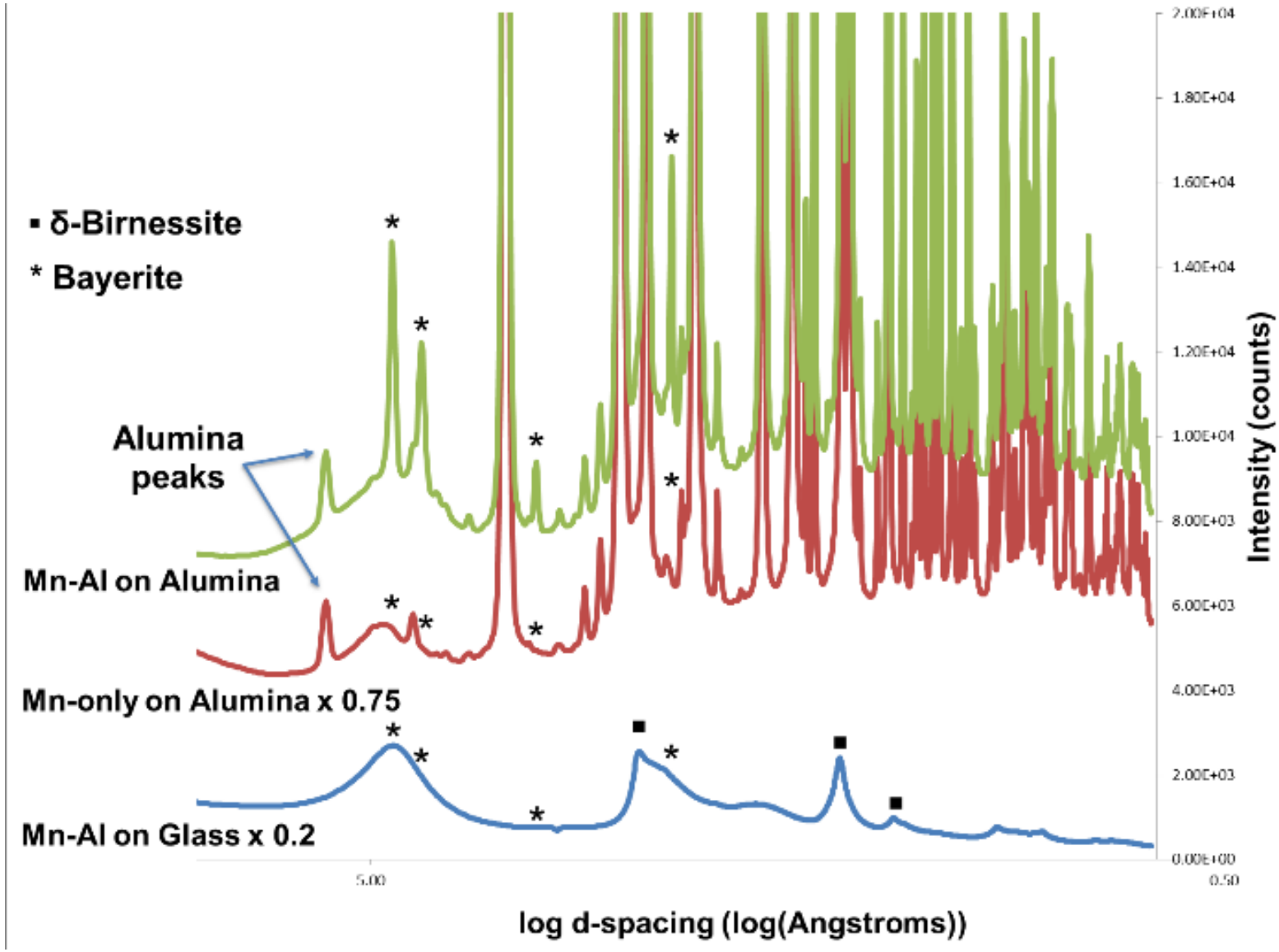

Figure 3.1. Synchrotron-based X-Ray diffraction patterns taken from three different dried samples of coating (Mn-Al on glass, Mn-only and Mn-Al on alumina). Spectra have been scaled down by the factor shown next to their name on label.

Table 3.1. *Summary of phases suggested and identified according to powder XRD analysis presented in chapter 2.*

Media	**Mn–only influent solution**		**Mn–Al influent solution**	
	Mineral Name	**Abundance**	**Mineral Name**	**Abundance**
Alumina spheres	Suggested phases: δ-birnessite Feitknechtite		Identified phases: Bayerite ($Al(OH)_3$) Suggested phases: δ-birnessite Feitknechtite	Minor
Silica Sand	Identified phases: Hexagonal-birnessite	Major	Suggested phases: δ-birnessite Feitknechtite	
Glass Beads	Identified phases: Hexagonal-birnessite	Major	Suggested phases: δ-birnessite Feitknechtite	

Analysis of the SR-XRD data confirmed that the major phase in the Mn-Al on glass sample is a turbostratically disordered birnessite (δ-birnessite). Hexagonal-birnessite was not identified due to the absence of the (001) characteristic basal plane peak, which supports the qualitative interpretation of the powder XRD results in Chapter 2. When comparing Mn-Al coatings formed

on glass and alumina media, sharp peaks of bayerite were only observed from the coating formed on alumina media. This suggests that bayerite in the coating formed on alumina media has greater crystallinity and/or large crystallite size. The phase with the broad peak centered at around 4.7 Å could not be identified.

Meanwhile, Mn-only coating on alumina media showed no bayerite peak. For both Mn-only and Mn-Al coatings on alumina media, a broad peak/hump, ranging from 3.7 to 5.7 Å, was observed. This suggests that an amorphous material is present. It was hypothesized that this material could be an amorphous manganese oxyhydroxide. All these results are consistent with the XRD analysis presented in chapter 2.

II. X-ray Photoemission Spectroscopy

To asses the oxidation states of manganese in the solid phases of surface coatings, X-ray Photoemission Spectroscopy (XPS) analyses were performed on all six surface coatings (namely, Mn-only and Mn-Al coatings on glass, silica sand and alumina media). The resultant spectra with multipeak curve fits for all six samples are presented in figure 3.2. Percentages calculated of Mn (IV), Mn (III), and Mn (II) contributions for each sample are summarized in table 3.2. These inferred oxidation states are consistent with the phases identified by the XRD and SR-XRD analyses. Santelli et al. (2011)[67] determined that δ-birnessite has a lower content of Mn (II) (~5% to 10%) and Mn(III) (less than 25%) with majority of Mn (IV) giving an average oxidation state of 3.9. Hexagonal-birnessite has up to 1/3 of Mn(III) content of all available Mn.

Mn (IV) was the predominant Mn oxidation state in the surface coatings on glass and silica sand media (4 samples). Mn-only coating on glass and silica sand media were the only coatings showing presence of Mn (II) (9% and 17%, respectively). In addition, the reported amount of Mn (II) included possible Mn (II) absorbed to the surface and present in the birnessite and hausmannite phases. These values cannot be estimated separately due to the lack of precise

information regarding Mn (II) content originated in either the adsorption process or in the structure of birnessite and hausmannite.

The presence of Al, either intentionally added or inccidentally supplied from feed water solution or due to dissolution of alumina, increased the percentage of Mn (III) oxidation state in: an additional 15% on glass media, an additional 46% on silica sand media, and an additional 26% on alumina media. Mn - Al coating on alumina media (figure 3.2 -C2-) showed even a predominant Mn (III) oxidation state (81% of total Mn content). These results coupled with previous phase identification by both synchrotron and powder XRD indicated that the predominant phase in Mn-only coatings is hexagonal-birnessite. A poorly-ordered δ-birnessite with a higher Mn (III) content is formed when media is also exposed to Al. The presence of a larger Mn (III) percentage (when Al increases) with no changes in Mn (II) content suggested that feitknechtite or an amorphous Mn oxyhydroxide phase is formed.

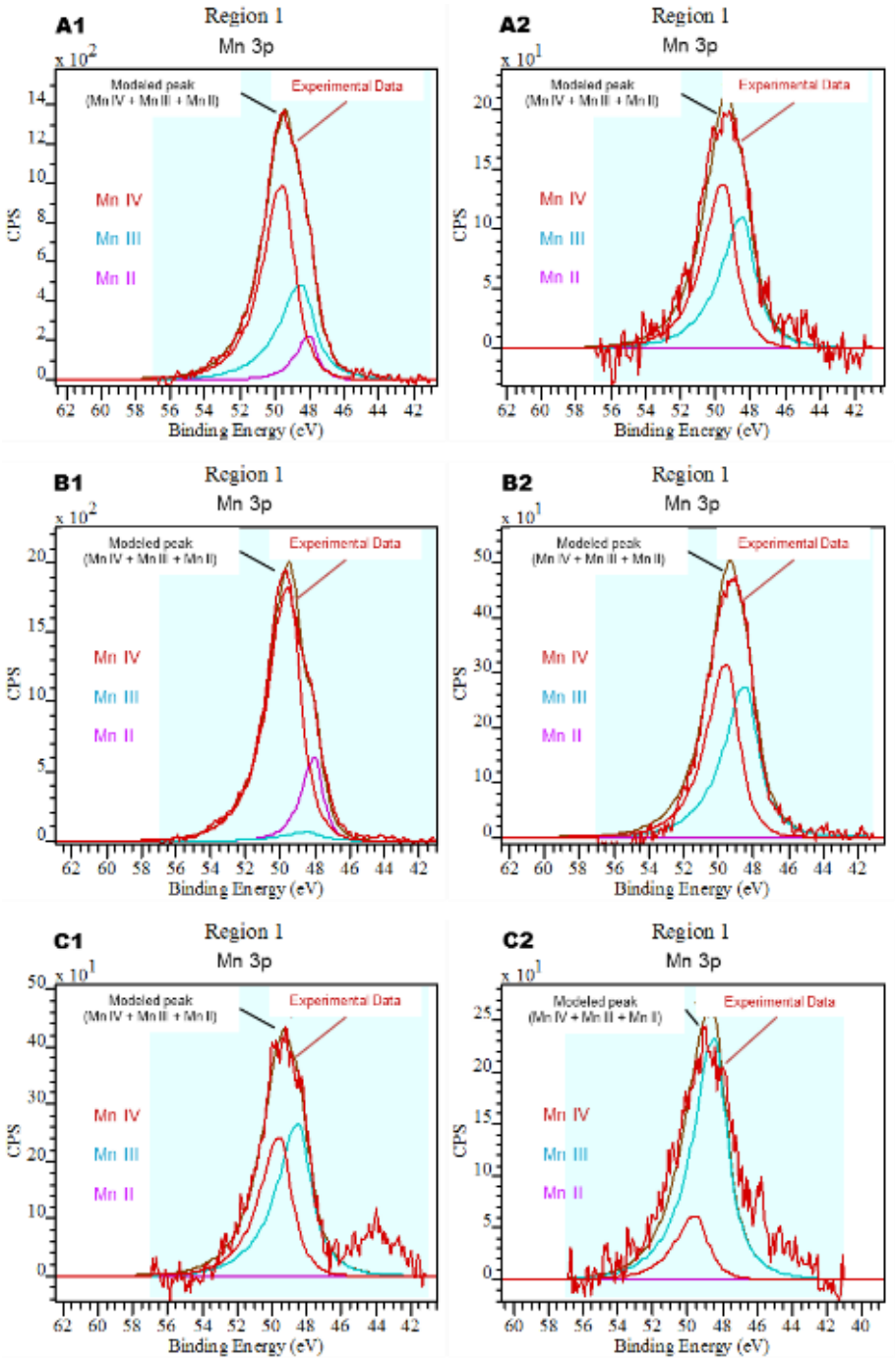

Figure 3.2. X-Ray Photoemission Spectra of a coated area on glass (A), sand (B), and alumina (C) exposed to Mn-only (A1, B1, C1) and Mn-Al (A2, B2, C2) solution respectively for 6 days. Peaks were curve fitted using Mn (II), Mn (III), and Mn (IV) standards. Mn (IV) was usually the predominant oxidation state in coatings. Exposure to Al increased Mn (III) oxidation state in coatings. Mn -Al coating on alumina media (C2) showed the greatest contribution of Mn (III) peak.

Table 3.2. Summary of curve fitting results from analysis of 3p photopeak from different samples.

Sample	Mn II %	Mn III %	Mn IV %
Mn-only on Glass	8.62	32.4	58.98
Mn-only on Sand	17.17	3.05	79.79
Mn-only on Alumina	0 or below detection	55.18	44.82
Mn-Al on Glass	0.04	47.07	52.89
Mn-Al on Sand	0 or below detection	49.41	50.59
Mn-Al on Alumina	0 or below detection	80.78	19.22

III. Transmission Electron Microscopy

TEM analysis was pursued in order to identify and confirm the structure and morphology of coating material at nanoscale. TEM bright field images in fig. 3.3 show morphological features of Mn-only (A1) and Mn-Al (A2) coatings on glass media. An equivalent comparison was made by SEM (fig. 2.15 in Chapter 2). The main difference observed at lower magnification (SEM) was a uniform distribution (continuous film) of Mn-only (A1) versus non-uniform distribution (patchy film) of Mn-Al (A2), respectively. Selected Area Electron Diffraction (SAED) pattern taken from A1 shows overlapping reflections of hausmannite[68] (0.29 nm, 0.25* nm, 0.15 nm), hexagonal-birnessite (0.36* nm, 0.25* nm, 0.23 nm, 0.20 nm), and bayerite (0.47* nm, 0.22 nm, 0.17 nm). Intense reflections in SAED patterns (marked by *) matched with the intense XRD peaks of each corresponding phase suggested or identified in Chapter 2. TEM-EDS spectrum (also in figure 3.3) confirmed the presence of Mn, trace amounts of Al, and O from the analyzed area. SAED pattern from A2 shows overlapping reflections of hausmannite (0.29 nm, 0.25* nm), δ-birnessite (0.25* nm, 0.23 nm, 0.17 nm, 0.14* nm), and bayerite (0.47* nm, 0.44* nm, 0.32 nm, 0.22 nm). TEM-EDS spectrum from A2 showed the presence of Mn, a large peak of Al, and O confirming the presence of an Al-bearing phase (bayerite).

The phase identification results from SAED are confirming those from SR- and powder-XRD results (table 3.1). On the other hand, SAED provided additional information regarding minor phases also present in the coating; for example, bayerite was not previously detected with XRD in A1. This latter phase was unexpected in A1, since Al was not additionally added to the solution. In addition, SAED showed several rings (sometimes diffuse) indicating the combined presence of polycrystalline and amorphous material. The surface coating formed in the absence of Al (A1) appears to be more crystalline (see distinguishable diffraction rings). As inferred from SR-XRD results, the addition of Al likely promotes the formation of amorphous Al-oxy-hydroxide (bayerite) phase.

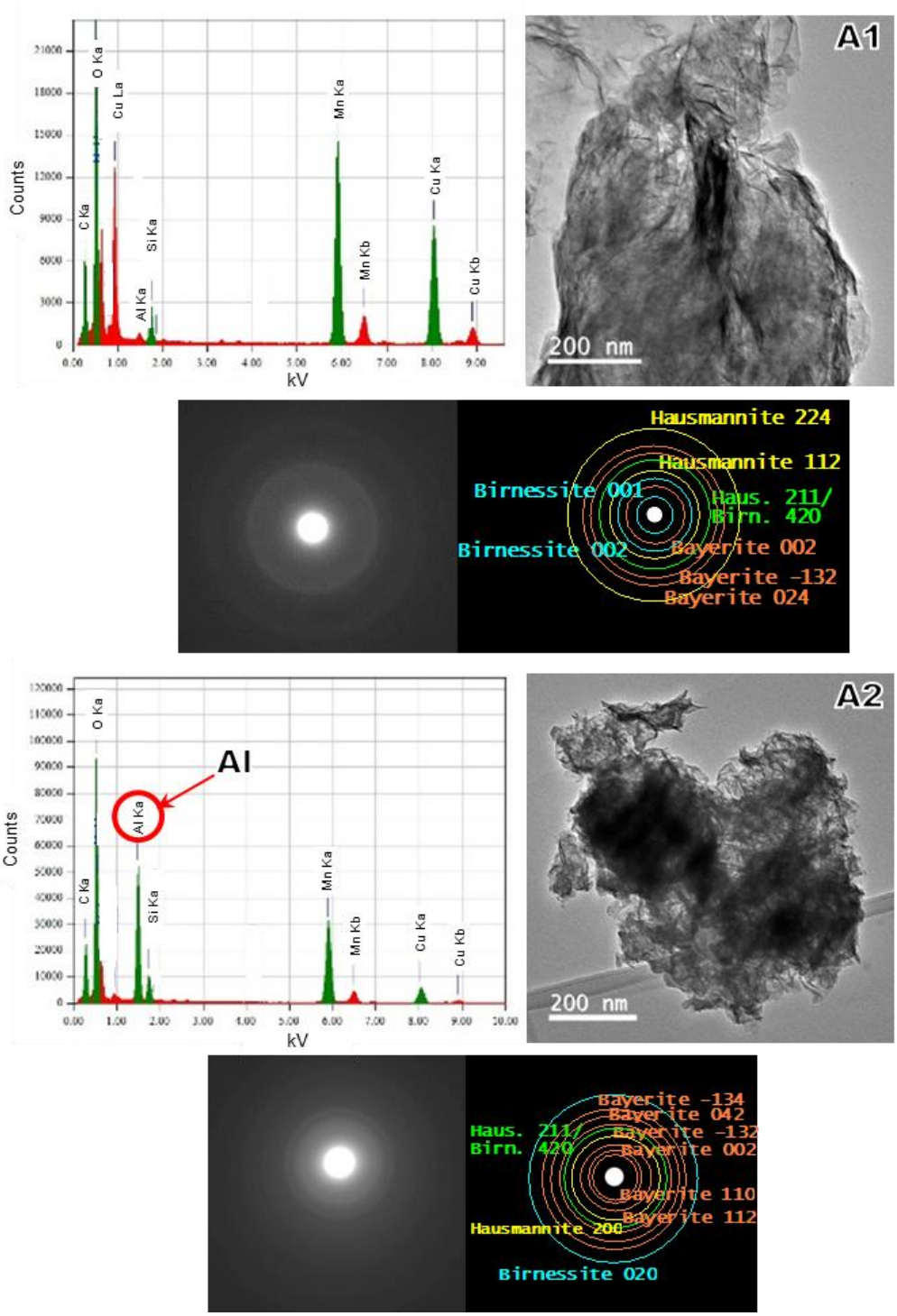

Figure 3.3. TEM micrographs of material dislodged from coating on glass media showing honeycomb-like morphology of around 100 nm in size. A1 presents coating formed on glass exposed to Mn-only solution and A2 coating on glass exposed to Mn-Al solution. EDS spectra confirmed elemental chemistry of area shown.

A series of magnified TEM bright field images (fig. 3.4.) show that MnO_x(s) coatings formed under the same solution composition share the same morphology. When referring to the same solution composition, the media surface hydration and dissolution would affect the coating morphology and these parameters depend on the type of media used. For instance, coating on glass and silica sand media exposed to Mn-only solution (fig. 3.4. A1 and B1 respectively) displayed a configuration of aggregated nanoparticles in a globular form, resembling the classical shape of the mineral hematite or a bunch of grapes. This particular morphology in much larger scale is referred to as botryoidal, and commonly is seen in bulk manganese oxide minerals (in e.g. Ocean Mn Nodules as reported by Post, Jeffrey (1999)[51]). On the other hand, coating on alumina media exposed to Mn-only solution (C1), and coatings formed by exposure to Mn-Al solution on all the three media (glass A2, silica sand B2, and alumina C2) show a poorly crystalline veil-like morphology with the presence of some nanoparticles. These results qualitatively matched XRD identification that suggested the presence of a more ordered hexagonal-birnessite in Mn-only coatings on glass and silica sand media, whereas a less ordered δ-birnessite was observed in coatings formed under the presence of Al. Consequently, these results indicate that Al decreases the degree of crystallinity in MnO_x(s) precipitates.

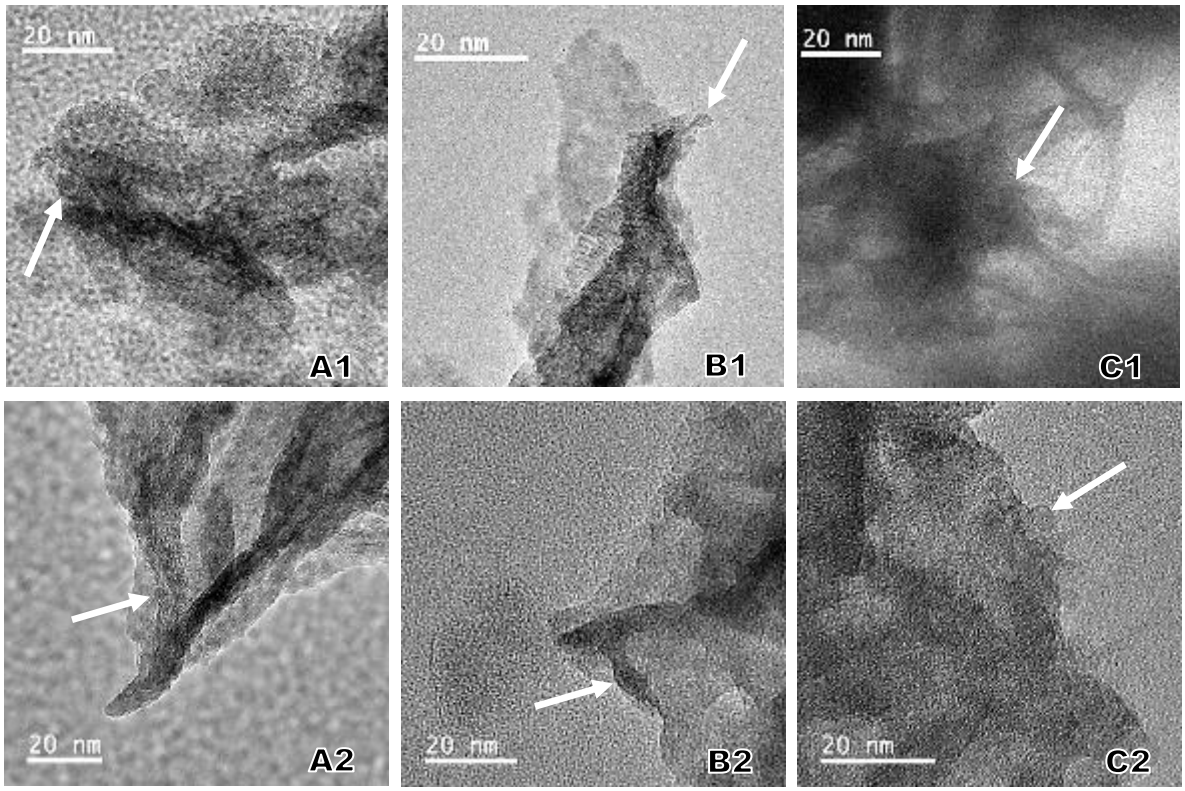

Figure 3.4. High magnification TEM micrographs of Mn-only and Mn-Al coating respectively on glass (A1, A2), sand (B1, B2), and alumina (C1, C2). Mn-only coating in A1 and B1 show nanoparticles in a botryoidal configuration which form clusters and chains. Meanwhile, coatings exposed intentionally or naturally to a Mn-Al (A2, B2, C1, C2) solution are similar to each other with a poorly crystalline veil-like morphology with the presence of some nanoparticles (indicated by arrows).

In figure 3.5 and 3.6, high resolution (HR) TEM images confirm that hexagonal-birnessite and bayerite coexist within a coating, and the morphology can be a folded film or nanoparticles aggregates (in a botryoidal configuration). Lattice fringes from the hexagonal-birnessite {002} reflection ($d \approx 0.36$ nm) and bayerite {002} reflection ($d \approx 0.47$ nm) are well distinguished. In figure 3.5, a mixture of crystalline and amorphous material is observed, supporting the SR-XRD results. In figure 3.6 B, lattice fringes in a nanoparticle corresponding to hexagonal-birnessite are evident, demonstrating that minor quantities of hexagonal-birnessite are present in coatings formed on glass media by exposure to Mn-Al solution. Both SR-XRD and powder XRD did not detect hexagonal-birnessite in this coating, probably due to a low volume fraction (less than 5%). In

figure 3.6 C, a few spotty rings in the SAED were also observed indicating either the presence of well crystallized particles, or some nanoparticles are well aligned to a particular crystallographic direction.

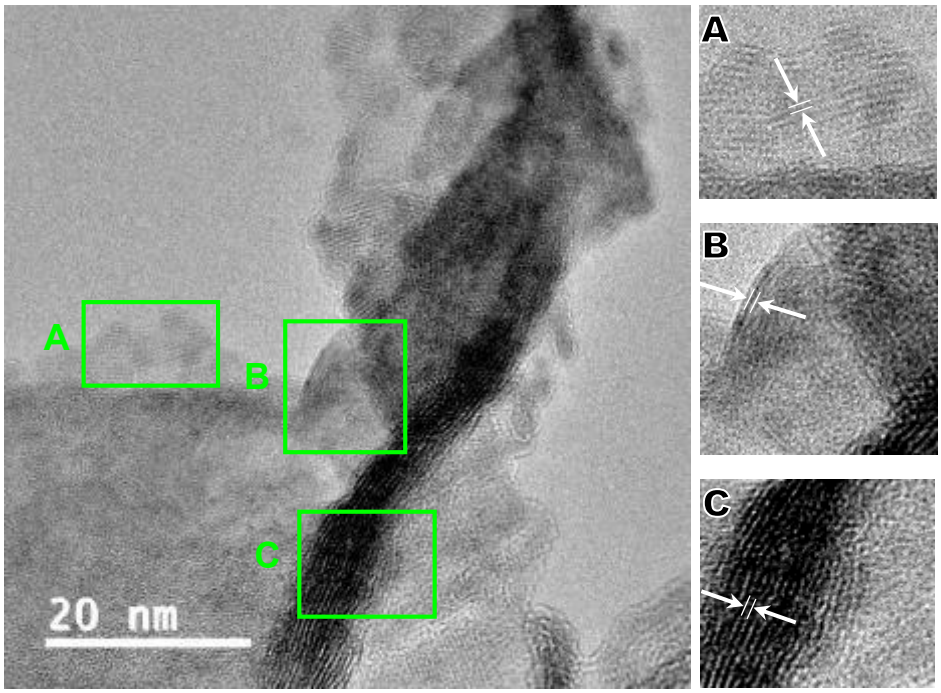

Figure 3.5. TEM micrographs of Mn-only coating on sand showing magnified areas of bayerite {002} reflection with d ≈ 0.47 nm (A) and hexagonal birnessite {002} reflection with d ≈ 0.36 nm (B and C) lattice fringes. D-spacings measured are of approximately 0.47 nm and 0.36 nm correspondingly. A mixture of amorphous and nanocrystalline material can be observed.

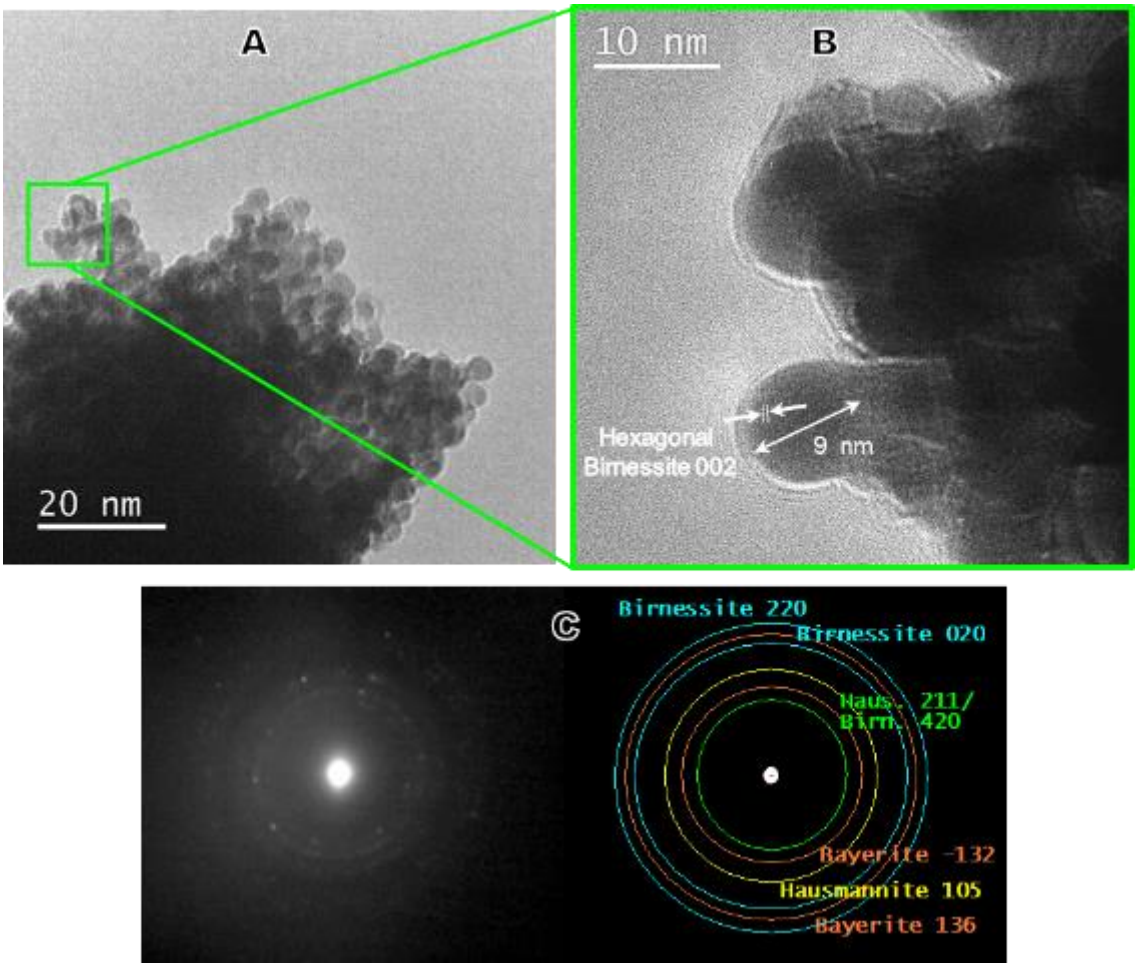

Figure 3.6. A) TEM micrographs of Mn-Al coating on glass showing spherical nanoparticles in a botryoidal configuration with particle size of approximately 9 nm. B) A magnified area of A depicting a nanoparticle with hexagonal birnessite {002} lattice fringes. C) SAED from A showing presence of birnessite, bayerite and hausmannite reflections. Micrographs were taken at 30kV.

In figure 3.7, SAED, bright field image, and a series of dark field images of Mn-only coating on glass media demonstrate an inhomogeneous distribution of birnessite, hausmannite and bayerite. Dark field images were obtained by selecting either one diffraction spot or a small section of one diffraction ring that was a diagnostic reflection from the phase of interest and had minimal overlap with other diffraction spot/rings from other phases. The diffracted beam was selected by using the smallest objective aperture available on the instrument (the effective size of 1.1 [1/nm]). Hexagonal birnessite (001) reflection (d≈0.73 nm), delta birnessite (310) reflection (d≈0.14 nm),

hausmannite (224) reflection (d≈0.16 nm), and bayerite ($\bar{1}32$) reflection (d≈0.22 nm) were used in this study. All the diagnostic reflections are labeled in the experimental SAED pattern in fig. 3.7. Figure 3.7A shows the distribution of birnessite within a 150nm diameter area. A combination of isolated and aggregated nanoparticles can be observed. In figure 3.7B, hausmannite is observed. This phase seems to be mainly located adjacent to birnessite particles forming larger aggregates. In figure 3.7C, bayerite is confirmed as a minor phase that has co-precipitated as small particles. Bayerite is formed as a result of the presence of Al in the feed water solution.

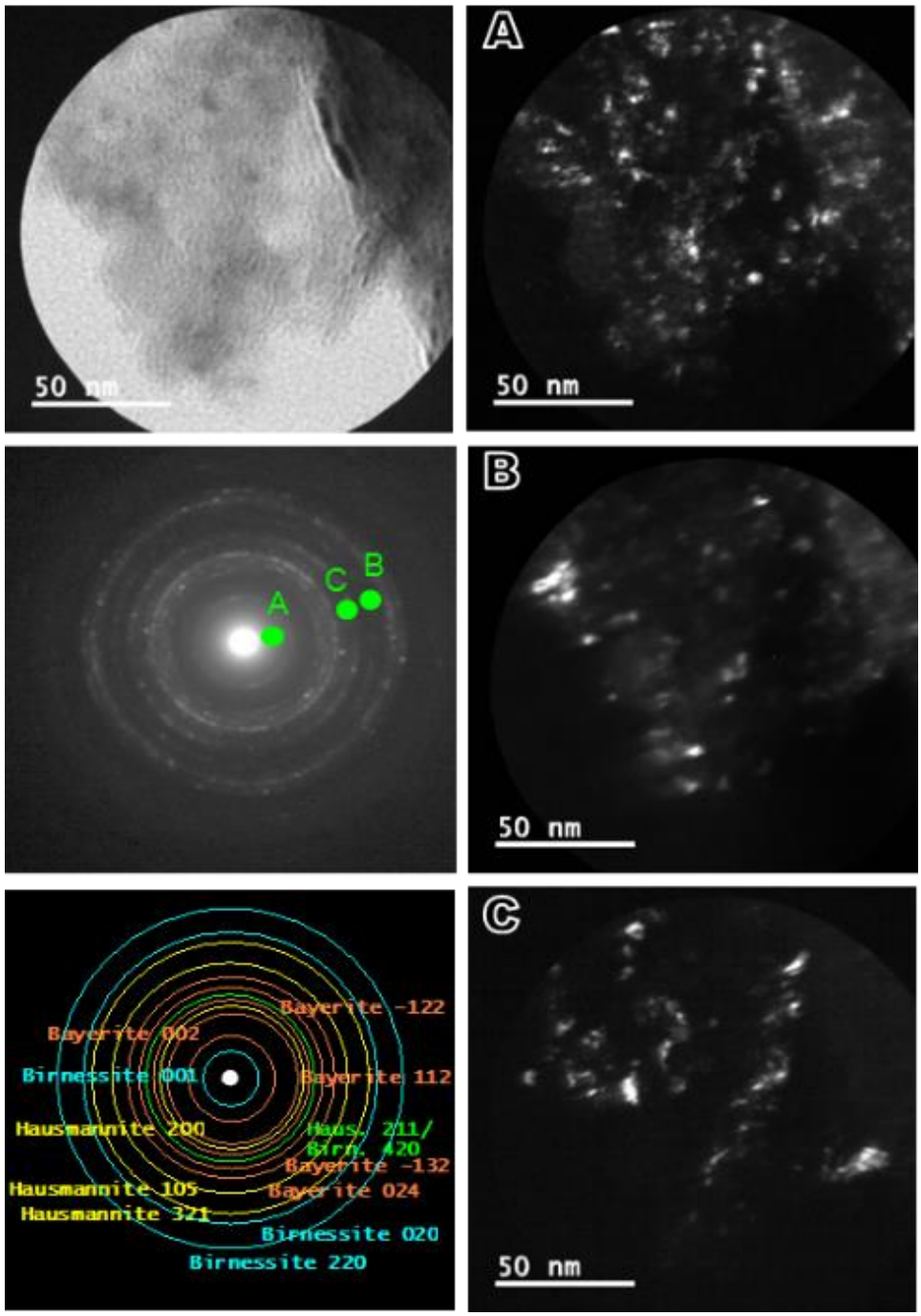

Figure 3.7. TEM SAED and BF/DF micrographs of imhomogeneously distributed phases (birnessite predominantly, hausmannite and bayerite) present in coating exposed to Mn-only dose on glass media. A) DF image of hexagonal birnessite {001} reflection (d≈0.73 nm). B) DF image of hausmannite {224} and {321} reflections (d≈0.16 nm). C) DF image of bayerite $\{\bar{1}32\}$ and {024} reflections (d≈0.22 nm and d≈0.21 nm). The effective size of the objective aperture used was 1.1 [1/nm].

In figure 3.8, a pair of bright and dark field images from Mn-only coating on glass media demonstrated further that coating consists of a mixture of amorphous and nanocrystalline particles. This data was taken from a different area of fig. 3.7. The dark field image was taken by using a part of birnessite {002} reflection (d=0.36 nm). Assuming the particles observed are nearly spherical, the average particle size was calculated by measuring 160 particles. The same procedure was applied for Mn-Al coating on glass media (fig. 3.9). The particles in the Mn-only coating have the average size of 4 nm, whereas the particles from the Mn-Al coating have an average size of 8 nm. The particle size distribution in both cases is multimodal with values ranging from 2 to 11 nm.

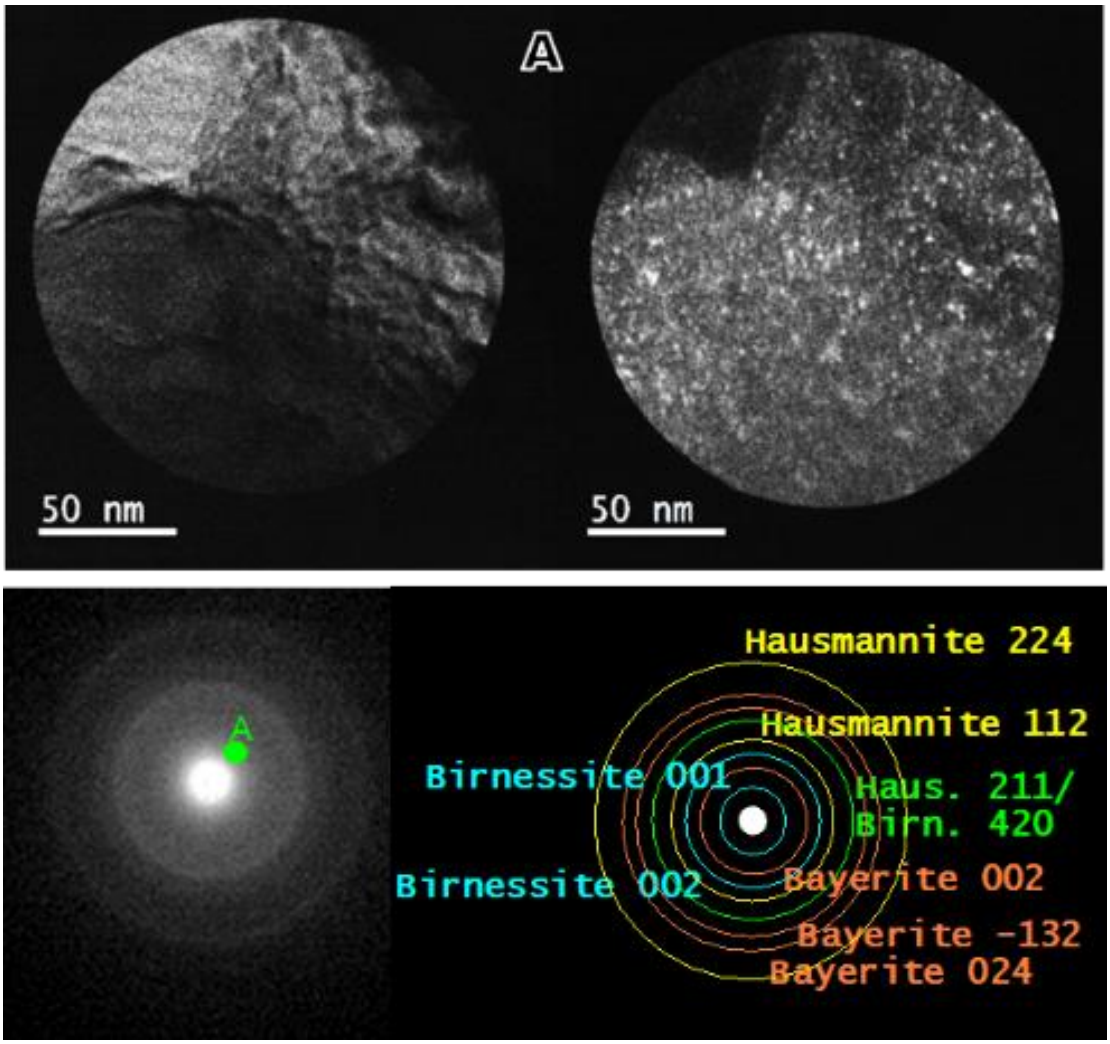

Figure 3.8. SAED and BF/DF images showing the hexagonal birnessite phase present in the coating exposed to Mn-only dose on glass media.

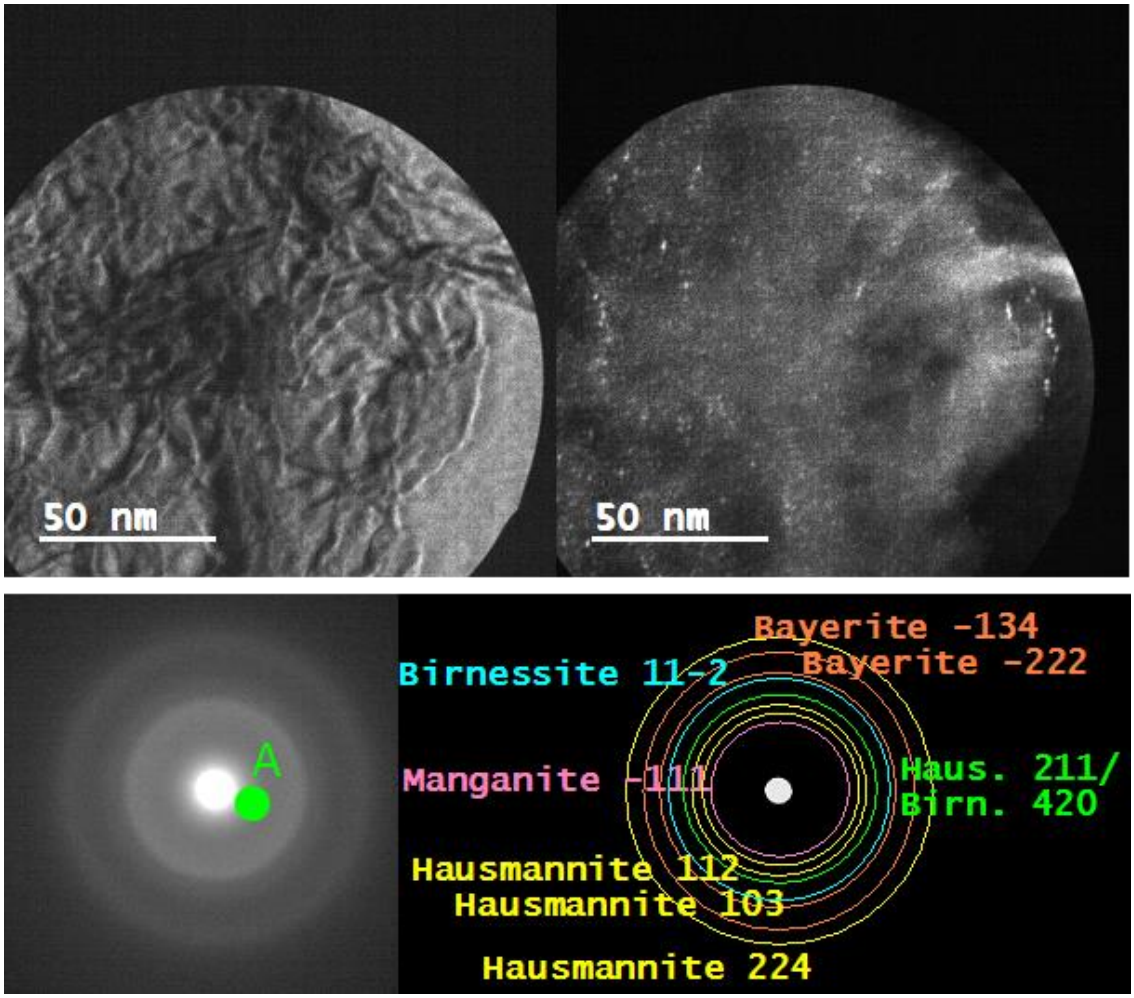

Figure 3.9. SAED and BF/DF images showing the delta birnessite phase present in the coating exposed to Mn-Al dose on glass media. The area selected correspond to the asymmetrical broad peak of delta birnessite in the range of d-spacings between 0.6 and 1.4 nm.

3.2.2 Coating evolution

In figure 3.10, SEM micrographs show the morphology of Mn-only coating on silica sand media. These images were taken in grooves formed when the coating was dehydrated under vacuum and partly by the electron beam illumination (likely, localized heating). The grooves reveal a cross-section of the coating. Figure 3.10 D suggests that a layer by layer stacking occurred. Since this groove was created during observation, it is very likely that water originally retained deep in the coating tore up the coating by vaporization. Consequently, water was likely present

in the empty space between honeycomb-like sheets of birnessite. This empty space has been proposed as the primary location for water adsorption[31, 51, 56, 57, 69] .

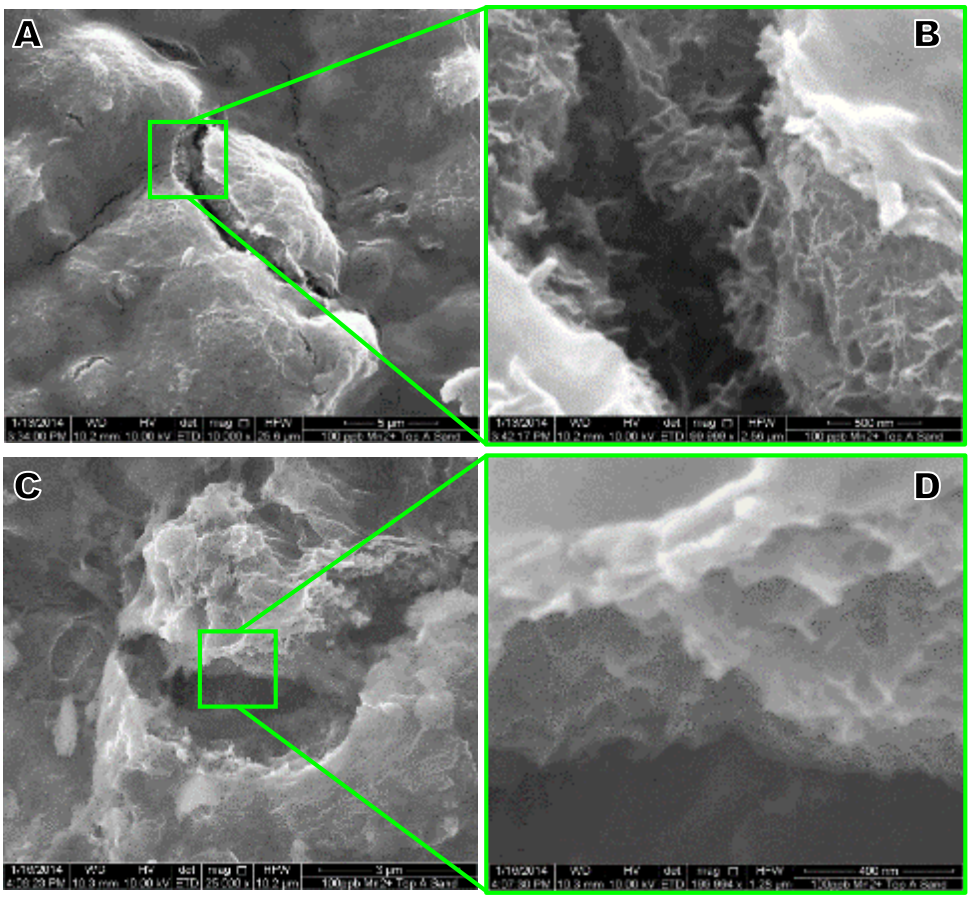

Figure 3.10. SEM micrographs of Mn-only coating on silica sand media. Images were captured in different locations from the same granule of coated sand.

To elucidate the effect of solution composition in the morphology and structure of coatings, deposits were formed on acrylic media by varying the solution composition with time according to the sequence presented in table 1.1. Cross-section samples were obtained by slicing a thin foil of the coating attached to an acrylic sphere using microtome. Samples were taken at the end of the column experiments and analyzed in the same way as other coatings. Two representative images of the coatings formed are presented in figure 3.11. Two different morphologies were obtained by changing the solution composition sequence. A highly dense honeycomb-like morphology

(labeled as H) was identified to be mainly hexagonal-birnessite by the presence of the characteristic (001) and (002) reflections (d≈0.72 nm and d≈0.36 nm) in the correspondent SAED pattern. This phase was always present as the very first surface coating layer, near the surface of media. Meanwhile, coating material with morphology resembling sheets/films that easily fold over themselves (labeled as D) was identified as coating with a predominant presence of δ-birnessite. In both cases, Al (oxy)hydroxide co-precipitated and was also present in the coating as a minor phase. TEM-EDS performed in these two areas did not show appreciable differences in elemental chemistry (Al, Mn, and O peaks were always present). A mixture of Mn and Al containing species were always present, indicating that Al species were incorporated on the coating. Usually, the Al oxyhydroxide phase is removed from the surface of media during backwash.

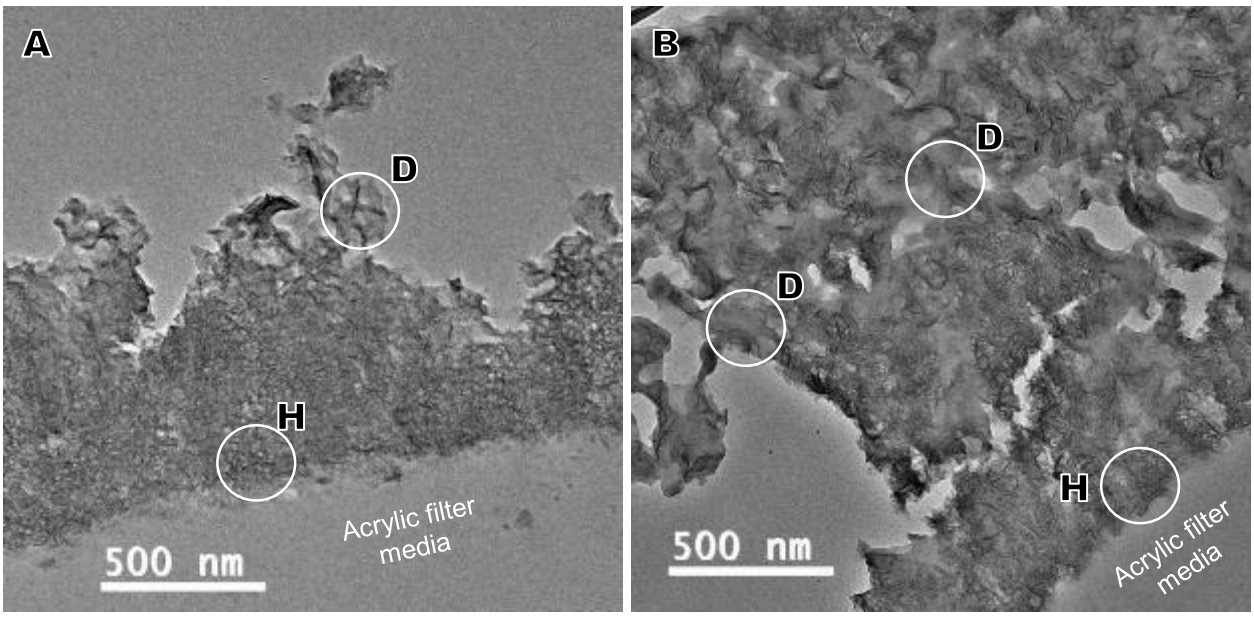

Figure 3.11. TEM micrographs of cross-section of coating formed on acrylic media by varying solution composition per table 1.1 (A and B denotes column A and B respectively). Samples analyzed were obtained at the end of column experiments. Acrylic media was used for ease of cutting with microtome knife.

The coating evolution was further investigated using XPS. Spectra were obtained from coated acrylic spheres retrieved at different instances/steps of coating evolution. The resultant spectra with multi-peak fits for the Mn 3p orbitals for four samples are presented in figure 3.12. Calculated percentages of Mn (IV), Mn (III), and Mn (II) contributions for each sample are summarized in table 3.3. Results showed that the Mn oxidation state of the coatings were mainly Mn (IV) and Mn (III). The ratio of Mn(II)-(IV) oxidation states for each sample is very similar to each other (see Table 3.3), except for sample A15. When comparing the sample A15 with the sample B15, an additional 16% in the Mn (III) content was observed. This difference can be explained by the change of conditions in influent water chemistry. The sample A15 was exposed to an Al-only solution prior its last exposure to Mn-only solution. Meanwhile, the sample B15 was exposed to a Mn-Al solution instead. This very strongly suggests that the presence of Al increased the content of Mn (III) oxidation.

Note that the sequence of solution composition applied to sample A15 (15 days of operation in column A) was the following: 3 days subjected to an Al-only solution, 3 days to a Mn-Al solution, 2 days to an Al-only solution, 1 day to a Mn-Al solution, 3 days to an Al-only solution, and –finally- 3 days to a Mn-only solution. Sample A18 (18 days of operation in column A) were subjected to the same sequence with 3 additionally days subjected to a Mn-Al solution.

Sample B8 (8 days of operation in column B) was subjected to 3 days to a Mn-Al solution and 5 days to an Al-only solution. Sample B15 (15 days of operation in column B) was exposed to an additional day to an Al-only solution, 3 days to a Mn-Al solution, and 3 days to a Mn-only solution as a final step.

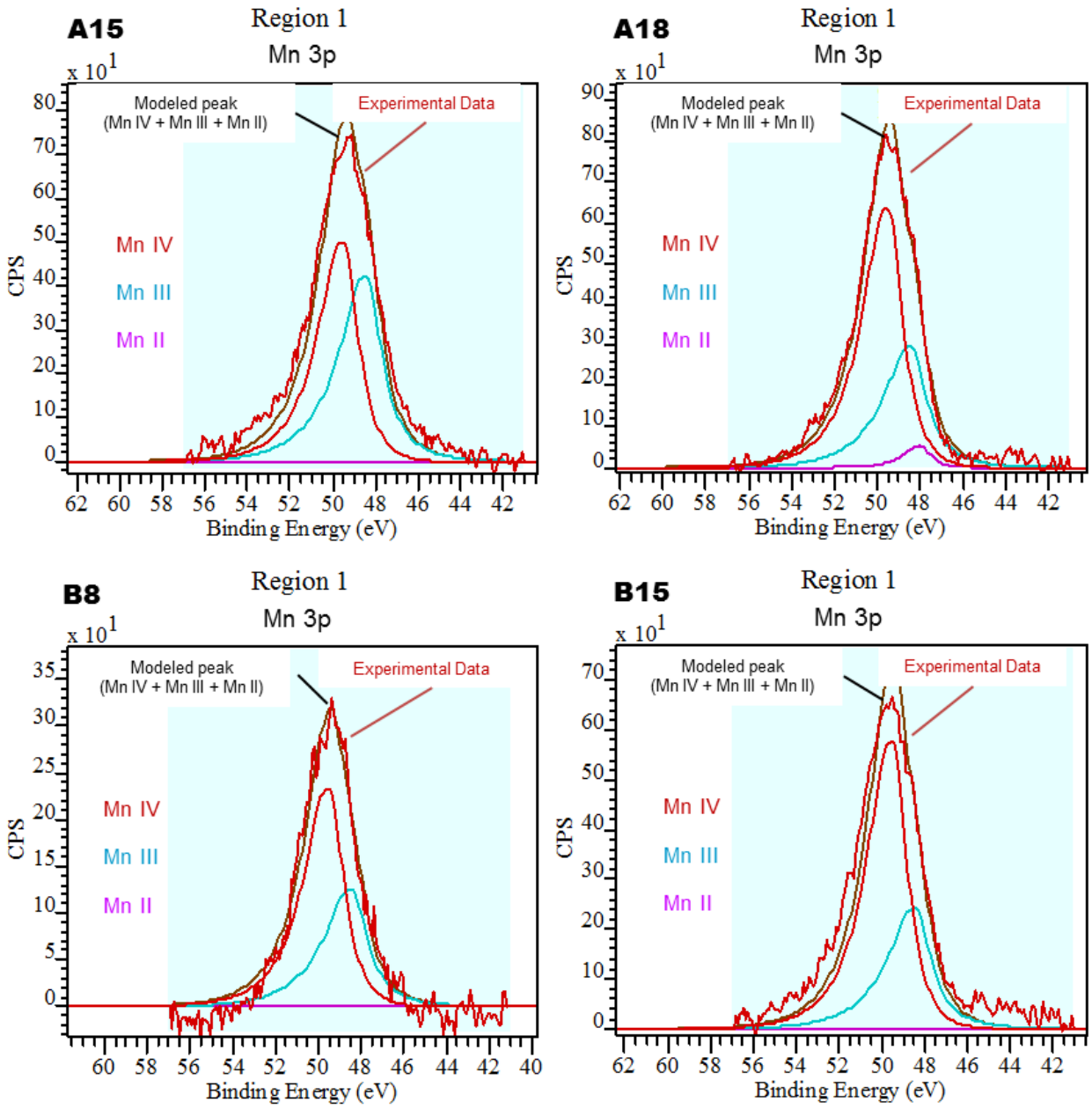

Figure 3.12. X-Ray Photoelectron spectra of coating formed on acrylic media by exposure to different solution composition per table 1.1. Peaks were curve fitted using Mn (II), Mn (III), and Mn (IV) standards.

Table 3.3. Summary of curve fitting results from analysis of 3p photopeak from different samples.

Sample	Mn II %	Mn III %	Mn IV %
A15	0 or below detection	48.72	51.28
A18	3.48	32.94	63.58
B8	0 or below detection	37.50	62.50
B15	0 or below detection	32.06	67.94

3.3. Discussion

3.3.1. Phase identification and microstructure

Micrometer scale (powder XRD, SR-XRD, XPS) and nanometer scale (TEM) analyses permit identification of the phases formed in surface coatings. The major phase in all coatings is a layered-type birnessite resembling the synthetic analog of hexagonal-birnessite, formed in coatings exposed to Mn-only solution, or δ-birnessite when coatings are formed under the presence of Al. In addition, hausmannite (Mn_3O_4) and bayerite (Al oxy(hydr)oxide) are found to co-precipitate and get incorporated into the coating.

Several authors[46, 62, 66, 67] have reported that the Mn oxidation state of these two layered birnessites (δ and hexagonal) is predominantly Mn (IV) with a small contribution of Mn (III) and Mn (II) which matched with the XPS results obtained for coatings formed in the presence of a Mn-only solution. For example, the prototype birnessite's chemistry by Post[51] is [Na, Ca, Mn^{2+}] Mn_7O_{14}•$2.8H_2O$. The Mn_7O_{14} (or MnO_6) octahedra contains only Mn^{3+} and Mn^{4+} whereas a small amount of Mn^{2+} may be a result of intercalation. Thus, both birnessites (regardless δ or hexagonal) and/or hausmannite could be responsible for the presence of Mn(II). When media was exposed to Mn-Al solution, the Mn oxidation state of coatings changed significantly; an increased

contribution of Mn (III) and a reduction in the percentage of Mn (II) (Table 3.2) were observed. δ-birnessite is the predominant phase in the Mn-Al coatings, and this phase has been shown to be actively contributing/participating in the Mn (II) oxidation process according to other studies[46, 50, 62, 66, 67]. Thus, δ-birnessite evidently contributes to reducing the amount of Mn (II) in coatings to below the detection limit of XPS. The experimental observed improvements of Mn (II) removal by the presence of Al also stimulates Mn (II) oxidation.

TEM results (Figures 3.3 – 3.9) elucidated the inhomogeneous nature of coatings at the nanoscale, i.e., multiple manganese oxide phases are intermingled and they range from amorphous to nanocrystal. They also provided evidence of the coexistence of minor phases that were not resolved by other characterization tools. XRD and SR-XRD indicate the coexistence of multiple phases, but cannot detect phases with low volume fractions. In turn, TEM allows for identifying the location of nanoparticles within coatings, their morphology, size, existence form (such as aggregates or single substance), and their crystal structure.

In addition to the identification of coating morphology and confirmation of the size of features and crystallites, TEM provides insights regarding coating evolution. An interesting result is the observed presence of nanoparticles in a botryoidal configuration in some coatings. When observed, these nanoparticle aggregates were always formed in between layered films. This demonstrates that the precipitation of MnO_x(s) nanoparticles concurrently occurred with the film formation. First, poorly crystallized nanoparticles form in solution and precipitate on rough areas on the surface of filter media, forming birnessite. Birnessite in turn promotes the surface-catalyzed oxidation of soluble Mn, forming additional birnessite and either hausmannite (pH between 8.0 and 8.5) or an amorphous manganite-like phase (pH between 7.0 to 8.0). At the same time, nanoparticles keep forming in solution and attach to the recently formed coating. In fact, the phase transformation process between birnessite and hausmannite seems almost reversible. In

terms of time scale and of relative phase concentration, birnessite promotes hausmannite in this particular study. According to Elzinga,E.J. (2011) and Lefkowitz et al. (2013), the transformation from birnessite to hausmannite can be achieved in a few days (with an intermediate metastable phase: feitknechtite (β-MnOOH)). Since birnessite is the major phase present and hausmannite the minor, the author concludes that birnessite likely promotes hausmannite formation rather than hausmannite converting to birnessite. The latter sequence is believed to be slower than the former.

It is also proposed that a localized modification of environmental conditions at the nanoscale is occurring at the surface of filter media (such as an inhomogeneous distribution of zeta potential as noted by Jinkeun et al. (2006)[70] which can further impact positively in the Mn (II) removal process by promoting heterogeneous oxidation of Mn (II), forming MnO_x(s) nanoparticles.

In summary, as proposed in the Chapter 2, the proposed coating growth model is: poorly crystallized nanoparticles $\rightarrow$ birnessite $\rightarrow$ form and precipitate more birnessite and at the same time form feitknechtite $\rightarrow$ feitknechtite transform to hausmannite (Mn-only samples) or to a manganite-like material (these could be the amorphous material formed when Al is present, such as in Mn-Al coating on all media and Mn-only coating on alumina media). TEM characterization provides the following experimental evidences to support the proposed growth model in addition to the structure identification of nanophases:

1) a precipitation process is occurring in which MnO_x(s) nanoparticles are being formed (based on observed botryoidal morphology).
2) an autocatalytic oxidation of soluble manganese on their surface in combination with precipitation of poorly crystallized nanoparticles, and formation of hausmannite take place.

3) a precipitation and growth mechanism in combination with an autocatalytic oxidation mechanism would take place nearly concurrently rather than sequentially.

3.3.2. Coating evolution

SEM (figure 3.10), TEM (figure 3.11) and XPS (figure 3.12) observations indicate that the basic structure unit of the coatings is a thin film. Each film layer preferentially grows two-dimensionally and then eventually stacks one on top of the other. Coatings grow laterally (2D) between previously formed MnO_x(s) coatings, filter media surface and water solution. Then, coatings grow upwards towards the solution. In the case of Mn-Al coatings, coatings preferentially grow on suspended solids already deposited on media surface (Al oxyhydroxide). This would be the main reason why aggregates of birnessite attached frequently to the rough surface of filter media (patchy features in Figures 2.14 through 2.20).

Only Mn-only coatings on silica sand and glass media have XRD detectable volume fraction of hexagonal-birnessite. Thus, the formed δ-birnessite likely remains as is within the time frame of this study. Consequently, the author speculates that delta birnessite is more stable than the hexagonal counterpart in the experimental conditions of this study. However, if an aging process at ambient temperature simultaneously took place, a poorly ordered δ-birnessite may transform to a higher ordered hexagonal counterpart as shown in other studies[59, 71, 72]. Learman et al.[50] have suggested that colloidal δ-birnessite is more effective in oxidizing Mn (II) than particulate triclinic birnessite (a more ordered birnessite phase that is believed to form by aging of the delta phase). They have proposed that transformation begins with δ-birnessite, goes through hexagonal -birnessite, and then forms the triclinic one. When the triclinic birnessite is obtained, the catalytic behavior is highly reduced. This phase transformation could explain the need of adding free chlorine across the filter to reactivate the catalytic effect of MnO_x(s) coatings

in water facilities when the Mn removal efficiency has decreased. By adding the oxidant, formation of new colloidal δ-birnessite with greater catalytic properties is achieved. These colloids are then captured and incorporated into the coating, recovering its capacity for further Mn (II) capture. As this phase transformation could be happening over a long duration, further study is required to draw a definitive conclusion.

CHAPTER 4. Numerical modeling of the influence of filter media characteristics on the initial formation of manganese-oxides coatings on filter media during water filtration.

4.1. Summary

This modeling exercise was undertaken to evaluate the influence of microscale surface topography, crystal structure and chemistry of filter media on the initial formation of manganese-oxides ($MnO_x(s)$) coatings on filter media. The approach assumed that at very early stages only heterogeneous oxidation of ionic manganese occurs, forming nanoparticles. This numerical modeling used extended DLVO theory taking into account surface heterogeneity to obtain $MnO_x(s)$ colloidal particle - filter media interaction energy curves for five different geometrical configurations. Figure 4.1 shows schematics of the five study cases of colloid – rough surface interactions for which the interaction curves are calculated. Asperity radii used correspond to a smooth surface (no asperity), arithmetic mean value of surface roughness (Ra), and highest asperity (see table 4.1). The model also assumed that $MnO_x(s)$ coatings were developed on three different filter media in a bench-scale column. The column contained only one type of filter media, and an identical simulated inorganic aqueous chemistry was used for all the three media. For evaluating the effect of Alum addition in the interaction curves, a spherical charge-neutralized cluster of combined manganese-oxides and aluminum-hydroxide nanoparticles was assumed. As mentioned in the previous chapter, the simulated inorganic aqueous chemistry follows that of a typical coagulation fresh water treatment plant where free chlorine is used as an oxidant across the filter bed. Correspondent previous experimental investigations (chapter 2 and 3) matched well

with theoretical results, suggesting that media surface roughness and morphology are major contributing factors of the process.

4.2. Results

4.2.1 Rough surface model

According the rough surface model by Shen et al. (2012), the filter media morphology and roughness are suggested to be determining factors for the location of favorable sites for colloidal particle deposition on the media surface. The surface roughness is taken into account in the Shen's model by summation of colloid-surface ps (sphere-plate) and colloid-asperity pg (sphere-sphere) interaction energies using the DLVO theory. Then, three energies are added for each of the two interactions: retarded van der Waals attraction (Φ^{vdW}), electrical double layer potential (Φ^{dl}), and Born repulsion potential (Φ^{Born}). Equations below were derived for calculations where:

A is the Hamaker constant

a_g is the asperity (protrusion) radius

a_p is the colloid (particle) radius

h is the surface-to-surface separation distance between colloid and asperity

H is the colloid-flat surface separation distance

λ is the dielectric characteristic wavelength taken as 100 nm (Hahn and O'Melia, 2004; Hahn et al., 2004) [73, 74]

ε_0 is the permittivity of vacuum

ε is the relative permittivity of water

κ is the reciprocal double layer thickness (Israelachvili, 2011)[75]

ψ_p is the zeta potential of the colloid

ψ_g is the zeta potential of the asperity assumed to be equal to the zeta potential of the surface ψ_s

$x = \frac{a_g}{a_p}$ is the radius ratio of asperity to colloid

$R = 1 + x + \frac{h}{a_p}$ is the center-to-center separation distance normalized by a_p

σ is the collision diameter, which experimental value has been determined to be 0.5 nm (Ruckenstein and Prieve, 1976; Feke et al., 1984; Hahn et al., 2004)[73, 76, 77].

Interaction energy curves were calculated for five different configurations of a spherical colloid particle approaching a rough surface (modelled as a flat surface with hemispherical asperities/protrusions). Asperity (protrusion) and colloid (nanoparticle) radius for model calculations were obtained experimentally. Nanoparticle size were measured using TEM (figure 3.8 in chapter 3), and two radii were selected for model calculations, i.e., 1 nm and 4 nm. For evaluating the effect of Alum addition, a spherical destabilized cluster of combined manganese-oxides ($MnO_x(s)$) and aluminum-hydroxide ($Al(OH)_3$) nanoparticles with a diameter of 11 nm (the largest size of nanoparticles measured by TEM in figure 3.8 in chapter 3) was assumed. According to Amirtharajah's discussion (1988)[17] on Alum coagulation diagram and zeta potential, at the pH of the performed experiments (7.3) and the concentration of Alum (0.22 mg/L), charge neutralization would most likely take place with aluminum-hydroxide coating the $MnO_x(s)$ particles. With regards to the asperity radius, AFM measurements were performed to monitor surface roughness (results are presented in the next section). Asperity radii for each media was selected by assuming the arithmetic mean value of surface roughness (Ra) (Table 4.1) as the smaller asperity radius; and, the largest protrusion height value measured on tested surfaces as the largest asperity radius. These are 11 and 100 nm for glass, 150 and 4000 nm for silica sand, and 189 and 3000 nm for alumina, respectively. Additional parameters needed for calculations

were obtained from published data with the same or very similar experimental conditions of the column tests used in this study (25° C, 1 atm, pH of 7.3, ionic strength of 0.002 M, oxic conditions: 8 mg/l of dissolved oxygen, systems: filter media –water- colloidal MnO_x(s)) (Petosa et al., 2010; Shen et al., 2012; Hahn et al., 2004; Israelachvili, J.N., 2011; Ruckenstein and Prieve, 1976; Feke et al., 1984; Bergström, L., 1997; Zhu et al., 2011; Shen et al., 2011; Fuerstenau and Shibata, 1999; Sprycha, R., 1989)[18, 25, 73, 75-82].

For retarded van der Waals attraction (Φ^{vdW}):

$$\Phi_{pg}^{vdW}(h) = -\frac{Aa_g a_p}{6(a_p+a_g)h}\left(\frac{1}{1+11.12\frac{h}{\lambda}}\right) \quad (2)$$

$$\Phi_{ps}^{vdW}(H) = -\frac{Aa_p}{6H}\left(\frac{1}{1+11.12\frac{H}{\lambda}}\right) \quad (3)$$

For electrical double layer potential (Φ^{dl}):

$$\Phi_{pg}^{dl}(h) = \frac{\pi\varepsilon\varepsilon_0 a_g a_p}{a_g+a_p}\left\{2\psi_p\psi_g \ln\left[\frac{1+\exp(-\kappa h)}{1-\exp(-\kappa h)}\right] + \left(\psi_p^2+\psi_g^2\right)\ln[1-exp(-2\kappa h)]\right\} \quad (4)$$

$$\Phi_{ps}^{dl}(H) = \pi\varepsilon\varepsilon_0 a_p\left\{2\psi_p\psi_s \ln\left[\frac{1+\exp(-\kappa H)}{1-\exp(-\kappa H)}\right] + \left(\psi_p^2+\psi_s^2\right)\ln[1-exp(-2\kappa H)]\right\} \quad (5)$$

For Born repulsion potential (Φ^{Born}):

$$\Phi_{pg}^{Born}(h) = \frac{A}{37800R}\left(\frac{\sigma}{a_p}\right)^6\left[\frac{-R^2-7(x-1)R-6(x^2-7x+1)}{(R-1+x)^7} + \frac{-R^2+7(x-1)R-6(x^2-7x+1)}{(R+1-x)^7} + \right.$$

$$\left.\frac{R^2+7(x+1)R+6(x^2+7x+1)}{(R+1+x)^7} + \frac{R^2-7(x+1)R+6(x^2+7x+1)}{(R-1-x)^7}\right] \quad (6)$$

$$\Phi_{ps}^{Born}(H) = \frac{A\sigma^6}{7560}\left[\frac{8a_p+H}{(2a_p+H)^7} + \frac{6a_p-H}{H^7}\right] \quad (7)$$

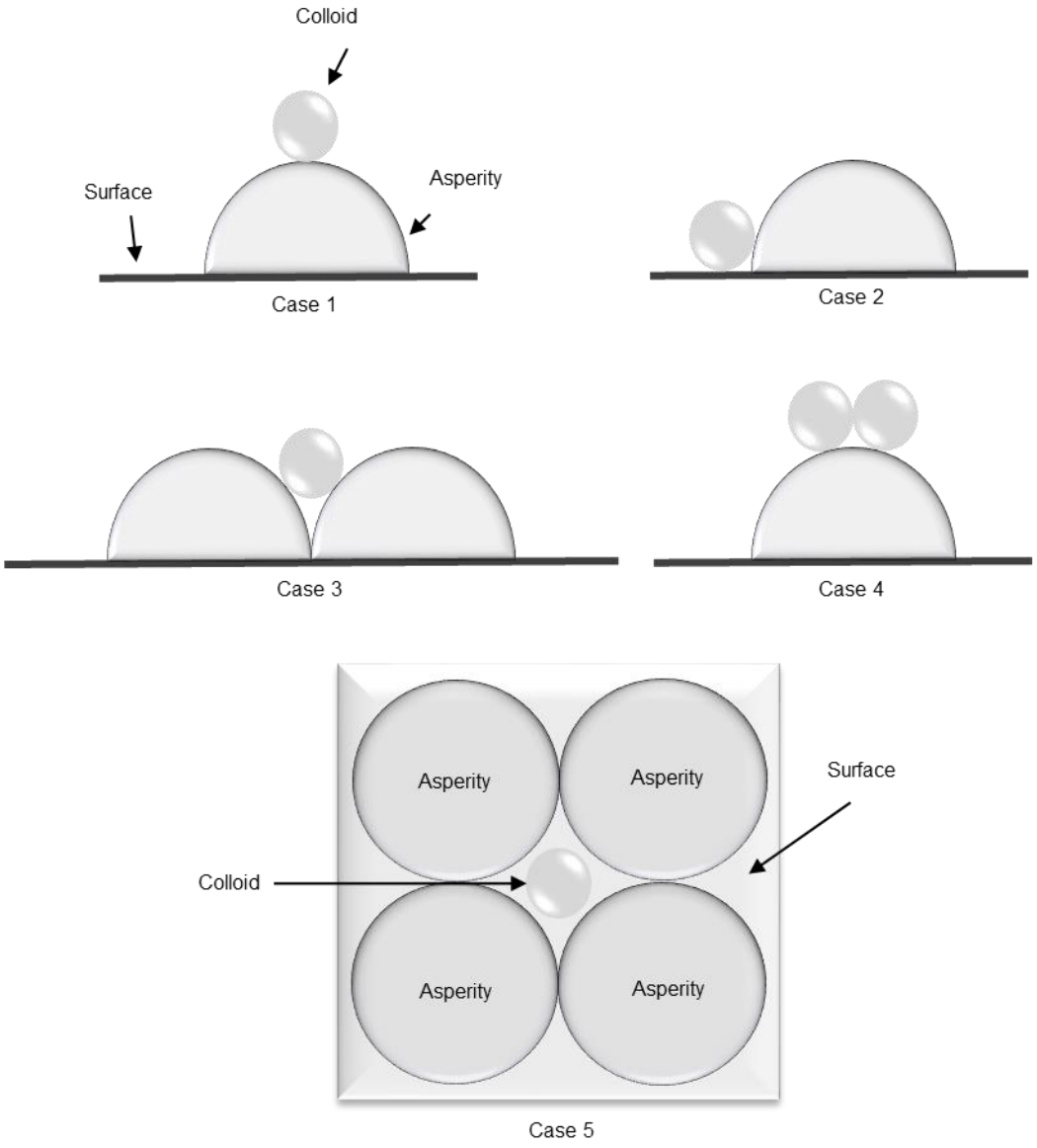

Figure 4.1. Schematics of the five cases of colloid – rough surface interactions that are studied applying the rough surface model following (Shen et al. 2012). Asperities are considered as hemispheres and colloids as spheres.

The total extended DLVO interaction energies (Φ_T) for these five cases with respect to h only are:

Case 1: $\Phi_T = \Phi_{pg}(h) + \Phi_{ps}(h + a_g)$ (8)

Case 2: $\Phi_T = \Phi_{pg}(h) + \Phi_{ps}\left[\sqrt{(h + a_p)^2 + 2ha_g} - a_p\right]$ (9)

Case 3: $\Phi_T = 2\Phi_{pg}(h) + \Phi_{ps}\left[\sqrt{\left(h + a_p + a_g\right)^2 + {a_g}^2} - a_p\right]$

Case 4: $\Phi_T = 2\Phi_{pg}(h) + 2\Phi_{ps}\left[\sqrt{\left(a_p + a_g + h\right)^2 - {a_p}^2} - a_p\right]\ at\ a_g > \left(\sqrt{2} - 1\right)a_p$ (10)

$$\Phi_T = 2\Phi_{ps}(H) + 2\Phi_{pg}\left[\sqrt{\left(a_p + H\right)^2 + {a_p}^2} - a_p - a_g\right]\ at\ a_g \leq \left(\sqrt{2} - 1\right)a_p \quad (11)$$

Case 5: $\Phi_T = 4\Phi_{pg}(h) + \Phi_{ps}\left[\sqrt{\left(h + a_p\right)^2 + 2ha_g} - a_p\right]$ (12)

Note that derivations of the above equations can be found in Shen et al. (2012)[25].

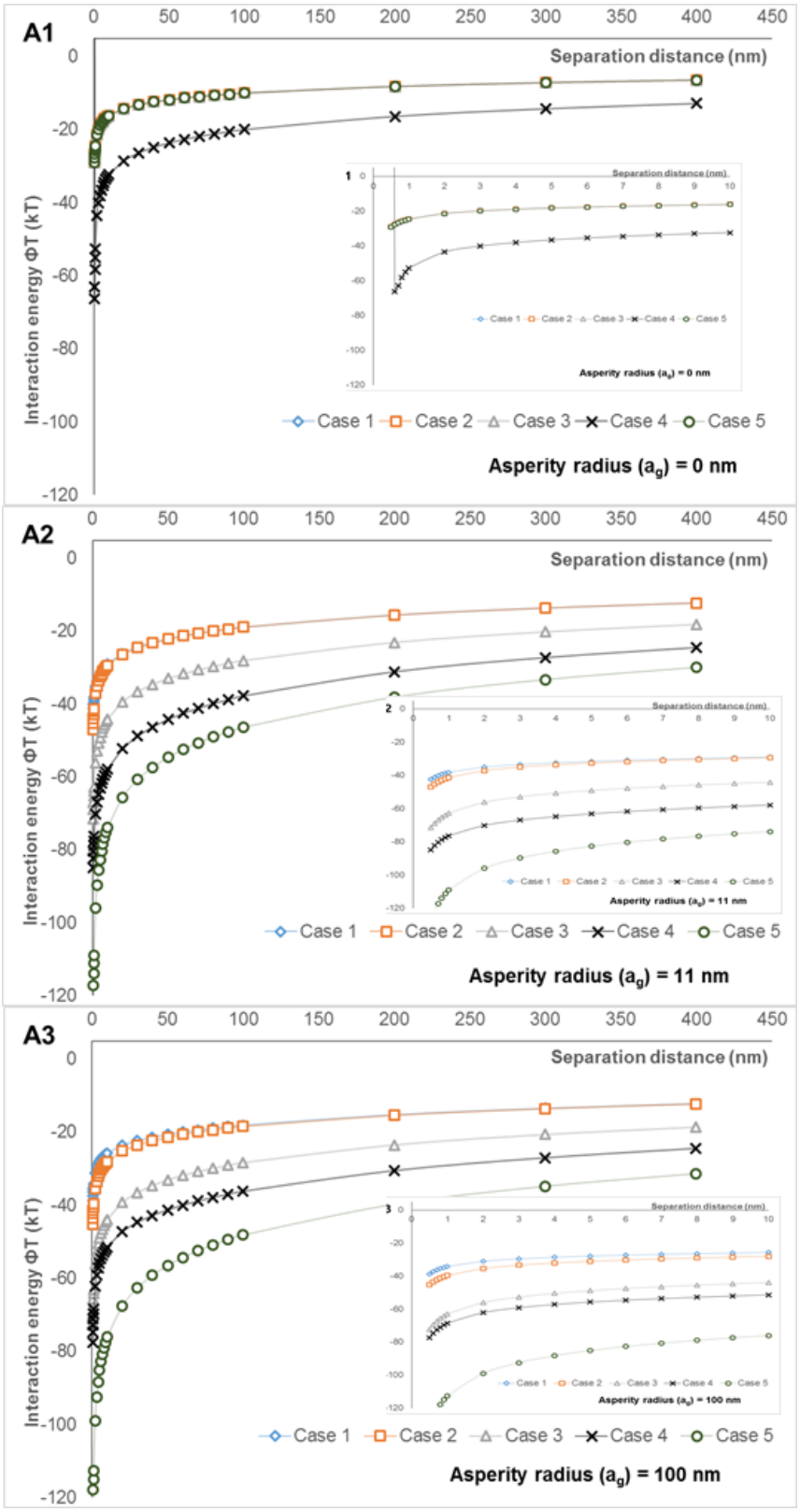

Figure 4.2. Calculated extended DLVO energy curves for interactions between MnO_x(s) colloids and rough media surfaces on glass media for configurations per figure 4.1 with different asperity radii along the z-axis at 0.002M ionic strength for 2 nm colloids.

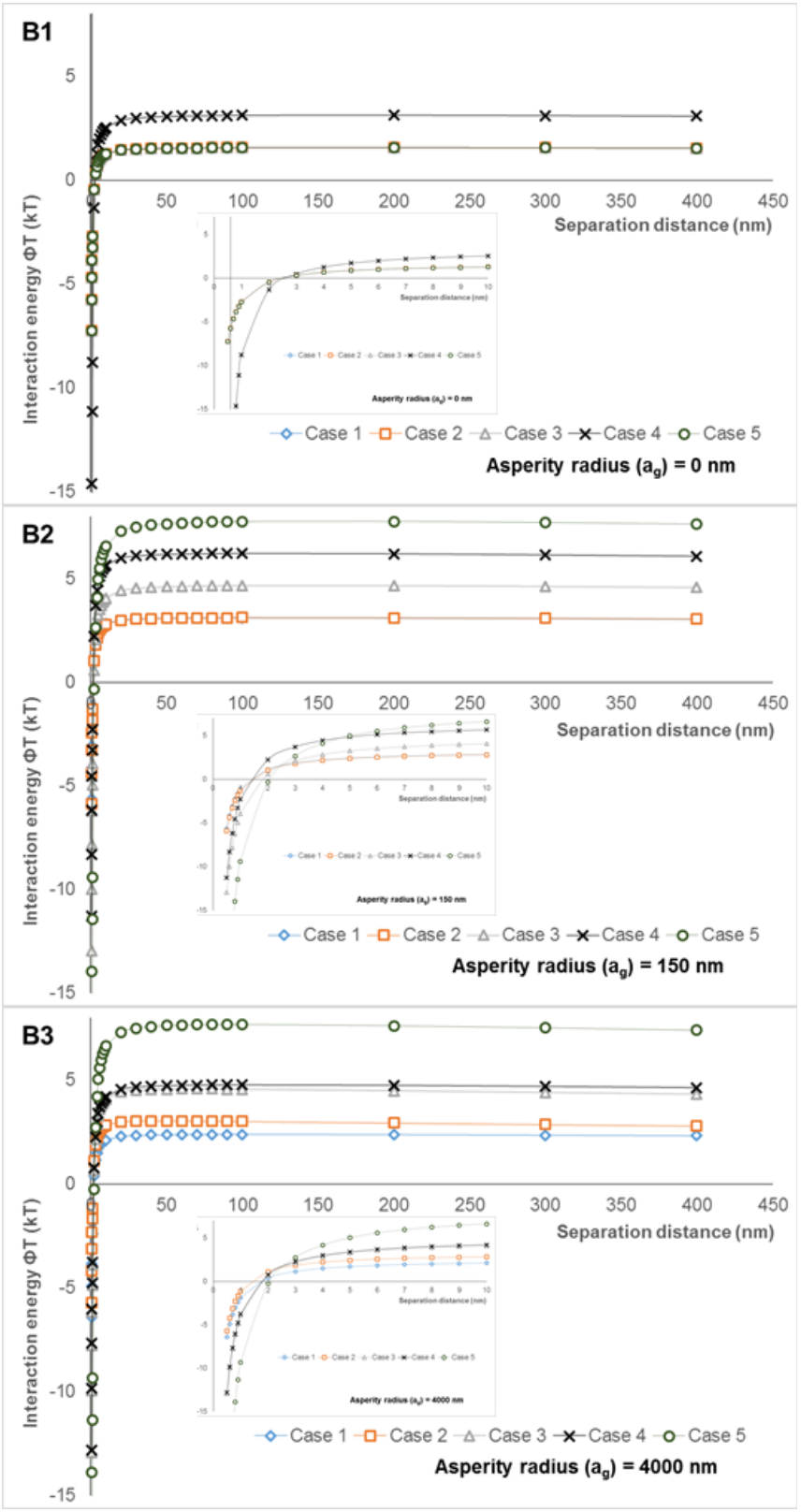

Figure 4.3. Calculated extended DLVO energy curves for interactions between MnO_x(s) colloids and rough media surfaces on sand media for configurations per figure 4.1 with different asperity radii along the z-axis at 0.002M ionic strength for 2 nm colloids.

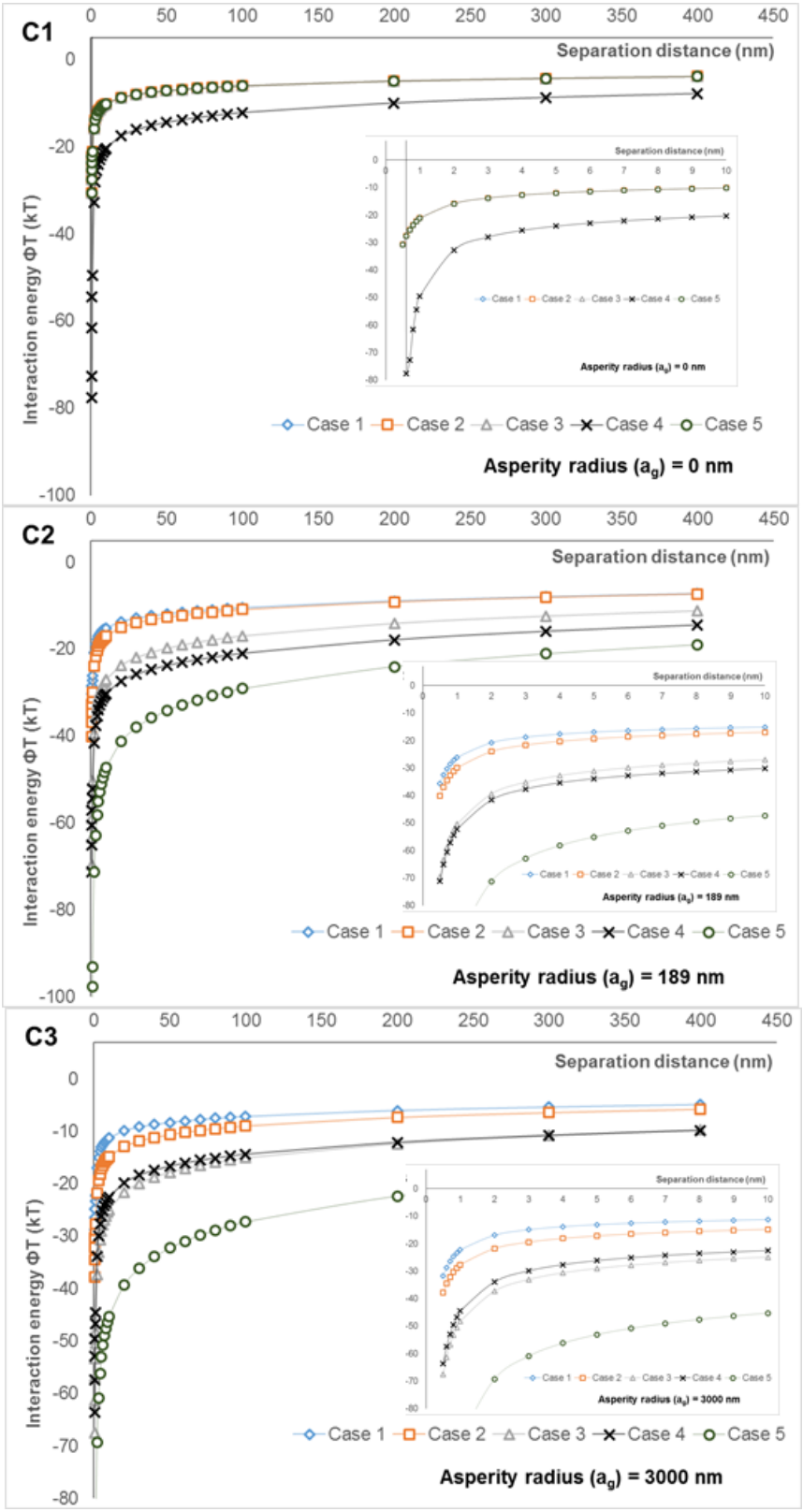

Figure 4.4. Calculated extended DLVO energy curves for interactions between MnO_x(s) colloids and rough media surfaces on alumina media for configurations per figure 4.1 with different asperity radii along the z-axis at 0.002M ionic strength for 2 nm colloids.

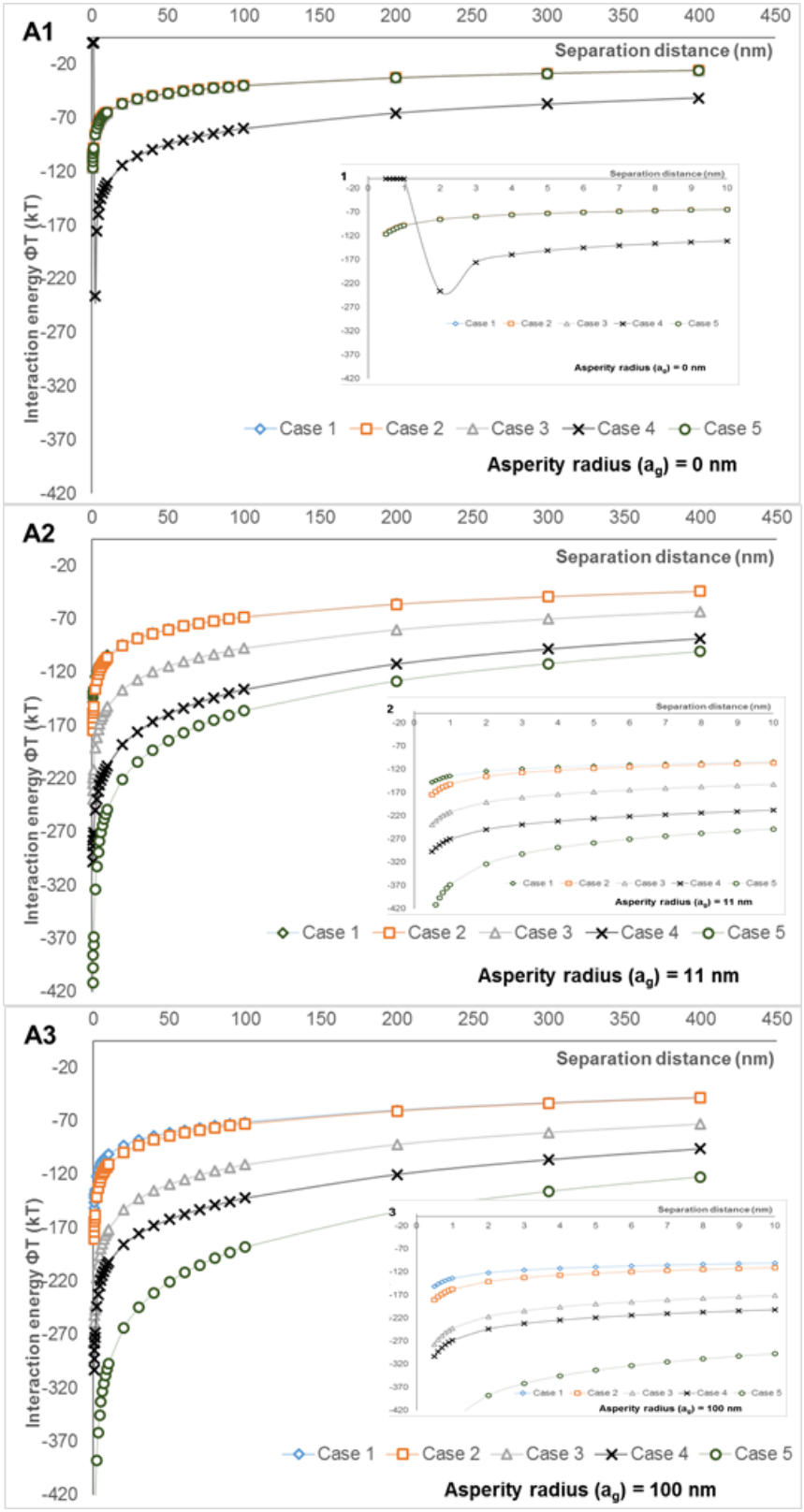

Figure 4.5. Calculated extended DLVO energy curves for interactions between MnO_x(s) colloids and rough media surfaces on glass media for configurations per figure 4.1 with different asperity radii along the z-axis at 0.002M ionic strength for 8 nm colloids.

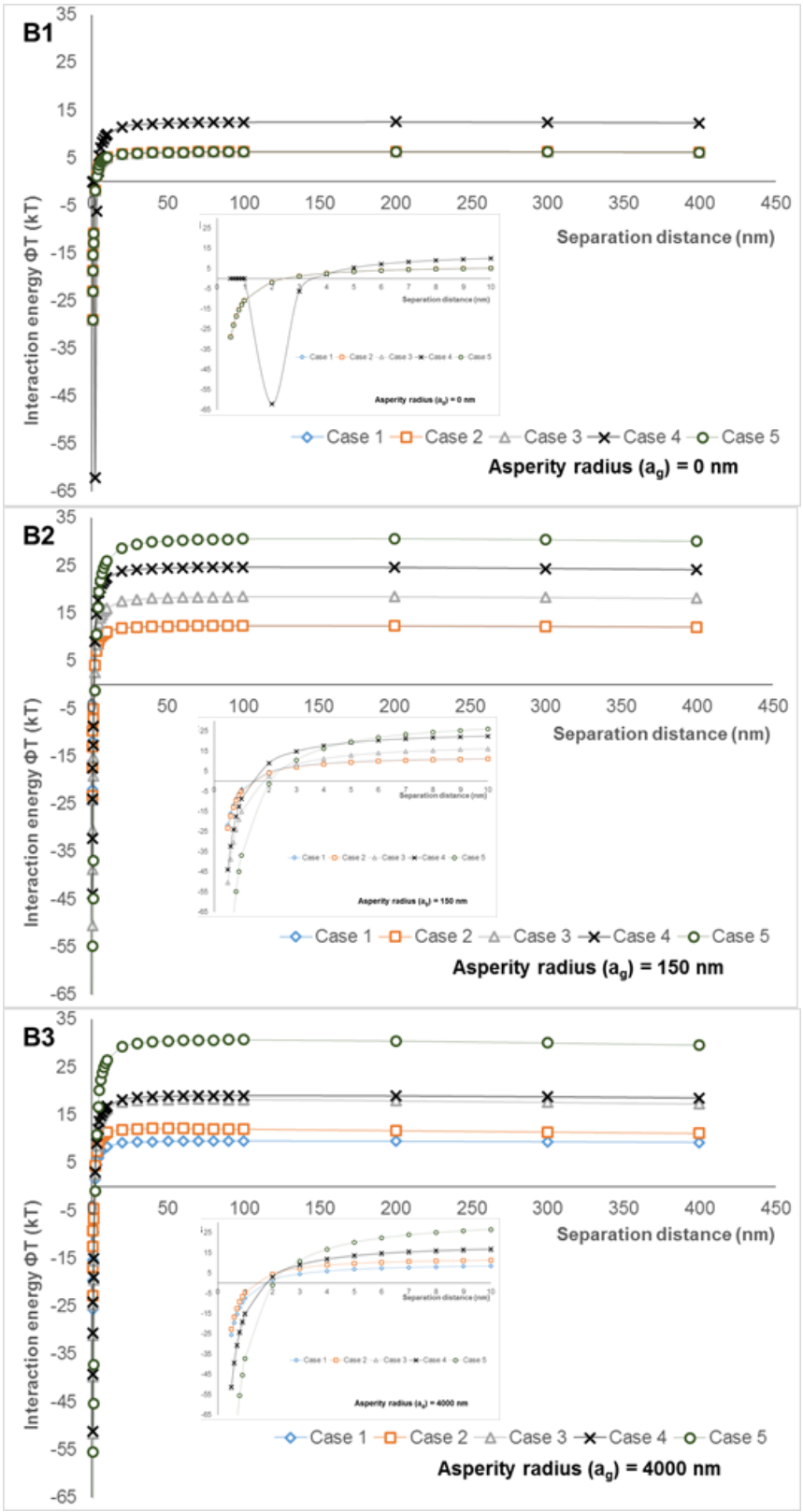

Figure 4.6. Calculated extended DLVO energy curves for interactions between MnO_x(s) colloids and rough media surfaces on sand media for configurations per figure 4.1 with different asperity radii along the z-axis at 0.002M ionic strength for 8 nm colloids.

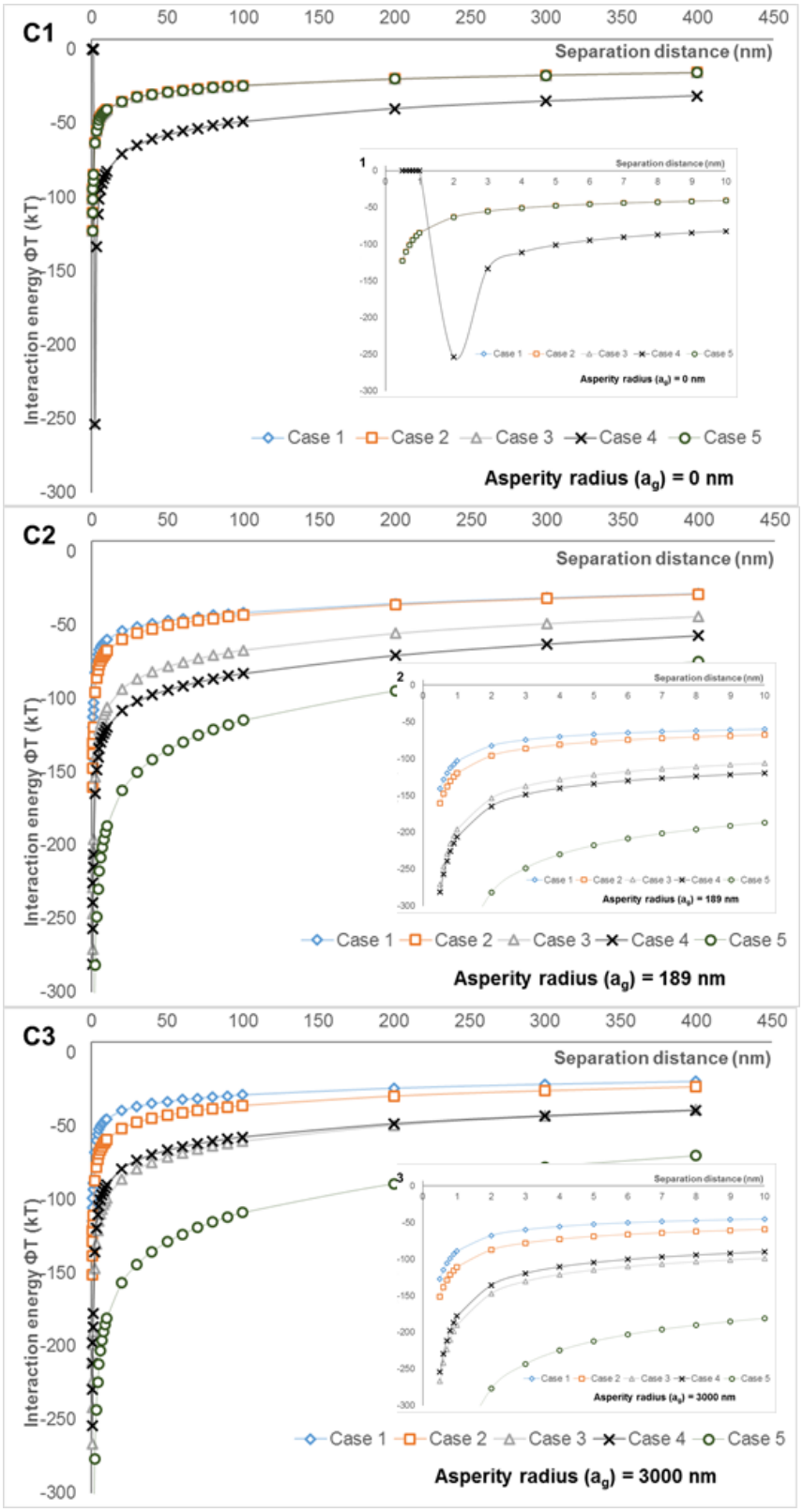

Figure 4.7. Calculated extended DLVO energy curves for interactions between MnO_x(s) colloids and rough media surfaces on alumina media for configurations per figure 4.1 with different asperity radii along the z-axis at 0.002M ionic strength for 8 nm colloids.

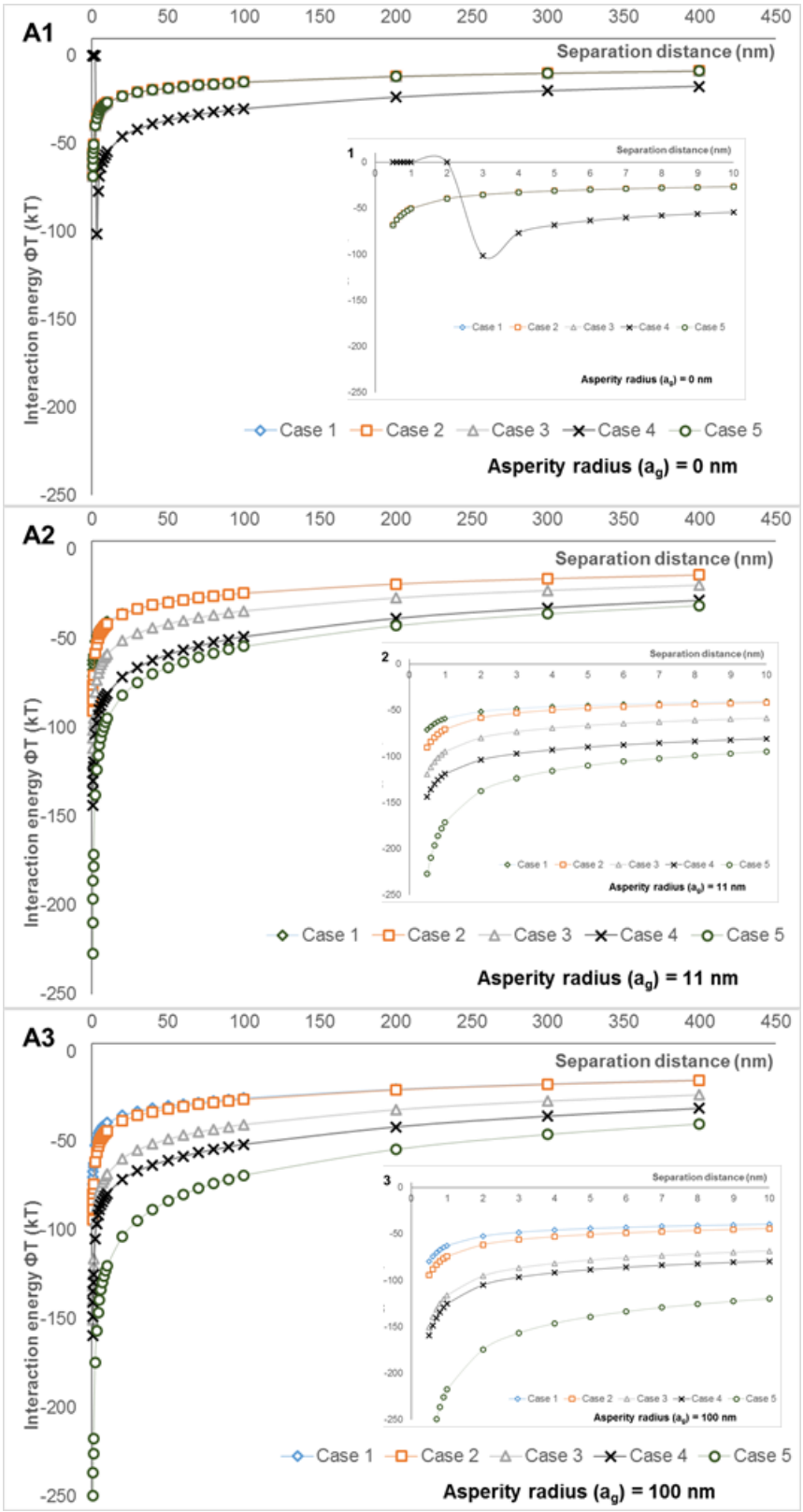

Figure 4.8. Calculated extended DLVO energy curves for interactions between a 11 nm cluster of MnO_x(s) and $Al(OH)_3$ colloids and rough media surfaces on glass media for configurations per figure 4.1 with different asperity radii along the z-axis at 0.002M ionic strength.

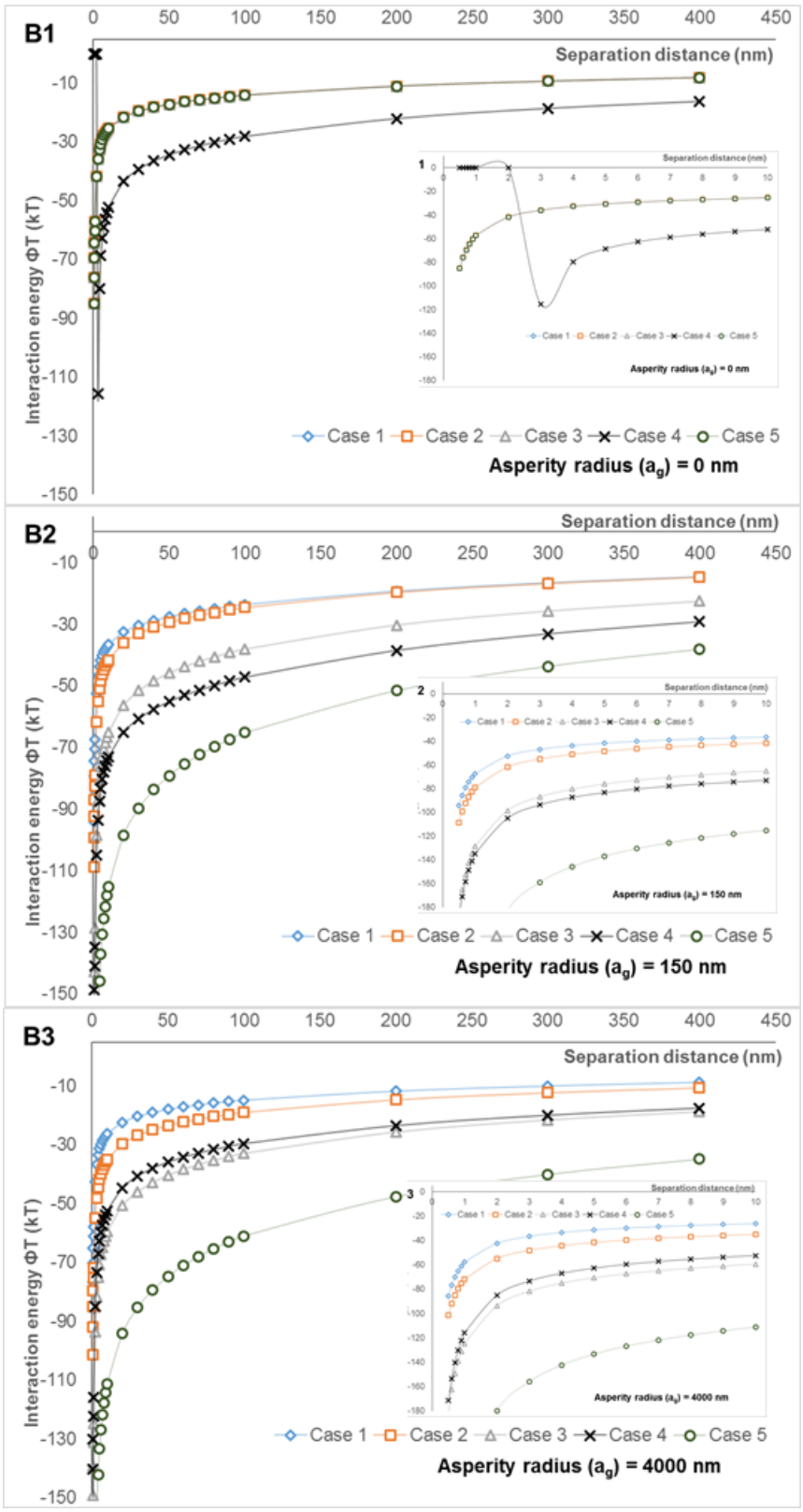

Figure 4.9. Calculated extended DLVO energy curves for interactions between a 11 nm cluster of MnO_x(s) and $Al(OH)_3$ colloids and rough media surfaces on sand media for configurations per figure 4.1 with different asperity radii along the z-axis at 0.002M ionic strength.

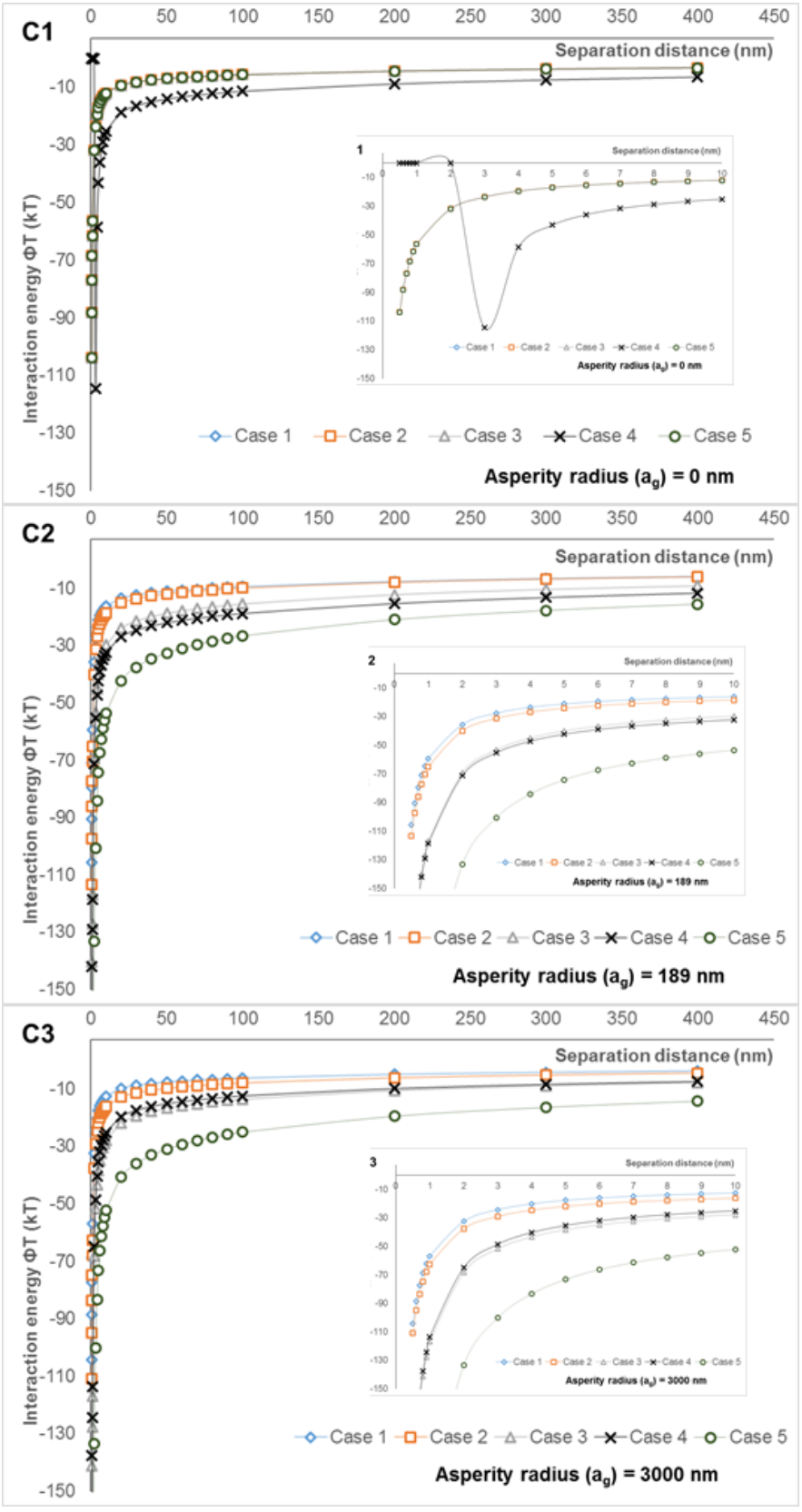

Figure 4.10. Calculated extended DLVO energy curves for interactions between a 11 nm cluster of MnO_x(s) and $Al(OH)_3$ colloids and rough media surfaces on alumina media for configurations per figure 4.1 with different asperity radii along the z-axis at 0.002M ionic strength.

Calculated interaction energy curves for the experimental conditions used in the column tests with colloidal particles of 2 nm, 8 nm, and a charge-neutralized cluster of colloidal particles of 11 nm in diameter are presented in figures 4.2 through 4.10. Favorable conditions for colloidal particles attachment are established when colloidal particles are oppositely-charged with respect to collector/filter media surface and thus particles are going to be always attracted to the collector/filter media surface. When the interaction energy becomes a large negative value, it indicates a stronger attachment. Unfavorable conditions for colloidal particles attachment exist when colloidal particles are like-charged with respect to collector/filter media surface. Colloidal particles are first repelled from the collector/filter media surface and, after a maximum energy barrier is surpassed, they are going to be attracted to the surface (see Figure 1.1 in chapter 1). Under the unfavorable conditions, however, a particle could still conquer the maximum energy barrier and attach to the surface when this repulsion energy became smaller. In particular, if the maximum energy barrier is comparable with the kinetic energy of Brownian motion, 1.5 kT, particle's movement is governed by the Brownian motion. In this case, both the particle attachment and detachment to the surface would be possible. According to Tadros, T (2007)[83], the maximum energy barrier should be less than 25kT for a particle to become attached to a surface. In general, this is a possible condition when a low zeta potential (below 40 mV) and high electrolyte concentration (above 10^{-2} M (mol dm^{-3}) 1:1 electrolyte) are achieved.

Based on the above definitions and the calculated results, the favorable conditions for MnO_x(s) colloidal particles are always observed in glass and alumina media (especially in A2 in figure 4.5 and C3 in figure 4.7) with the preferred attachment location of case 5 (valley/crevice formed by 4 contiguous asperities/protrusions). Note that the difference in the maximum energy barrier is about 10kT between A2 and A3 (figure 4.5), as well as between C2 and C3 (figure 4.7). 10 kT is significant enough since just a few kT units determines whether a particle will attach to a surface or will be destabilized. For example, when a secondary minimum exists in a particle-

surface interaction energy curve, its depth is usually between 1 and 5 kT. This secondary minimum determines a range of the particle-surface separation distance where reversible attachment occurs (figure 1.1 in Chapter 1).

In silica sand media, the unfavorable conditions for MnO_x(s) colloidal particles attachment always take place in the absence of Al (B1-3 in figure 4.6) because the interaction energy curve shows an energy barrier. Since energy barriers for these curves are low and relatively near the average Brownian kinetic energy (1.5 kT) in the majority of these cases, a reversible attachment of colloidal particles most likely occurs by Brownian diffusion. In this case, colloidal particles are more likely to be first attracted to the top or sides of asperities (case 1 and case 2 in B2 in figure 4.6). At the same time, particle detachment would also happen due to a hydrodynamic shear flow. However, the interaction energy curves in figure 4.6 B2 indicate that colloidal particles -after becoming close enough to the surface- could be then attached to the case 5 location. They would not be removed again (irreversible attachment) when particles approach that location and the separation distances become less than 2.0 nm. In addition, these concave areas (valleys/crevices) supported the attachment by shielding the particles from shear flow. Characterization data, especially SEM images in Figure 2.20 and Figure 4.12, strongly corroborate these results. These above-mentioned effects correspond directly to the characteristics (chemistry and structure) of each type of media.

When Al is present in the solution, favorable conditions for MnO_x(s) colloidal particles attachment are always observed in the calculated interaction energy curves. Destabilization of particles due to charge neutralization reduces the repulsion effect with respect to collector/filter media surface. In addition, aggregation of particles also takes place increasing the van der Waals attraction. Consequently, energy barriers for these curves are eliminated and thus particles are going to be always attracted to the collector/filter media surface.

In general, the interaction energies become more negative or the maximum energy barriers become smaller when the Hamaker constant increases and/or the colloidal particles size increases. For this exercise, the Hamaker constant depends on the filter media material and colloidal nanoparticles, since medium is the same. Due to the lack of knowledge regarding relative phase distribution in colloidal particles, a general MnO_x(s) Hamaker constant for all colloids was used, obtained from Zhu et al. (2011)[79]. For favorable conditions for attachment, the interaction energy curves become more negative until they reached a critical asperity size, after which the curves start to become less negative. For unfavorable conditions, the opposite behavior is observed. The maximum energy barrier start to increase until a critical asperity size is achieved, after which the maximum energy barrier start to decrease.

4.2.2 Microstructure

By using Atomic Force Microscopy (AFM) (figure 4.11), differences in morphology and topography of fresh media surface were observed. Fresh glass media presented asperities in the order of a few tens of nanometers with height differences (due to pits or craters on the surface) of about a hundred nanometers. Fresh alumina media showed differences in their surfaces varying in asperities distribution and protrusion height generally in the order of 1-3 micrometers because the alumina media was manufactured by powder sintering (Christy® Catalytics, Saint Louis, MO). Alumina media showed some areas of faceted features that were also observed in Scanning Electron Microscopy (SEM). Finally, fresh silica sand media has an intricate morphology of surface protrusions with larger height differences in the order of 1-4 micrometers combined with asperities of hundreds of nanometers.

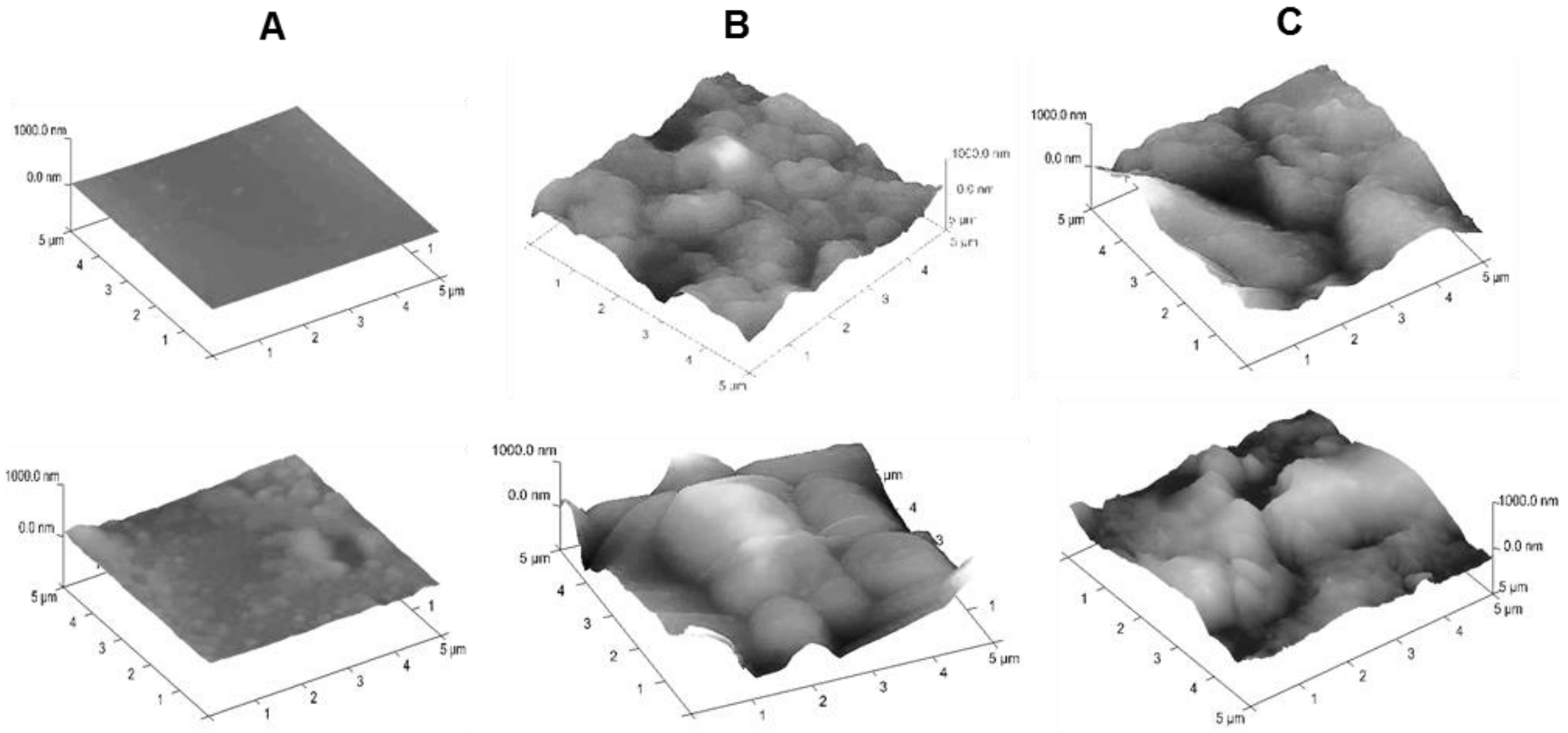

Figure 4.11. AFM images showing differences in typical topography of fresh glass beads, alumina spheres, and silica sand. A) Glass beads: the majority of the surface is smooth –top image-. Small concave defects -pits or craters- are also present on the surface –bottom image-. B) Alumina spheres: since these media are produced by sintering powder which coarsens through time, differences in surface morphology and topography are important. Height differences in features are appreciable on the surface, resembling aggregation of particles. C) Silica sand: larger height differences in features are observed with an intricate network of protrusions on the surface.

In table 4.1, typical arithmetic mean values of surface roughness (Ra) are presented for fresh and coated media. Ra value is the arithmetic average of the absolute value of the surface height deviations measured from the mean plane (Veeco Instruments Inc., 2004)[84]. The mean plane is calculated for the acquired raw data automatically by the NanoScope software following the ASME B46.1 and ISO 4287/4288 metrological standards (Veeco Instruments Inc., 2004)[84]. The NanoScope software then calculated the Ra values using the following formula:

$$R_a = \frac{1}{N}\sum_{j=1}^{N}|Z_j|$$

Where N = the number of measured points within a given area and Z_j = the absolute value of the surface height deviation measured from the mean plane.

Differences in surface roughness (increase or decrease) from identical filter media indicated that the coating formation was effectively occurring. For Mn–only and Mn-Al coated glass, and Mn-only coated alumina, the roughness increased with coating. Meanwhile, for Mn-Al coated alumina, and Mn-only and Mn-Al coated silica sand, the roughness decreased with coating. This trend explains the proposal of a preferred coating formation location: coating would start to form preferentially on concave areas of the filter media surface (valleys and crevices, especially). Smoother surfaces showed an increased number of asperities, as well as asperity size and/or morphology changes due to coating growth. Rough surfaces showed decreased protrusion (asperity) height differences due to coating formation on valleys and cavities (crevices) on the surface. In all cases, coating formed as a continuous network with a characteristic morphology (honeycomb-like morphology) as shown in SEM images (figures 2.14 through 2.20, and 3.9).

Table 4.1. Typical arithmetic mean value of surface roughness (Ra) of fresh filter media measured on different surface locations. As a comparison, measurements of identical, but coated media are also presented. Values are in nanometers (nm) and shows arithmetic mean ± standard deviation of three measurements.

Location	Fresh media	Mn-only coating (sixth day)	Mn-Al coating (sixth day)
Smoother glass surface	5±4	11±9	28±17
Pits or craters in glass surface	17±5	64±15	102±14
Low coarsened alumina surface	140±8	N/A	N/A
Medium coarsened alumina surface	181±4	N/A	N/A
High coarsened alumina surface	246±31	N/A	N/A
All alumina surfaces*	189±49	209±55	145±112
Sand surface	150±14	113±18	106±18

*Values computed with respect to all alumina surfaces.

In figure 4.12, a representative SEM micrograph shows a concave rough area on glass media covered with a large quantity of particles of Mn-Al coating, near a smooth and higher area. The location of coating particles correlated well with concave rough surfaces. Usually, a higher density of particles was observed in concave areas (valleys, craters, etc.) located between or next to large asperities.

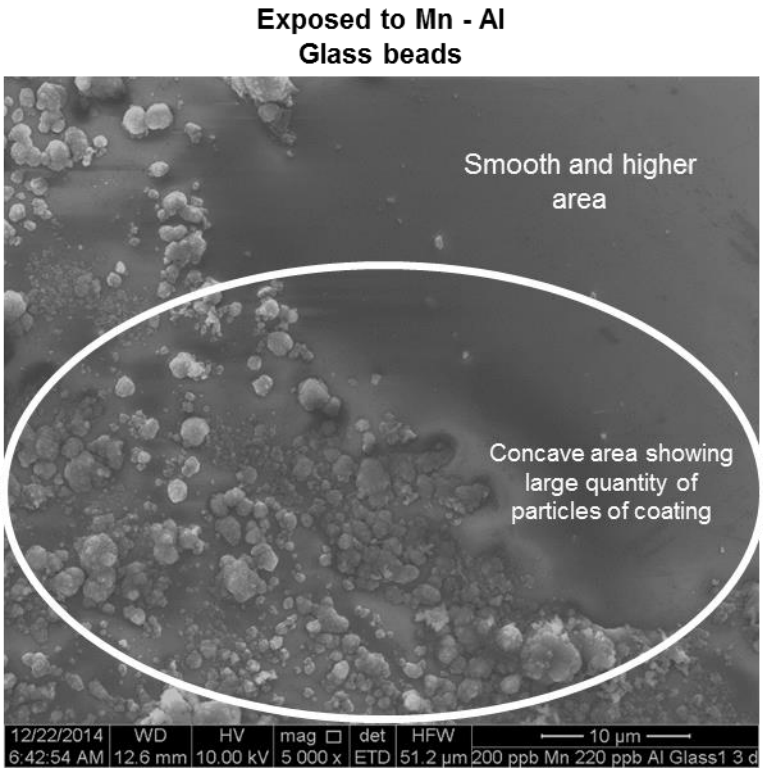

Figure 4.12. Concave rough area on top of glass media exposed to Mn–Al solution showing large quantity of coating particles.

4.3. Discussion

In figure 4.3 and 4.6, energy barriers in unfavorable conditions do not disappear and colloidal particle attachment is still hindered (B1 through B3). Nonetheless, the maximum energy barrier can still be overcome due to the relative small value (around 7kT and 30kT respectively). All other calculated energy curves present favorable conditions with a preferred attachment location in valleys/crevices. When suspension is moving or a shear flow system is created, asperities can shield colloids from hydrodynamic shear[85]. The shielding effect provided by asperities can be referred to as the wall effect. Particle attachment took place in concave areas near asperities where tangential adhesive forces develop, preventing colloids from being dragged away (figure 4.12). On the other hand, the favorable conditions curves suggest that homogeneous coating formation should occur. However, this condition is not observed due to shear flow

dragging away unshielded colloids. SEM images (figure 2.20 and figure 4.12) demonstrate that the irreversible attachment in the primary minima on top of asperities is not happening. These observations support the predictions of the rough surface model in shear flow systems. Also, despite the different chemical characteristics and crystallinity of each media type changing the shape of the interaction curves, a similar coating development behavior is observed. This indicates that elemental chemistry and crystallinity of filter media impact to a lesser extent the initial MnO_x(s) coating formation and Mn uptake processes. In contrary, the presence of Al in the solution enhances these phenomena -initial MnO_x(s) coating formation and Mn removal from water- by always providing favorable conditions for particle attachment in addition to particle destabilization and aggregation regardless filter media used.

According to Amirtharajah (1988)[17], Al species in water mainly neutralize surface charge, destabilizing and aggregating MnO_x(s) colloidal particles at the experimental pH of 7.3. These colloidal particles experiment decreased interaction energies with collector/filter media due to the reduction of the electrical double layer potential. On the other hand, destabilization and aggregation permit to form a larger cluster of colloidal particles, which promotes increased attraction to collector/filter media mainly due to the van der Waals component of the interaction energy. This indicates that aggregation of particles and deposition are enhanced in the proximity of collector/filter media surface due to combination of these effects. When colloids are located at large separation distances, interaction energies with respect to collector/filter media are largely reduced. Consequently, colloidal particle aggregation mainly occurs, forming intermixed clusters of colloidal MnO_x(s) and Al species. These latter species are simultaneously precipitating and coating colloidal particles. These larger clusters will then be deposited on the surface of filter media. This can explain the different growth morphology of coatings at initial stages in the absence and presence of Al (film growth versus island growth, respectively) as observed in figures 2.14 to 2.20 in chapter 2. Moreover, when aggregates of particles are deposited on and attached

to the filter media, a condition of rougher surface is created enhancing the colloidal particle removal.

Since colloid attachment is limited to the availability of concave sites and their size, this process ends with time due to a preferential growth of coating on these locations. Therefore, other mechanisms should have taken place for developing further these coatings, for example, the attachment in the primary minimum by surface charge heterogeneity and the autocatalytic redox reactions on the surface. Based on the time-resolved observations in chapter 2 (figures 2.19 and 2.20), it is suggested that an autocatalytic redox reaction is occurring on the surface of coating in combination with a precipitation and growth process, which could include sorption to develop coatings further. As observed by Junta-Rosso et al. (1997)[15], heterogeneous oxidation reactions will be promoted on the rough surfaces (defects, step-edges, etc.) due to changes in the local environment conditions (concentration, pH, etc.). Jinkeun et al. (2006)[70], also supports the hypothesis of localized changes of environmental conditions near surface due to roughness through their analysis of zeta potential distributions on filter media. Both studies confirm that areas of concave defects and around protrusions are actively promoting the formation of poorly crystalline birnessite by redox reaction. In this study, coating evolution images (figures 2.19 and 2.20) showed precipitates growing outwards from these locations, constituting strong support for the hypothesis mentioned above.

CHAPTER 5. Conclusions and suggestions for future work

5.1. Conclusions

- Among the three main characteristics of media analyzed, micrometer scale surface topography and elemental chemistry are demonstrated to be the most influential parameters in the process of the initial formation of $MnO_{x(s)}$ coating layer and in the removal of soluble Mn from water.
    - Results demonstrate that initial coating preferentially form on concave areas (valleys, crevices and around protrusions). After that, coating grows first two-dimensionally parallel to the surface of the substrate (filter media or bayerite), and then stacks one layer on top of another. When time elapsed, coating connect to each other developing networks/films.
    - Elemental chemistry of media determines the phases formed in the system (coating and suspended solids).
    - Crystallinity of media did not show a role on the coating formation process.
- Presence of Al in water enhances soluble Mn removal capacity, promotes formation of a more catalytically active phase of $MnO_x(s)$ –delta birnessite-, increases content of suspended solids, and produces non-uniform distribution of coatings (“patchy” features).
- Delta and hexagonal birnessites are the major phases present in the $MnO_x(s)$ coatings, explaining the catalytically active behavior of coating in oxidizing soluble Mn and in capturing other contaminants from water. Hausmannite, Bayerite and a manganite-like amorphous phase are identified as minor phases.

- The rough surface model is proven to yield good approximations in predicting location of the first manganese-bearing deposits on the filter media. Our observations support the theoretical evaluation of this model on interactions between spherical MnO_x(s) nanoparticles and rough surfaces using a modified/extended DLVO theory.
- A coating growth model has been proposed, which suggests that poorly crystallized nanoparticles form in solution yielding a different birnessite (delta or hexagonal) phase depending on the solution chemistry. This birnessite in turn forms and precipitates more birnessite and simultaneously produces the metastable phase feitknechtite. Then, feitknechtite -when exposed to soluble Mn- transforms to hausmannite (pH 8.0- 8.5) or to a manganite-like material (pH 7.0- 8.0).
- Most likely, a combination of the rough surface model with the geometric one could better predict the capture and oxidation of soluble Mn by porous filters, providing a comprehensive model with improved accuracy.

5.2. Future work

Certainly, further research needs to be performed in order to provide insights regarding the formation mechanism(s) of MnO_x(s) nanoparticles in solution observed in TEM micrographs. At this time, it can only be hypothesized that a rapid localized heterogeneous oxidation of Mn (II) by free chlorine is occurring prefilter which forms precursors of MnO_x(s) that potentially self-assemble, and ultimately create the birnessite nanoparticles observed.

In addition, explaining how Al promotes the delta birnessite formation would also deem important to further improve the removal of soluble Mn from water. Moreover, it would be interesting to investigate if birnessite phases evolve with time (δ-birnessite → hexagonal-birnessite → triclinic-birnessite) in controlled experiments under the same conditions of the column tests, since this could provide insights regarding coating behavior with time and the evolution of its properties.

References

1. Gabelich, C. J.; Gerringer, F. W.; Knocke, W. R.; Lee, C. C., Sequential Manganese Desorption and Sequestration in Anthracite Coal and Silica Sand Filter Media. *Journal (American Water Works Association)* **2006,** *98*, (5), 116-127.
2. Carlson, K.; Knocke, W., Modeling Manganese Oxidation with KMnO4 for Drinking Water Treatment. *Journal of Environmental Engineering* **1999,** *125*, (10), 892-896.
3. Sly, L. I.; Hodgkinson, M. C.; Arunpairojana, V., Deposition of manganese in a drinking water distribution system. *Applied and Environmental Microbiology* **1990,** *56*, (3), 628-639.
4. Hargette, A.; Knocke, W., Assessment of Fate of Manganese in Oxide-Coated Filtration Systems. *Journal of Environmental Engineering* **2001,** *127*, (12), 1132-1138.
5. Sain, A. E. Aerosolization of Drinking Water Metals to Indoor Air and Assessment of Human Taste and Visual Thresholds for Manganese. Thesis, Virginia Polytechnic Institute and State University, Blacksburg, VA, 2013.
6. Coffey, B.; Gallagher, D.; Knocke, W., Modeling Soluble Manganese Removal by Oxide‐Coated Filter Media. *Journal of Environmental Engineering* **1993,** *119*, (4), 679-694.
7. Knocke, W. R.; Hamon, J. R.; Thompson, C. P., Soluble Manganese Removal on Oxide-Coated Filter Media. *Journal (American Water Works Association)* **1988,** *80*, (12), 65-70.
8. Knocke, W. R.; Occiano, S. C.; Hungate, R., Removal of Soluble Manganese by Oxide-coated Filter Media: Sorption Rate and Removal Mechanism Issues. *Journal (American Water Works Association)* **1991,** *83*, (8), 64-69.
9. Tobiason, J. E.; Knocke, W. R.; Goodwill, J. E.; Islam, A. A.; Hargette, P.; Bouchard, R.; Zuravnsky, L. *Characterization and Performance of Filter Media for Manganese Control*; Denver, Colorado, 2008.
10. Merkle, P.; Knocke, W.; Gallagher, D.; Little, J., Dynamic Model for Soluble Mn2+ Removal by Oxide-Coated Filter Media. *Journal of Environmental Engineering* **1997,** *123*, (7), 650-658.
11. Knocke, W. R.; Benschoten, J. E. V.; Kearney, M. J.; Soborski, A. W.; Reckhow, D. A., Kinetics of Manganese and Iron Oxidation by Potassium Permanganate and Chlorine Dioxide. *Journal (American Water Works Association)* **1991,** *83*, (6), 80-87.
12. Nakanishi, H., Kinetics of continuous removal of manganese in a Mn02-coated sand bed. *Kogyo Kagaku Zasshi, Japan* **1967,** *70*, (4), 407-410.
13. Davies, S. H. R.; Morgan, J. J., Manganese(II) oxidation kinetics on metal oxide surfaces. *Journal of Colloid and Interface Science* **1989,** *129*, (1), 63-77.
14. Hao, O.; Davis, A.; Chang, P., Kinetics of Manganese(II) Oxidation with Chlorine. *Journal of Environmental Engineering* **1991,** *117*, (3), 359-374.
15. Junta-Rosso, J. L.; Hochella Jr, M. F.; Donald Rimstidt, J., Linking microscopic and macroscopic data for heterogeneous reactions illustrated by the oxidation of manganese (II) at mineral surfaces. *Geochimica et Cosmochimica Acta* **1997,** *61*, (1), 149-159.
16. Knocke, W. R.; Hoehn, R. C.; Sinsabaugh, R. L., Using Alternative Oxidants to Remove Dissolved Manganese From Waters Laden With Organics. *Journal (American Water Works Association)* **1987,** *79*, (3), 75-79.
17. Amirtharajah, A., Some Theoretical and Conceptual Views of Filtration. *Journal (American Water Works Association)* **1988,** *80*, (12), 36-46.

18. Petosa, A. R.; Jaisi, D. P.; Quevedo, I. R.; Elimelech, M.; Tufenkji, N., Aggregation and Deposition of Engineered Nanomaterials in Aquatic Environments: Role of Physicochemical Interactions. *Environmental science & technology* **2010,** *44*, (17), 6532-6549.
19. Saiers, J. E.; Ryan, J. N., Colloid deposition on non-ideal porous media: The influences of collector shape and roughness on the single-collector efficiency. *Geophysical Research Letters* **2005,** *32*, (21), L21406.
20. Bhattacharjee, S.; Ko, C.-H.; Elimelech, M., DLVO Interaction between Rough Surfaces. *Langmuir* **1998,** *14*, (12), 3365-3375.
21. Hem, J. D., Rates of manganese oxidation in aqueous systems. *Geochimica et Cosmochimica Acta* **1981,** *45*, (8), 1369-1374.
22. Hem, J. D.; Lind, C. J., Nonequilibrium models for predicting forms of precipitated manganese oxides. *Geochimica et Cosmochimica Acta* **1983,** *47*, (11), 2037-2046.
23. Murray, J. W.; Dillard, J. G.; Giovanoli, R.; Moers, H.; Stumm, W., Oxidation of Mn(II): Initial mineralogy, oxidation state and ageing. *Geochimica et Cosmochimica Acta* **1985,** *49*, (2), 463-470.
24. Wilson, D. E., Surface and complexation effects on the rate of Mn(II) oxidation in natural waters. *Geochimica et Cosmochimica Acta* **1980,** *44*, (9), 1311-1317.
25. Shen, C.; Wang, L.-P.; Li, B.; Huang, Y.; Jin, Y., Role of Surface Roughness in Chemical Detachment of Colloids Deposited at Primary Energy Minima. *Vadose Zone Journal* **2012,** *11*, (1).
26. Bradford, S. A.; Torkzaban, S., Colloid Interaction Energies for Physically and Chemically Heterogeneous Porous Media. *Langmuir* **2013,** *29*, (11), 3668-3676.
27. Elimelech, M.; Xiaohua, Z.; Childress, A. E.; Seungkwan, H., Role of membrane surface morphology in colloidal fouling of cellulose acetate and composite aromatic polyamide reverse osmosis membranes. *Journal of Membrane Science* **1997,** *127*, (1), 101-109.
28. Merkle, P. B.; Knocke, W.; Gallagher, D.; Junta-Rosso, J.; Solberg, T., Characterizing filter media mineral coatings. *Journal (American Water Works Association)* **1996,** *88*, (12), 62-73.
29. Birkner, N.; Navrotsky, A., Thermodynamics of manganese oxides: Effects of particle size and hydration on oxidation-reduction equilibria among hausmannite, bixbyite, and pyrolusite. *American Mineralogist* **2012,** *97*, (8-9), 1291-1298.
30. Bricker, O., Some stability relations in system Mn-O2-H2O at 25 degrees and 1 atmosphere total pressure. *American Mineralogist* **1965,** *50*, (9), 1296-1354.
31. Zhu, M.; Farrow, C. L.; Post, J. E.; Livi, K. J. T.; Billinge, S. J. L.; Ginder-Vogel, M.; Sparks, D. L., Structural study of biotic and abiotic poorly-crystalline manganese oxides using atomic pair distribution function analysis. *Geochimica et Cosmochimica Acta* **2012,** *81*, (0), 39-55.
32. Okazaki, M.; Sugita, T.; Shimizu, M.; Ohode, Y.; Iwamoto, K.; de Vrind-de Jong, E. W.; de Vrind, J. P.; Corstjens, P. L., Partial purification and characterization of manganese-oxidizing factors of Pseudomonas fluorescens GB-1. *Applied and Environmental Microbiology* **1997,** *63*, (12), 4793-4799.
33. Morgan, J. J.; Stumm, W., Analytical Chemistry of Aqueous Manganese. *Journal (American Water Works Association)* **1965,** *57*, (1), 107-119.
34. Brewer, P. G.; Spencer, D. W., COLORIMETRIC DETERMINATION OF MANGANESE IN ANOXIC WATERS1. *Limnology and Oceanography* **1971,** *16*, (1), 107-110.

35. Veeramani, H.; Aruguete, D.; Monsegue, N.; Murayama, M.; Dippon, U.; Kappler, A.; Hochella, M. F., Low-Temperature Green Synthesis of Multivalent Manganese Oxide Nanowires. *ACS Sustainable Chemistry & Engineering* **2013,** *1*, (9), 1070-1074.
36. Han, R.; Zou, W.; Zhang, Z.; Shi, J.; Yang, J., Removal of copper(II) and lead(II) from aqueous solution by manganese oxide coated sand: I. Characterization and kinetic study. *Journal of Hazardous Materials* **2006,** *137*, (1), 384-395.
37. Cerrato, J. M.; Knocke, W. R.; Hochella, M. F.; Dietrich, A. M.; Jones, A.; Cromer, T. F., Application of XPS and Solution Chemistry Analyses to Investigate Soluble Manganese Removal by MnO_x(s)-Coated Media. *Environmental science & technology* **2011,** *45*, (23), 10068-10074.
38. Junta, J. L.; Hochella Jr, M. F., Manganese (II) oxidation at mineral surfaces: A microscopic and spectroscopic study. *Geochimica et Cosmochimica Acta* **1994,** *58*, (22), 4985-4999.
39. Nesbitt, H.; Banerjee, D., Interpretation of XPS Mn (2p) spectra of Mn oxyhydroxides and constraints on the mechanism of MnO2 precipitation. *American Mineralogist* **1998,** *83*, (3), 305-315.
40. Sahabi, D. M.; Takeda, M.; Suzuki, I.; Koizumi, J.-i., Removal of Mn2+ from water by "aged" biofilter media: The role of catalytic oxides layers. *Journal of Bioscience and Bioengineering* **2009,** *107*, (2), 151-157.
41. Hu, P.-Y.; Hsieh, Y.-H.; Chen, J.-C.; Chang, C.-Y., Characteristics of manganese-coated sand using SEM and EDAX analysis. *Journal of Colloid and Interface Science* **2004,** *272*, (2), 308-313.
42. O'Reilly, S. E.; Hochella Jr, M. F., Lead sorption efficiencies of natural and synthetic Mn and Fe-oxides. *Geochimica et Cosmochimica Acta* **2003,** *67*, (23), 4471-4487.
43. Kim, J.; Jung, S., SOLUBLE MANGANESE REMOVAL BY POROUS MEDIA FILTRATION. *Environmental Technology* **2008,** *29*, (12), 1265-1273.
44. Manceau, A.; Marcus, M. A.; Grangeon, S.; Lanson, M.; Lanson, B.; Gaillot, A.-C.; Skanthakumar, S.; Soderholm, L., Short-range and long-range order of phyllomanganate nanoparticles determined using high-energy X-ray scattering. *Journal of Applied Crystallography* **2013,** *46*, (1), 193-209.
45. Fendorf, S. E.; Sparks, D. L.; Fendorf, M.; Gronsky, R., Surface precipitation reactions on oxide surfaces. *Journal of Colloid and Interface Science* **1992,** *148*, (1), 295-298.
46. Villalobos, M.; Toner, B.; Bargar, J.; Sposito, G., Characterization of the manganese oxide produced by pseudomonas putida strain MnB1. *Geochimica et Cosmochimica Acta* **2003,** *67*, (14), 2649-2662.
47. Hinds, G. S. The Impact of Aluminum on the Initiation and Development of MnO_x(s) Coatings for Manganese Removal. Virginia Tech, 2015.
48. Chupas, P. J.; Qiu, X.; Hanson, J. C.; Lee, P. L.; Grey, C. P.; Billinge, S. J. L., Rapid-acquisition pair distribution function (RA-PDF) analysis. *Journal of Applied Crystallography* **2003,** *36*, (6), 1342-1347.
49. Hammersley, A. P.; Svensson, S. O.; Hanfland, M.; Fitch, A. N.; Hausermann, D., Two-dimensional detector software: From real detector to idealised image or two-theta scan. *High Pressure Research* **1996,** *14*, (4-6), 235-248.
50. Learman, D. R.; Wankel, S. D.; Webb, S. M.; Martinez, N.; Madden, A. S.; Hansel, C. M., Coupled biotic–abiotic Mn(II) oxidation pathway mediates the formation and structural evolution of biogenic Mn oxides. *Geochimica et Cosmochimica Acta* **2011,** *75*, (20), 6048-6063.

51. Post, J. E., Manganese oxide minerals: Crystal structures and economic and environmental significance. *Proceedings of the National Academy of Sciences* **1999,** *96*, (7), 3447-3454.
52. Christensen, A. N.; Ollivier, G., Hydrothermal preparation and low temperature magnetic properties of Mn(OH)2. *Solid State Communications* **1972,** *10*, (7), 609-614.
53. Balan, E.; Blanchard, M.; Hochepied, J.-F.; Lazzeri, M., Surface modes in the infrared spectrum of hydrous minerals: the OH stretching modes of bayerite. *Phys Chem Minerals* **2008,** *35*, (5), 279-285.
54. Langford, J. I.; Wilson, A. J. C., Scherrer after sixty years: A survey and some new results in the determination of crystallite size. *Journal of Applied Crystallography* **1978,** *11*, (2), 102-113.
55. Dadkhah, M.; Saboori, A.; Jafari, M., Investigating the Physical Properties of Sintered Alumina in the Presence of MgO Nanopowder. *Journal of Materials* **2014,** *2014*, 7.
56. Lefkowitz, J. P.; Rouff, A. A.; Elzinga, E. J., Influence of pH on the Reductive Transformation of Birnessite by Aqueous Mn(II). *Environmental science & technology* **2013,** *47*, (18), 10364-10371.
57. Elzinga, E. J., Reductive Transformation of Birnessite by Aqueous Mn(II). *Environmental science & technology* **2011,** *45*, (15), 6366-6372.
58. Brezonik, P. L.; Arnold, W. A., Water chemistry an introduction to the chemistry of natural and engineered aquatic systems. In Oxford University Press: New York, 2011.
59. Yang, D. S.; Wang, M. K., SYNTHESES AND CHARACTERIZATION OF BIRNESSITE BY OXIDIZING PYROCHROITE IN ALKALINE CONDITIONS. *Clays and Clay Minerals* **2002,** *50*, (1), 63-69.
60. Cornell, R.; Giovanoli, R., Transformation of hausmannite into birnessite in alkaline media. *Clays and Clay Minerals* **1988,** *36*, (3), 249-257.
61. Drits, V. A.; Silvester, E.; Gorshkov, A. I.; Manceau, A., Structure of synthetic monoclinic Na-rich birnessite and hexagonal birnessite .1. Results from X-ray diffraction and selected-area electron diffraction. *The American mineralogist* **1997,** *82*, (9-10), 946-961.
62. Silvester, E.; Manceau, A.; Drits, V. A., Structure of synthetic monoclinic Na-rich birnessite and hexagonal birnessite; II, Results from chemical studies and EXAFS spectroscopy. *American Mineralogist* **1997,** *82*, (9-10), 962-978.
63. Post, J. E.; Veblen, D. R., Crystal structure determinations of synthetic sodium, magnesium, and potassium birnessite using TEM and the Rietveld method. *The American mineralogist* **1990,** *75*, (5-6), 477.
64. Lanson, B.; Drits, V. A.; Feng, Q.; Manceau, A., Structure of synthetic Na-birnessite: Evidence for a triclinic one-layer unit cell. *American Mineralogist* **2002,** *87*, (11-12), 1662-1671.
65. Post, J. E.; Heaney, P. J.; Hanson, J., Rietveld refinement of a triclinic structure for synthetic Na-birnessite using synchrotron powder diffraction data. *Powder Diffraction* **2002,** *17*, (03), 218-221.
66. Webb, S. M.; Tebo, B. M.; Bargar, J. R., Structural characterization of biogenic Mn oxides produced in seawater by the marine bacillus sp. strain SG-1. *American Mineralogist* **2005,** *90*, (8-9), 1342-1357.
67. Santelli, C. M.; Webb, S. M.; Dohnalkova, A. C.; Hansel, C. M., Diversity of Mn oxides produced by Mn(II)-oxidizing fungi. *Geochimica et Cosmochimica Acta* **2011,** *75*, (10), 2762-2776.

68. Baron, V.; Gutzmer, J.; Rundlof, H.; Tellgren, R., The influence of iron substitution in the magnetic properties of hausmannite, Mn (super 2+) (Fe,Mn) (super 3+) 2 O 4. *American Mineralogist* **1998,** *83*, (7-8), 786-793.
69. Auerbach, S. M.; Carrado, K. A.; Dutta, P. K., *Handbook of layered materials*. M. Dekker: New York, 2004.
70. Jinkeun, K.; Nason, J. A.; Lawler, D. F., Zeta potential distributions in particle treatment processes. *Journal of Water Supply: Research & Technology-AQUA* **2006,** *55*, (7/8), 461-470.
71. Feng, X. H.; Zhu, M.; Ginder-Vogel, M.; Ni, C.; Parikh, S. J.; Sparks, D. L., Formation of nano-crystalline todorokite from biogenic Mn oxides. *Geochimica et Cosmochimica Acta* **2010,** *74*, (11), 3232-3245.
72. Tilak, A. S.; Ojewole, S.; Williford, C. W.; Fox, G. A.; Sobecki, T. M.; Larson, S. L., Formation of Manganese Oxide Coatings onto Sand for Adsorption of Trace Metals from Groundwater. *J. Environ. Qual.* **2013,** *42*, (6), 1743-1751.
73. Hahn, M. W.; Abadzic, D.; O'Melia, C. R., Aquasols: On the Role of Secondary Minima†. *Environmental science & technology* **2004,** *38*, (22), 5915-5924.
74. Hahn, M. W.; O'Melia, C. R., Deposition and Reentrainment of Brownian Particles in Porous Media under Unfavorable Chemical Conditions: Some Concepts and Applications. *Environmental science & technology* **2004,** *38*, (1), 210-220.
75. Israelachvili, J. N., *Intermolecular and surface forces*. Academic Press: Burlington, MA, 2011.
76. Ruckenstein, E.; Prieve, D. C., Adsorption and desorption of particles and their chromatographic separation. *AIChE Journal* **1976,** *22*, (2), 276-283.
77. Feke, D. L.; Prabhu, N. D.; Mann, J. A.; Mann, J. A., A formulation of the short-range repulsion between spherical colloidal particles. *The Journal of Physical Chemistry* **1984,** *88*, (23), 5735-5739.
78. Bergström, L., Hamaker constants of inorganic materials. *Advances in Colloid and Interface Science* **1997,** *70*, (0), 125-169.
79. Zhu, M.; Park, J.; Sastry, A. M., Particle Interaction and Aggregation in Cathode Material of Li-Ion Batteries: A Numerical Study. *Journal of The Electrochemical Society* **2011,** *158*, (10), A1155-A1159.
80. Shen, C.; Li, B.; Wang, C.; Huang, Y.; Jin, Y., Surface Roughness Effect on Deposition of Nano- and Micro-Sized Colloids in Saturated Columns at Different Solution Ionic Strengths. *Vadose Zone Journal* **2011,** *10*, (3), 1071-1081.
81. Fuerstenau, D. W.; Shibata, J., On using electrokinetics to interpret the flotation and interfacial behavior of manganese dioxide. *International Journal of Mineral Processing* **1999,** *57*, (3), 205-217.
82. Sprycha, R., Electrical double layer at alumina/electrolyte interface: I. Surface charge and zeta potential. *Journal of Colloid and Interface Science* **1989,** *127*, (1), 1-11.
83. Tadros, T., General Principles of Colloid Stability and the Role of Surface Forces. *Colloid Stability: The Role of Surface Forces-Part I, Volume 1* **2007**, 1-22.
84. Inc., V. I. *NanoScope Software 6.13*, Veeco Instruments Inc: Plainview, NY, 2004.
85. Shen, C.; Wang, F.; Li, B.; Jin, Y.; Wang, L.-P.; Huang, Y., Application of DLVO Energy Map To Evaluate Interactions between Spherical Colloids and Rough Surfaces. *Langmuir* **2012,** *28*, (41), 14681-14692.